

# **New tractography methods based on parametric models of white matter fibre dispersion**

Matthew Rowe

A dissertation submitted in partial fulfillment

of the requirements for the degree of

**Doctor of Philosophy**

of

**University College London**

Department of Computer Science

University College London

2014

*I, Matthew Rowe, confirm that the work presented in this thesis is my own. Where information has been derived from other sources, I confirm that this has been indicated in the thesis.*

---

# Abstract

Diffusion weighted magnetic resonance imaging (DW-MRI) is a powerful imaging technique that can probe the complex structure of the body, revealing structural trends which exist at scales far below the voxel resolution. Tractography utilises the information derived from DW-MRI to examine the structure of white matter. Using information derived from DW-MRI, tractography can estimate connectivity between distinct, functional cortical and sub-cortical regions of grey matter. Understanding how separate functional regions of the brain are connected as part of a network is key to understanding how the brain works. Tractography has been used to delineate many known white matter structures and has also revealed structures not fully understood from anatomy due to limitations of histological examination. However, there still remain many shortcomings of tractography, many anatomical features for which tractography algorithms are known to fail, which leads to discrepancies between known anatomy and tractography results. With the aim of approaching a complete picture of the human connectome via tractography, we seek to address the shortcomings in current tractography techniques by exploiting new advances in modelling techniques used in DW-MRI, which provide more accurate representation of underlying white matter anatomy.

This thesis introduces a methodology for fully utilising new tissue models in DW-MRI to improve tractography. It is known from histology that there are regions of white matter where fibres disperse or curve rapidly at length scales below the DW-MRI voxel resolution. One area where dispersion is particularly prominent is the corona radiata. New DW-MRI models capture dispersion utilising specialised parametric probability distributions. We present novel tractography algorithms utilising these parametric models of dispersion in tractography to improve connectivity estimation in areas of dispersing fibres. We first present an algorithm utilising the the new parametric models of dispersion for tractography in a simple Bayesian framework. We then present an extension to this algorithm which introduces a framework to pool neighbourhood information from

multiple voxels in the neighbourhood surrounding the tract in order to better estimate connectivity, introducing the new concept of the neighbourhood-informed orientation distribution function (NI-ODF). Specifically, using neighbourhood exploration we address the ambiguity arising in 'fanning polarity'. In regions of dispersing fibres, the antipodal symmetry inherent in DW-MRI makes it impossible to resolve the polarity of a dispersing fibre configuration from a local voxel-wise model in isolation, by pooling information from neighbouring voxels, we show that this issue can be addressed.

We evaluate the newly proposed tractography methods using synthetic phantoms simulating canonical fibre configurations and validate the ability to effectively navigate regions of dispersing fibres and resolve fanning polarity. We then validate that the algorithms perform effectively in real *in vivo* data, using DW-MRI data from 5 healthy subjects. We show that by utilising models of dispersion, we recover a wider range of connectivity compared to other standard algorithms when tracking through an area of the brain known to have significant white fibre dispersion - the corona radiata. We then examine the impact of the new algorithm on global connectivity estimates in the brain. We find that whole brain connectivity networks derived using the new tractography method feature strong connectivity between frontal lobe regions. This is in contrast to networks derived using competing tractography methods which do not account for sub-voxel fibre dispersion. We also compare thalamo-cortical connectivity estimated using the newly proposed tractography method and compare with a competing tractography method, finding that the recovered connectivity profiles are largely similar, with some differences in thalamo-cortical connections to regions of the frontal lobe. The results suggest that fibre dispersion is an important structural feature to model in the basis of a tractography algorithm, as it has a strong effect on connectivity estimation.

## Acknowledgements

I would like to thank my supervisor Daniel Alexander and my cosupervisor Gary Zhang, both of whom have lent the best of guidance with encouragement and enthusiasm in every aspect of my PhD work.

I would also like to thank other people who have lent advice or guidance during my MRes and PhD at UCL. My thanks go to John Clayden who has offered some insightful guidance and David Atkinson, who supervised me through my second MRes project. My thanks also go to Dave Hawkes and Sebastian Ourselin for offering me a place on the CMIC doctoral training programme.

My thanks are also extended to the many people in my group who have helped me with guidance in my work and also been great company throughout my time at UCL. Laura Panagiotaki, Gemma Morgan and Torben Scheider have provided help above and beyond the call of duty, helping me prepare papers, presentations and furthermore offered sage wisdom and general life strategies. My thanks are also extended to all the members of the Microstructure Imaging Group and CMIC, all of whom have been helpful and have been great company.

Very special thanks go to my family. My parents have provided support of every sort throughout my education and a roof over my head for the past year and my sister Jenny and her boyfriend Gary have been great companions and flatmates throughout my time in London.

# Contents

|          |  |           |
|----------|--|-----------|
| <b>1</b> | <b>Introduction and outline</b>                                | <b>16</b> |
| 1.1      | Introduction . . . . .   | 16        |
| 1.1.1    | Problem statement . . . . .                                    | 19        |
| 1.1.2    | Project aims . . . . .   | 19        |
| 1.1.3    | Contributions . . . . .  | 20        |
| 1.1.4    | Thesis outline . . . . .                                       | 20        |
| <b>2</b> | <b>Background</b>  | <b>22</b> |
| 2.1      | Tissue structure in the brain . . . . .                        | 22        |
| 2.1.1    | Macroscopic structure of the brain . . . . .                   | 26        |
| 2.1.2    | White matter . . . . .   | 26        |
| 2.2      | Diffusion basics . . . . .                                     | 28        |
| 2.2.1    | Diffusion in free water . . . . .                              | 28        |
| 2.2.2    | Diffusion in neural tissue . . . . .                           | 33        |
| 2.3      | Diffusion weighted magnetic resonance imaging . . . . .        | 35        |
| 2.3.1    | Basic principles of magnetic resonance imaging (MRI) . . . . . | 35        |
| 2.3.1.1  | Excitation and relaxation . . . . .                            | 37        |
| 2.3.1.2  | $T_2^*$ and magnetic field inhomogeneity: . . . . .            | 39        |
| 2.3.1.3  | Spin echo sequence . . . . .                                   | 40        |
| 2.3.2    | Diffusion weighted magnetic resonance imaging . . . . .        | 40        |
| 2.3.2.1  | Q-space . . . . .  | 42        |

|          |   |           |
|----------|---|-----------|
| 2.4      | Modelling white matter architecture . . . . .                                       | 43        |
| 2.4.1    | The diffusion tensor . . . . .  | 43        |
| 2.4.2    | Extracting informative measures from the diffusion tensor . . . . .                 | 45        |
| 2.4.3    | Complex sub-voxel fibre architecture . . . . .                                      | 48        |
| 2.4.4    | Multi-compartment models . . . . .  | 49        |
| 2.4.4.1  | Ball and stick model . . . . .  | 50        |
| 2.4.4.2  | Multi-tensor model . . . . .  | 51        |
| 2.4.5    | Non-parametric approaches . . . . .   | 52        |
| 2.4.5.1  | Diffusion spectrum imaging . . . . .  | 53        |
| 2.4.5.2  | Q-ball imaging (QBI) . . . . .  | 54        |
| 2.4.5.3  | Persistent angular structure MRI (PAS-MRI) . . . . .                                | 54        |
| 2.4.5.4  | Spherical deconvolution . . . . .   | 55        |
| 2.4.6    | Advanced parametric approaches . . . . .  | 56        |
| 2.4.7    | The NODDI tissue model . . . . .  | 59        |
| 2.4.7.1  | Intra-cellular compartment . . . . .  | 61        |
| 2.4.7.2  | Extra-cellular compartment . . . . .  | 62        |
| 2.4.7.3  | CSF compartment . . . . .   | 62        |
| 2.4.8    | NODDI protocol and fitting . . . . .  | 62        |
| 2.4.9    | NODDI metrics . . . . .   | 63        |
| 2.4.9.1  | Orientation dispersion index (Watson distribution) . . . . .                        | 63        |
| 2.4.9.2  | Orientation tensor and dispersion anisotropy index (Bingham distribution) . . . . . | 63        |
| 2.5      | Summary and conclusion . . . . .  | 64        |
| <b>3</b> | <b>Tractography</b>   | <b>67</b> |
| 3.1      | Tractography . . . . .  | 67        |
| 3.1.1    | Deterministic tractography . . . . .  | 70        |
| 3.1.2    | Probabilistic tractography . . . . .  | 71        |

|          |   |           |
|----------|---|-----------|
| 3.1.2.1  | Bootstrap estimates of uncertainty . . . . .            | 74        |
| 3.1.2.2  | Calibration-based estimates of uncertainty. . . . .     | 74        |
| 3.1.2.3  | Bayesian estimates of uncertainty . . . . .             | 74        |
| 3.1.3    | fODF and dODF tractography techniques . . . . .         | 75        |
| 3.1.4    | Global tractography . . . . .                           | 76        |
| 3.1.4.1  | Advantages . . . . .                                    | 76        |
| 3.1.4.2  | Limitations . . . . .                                   | 77        |
| 3.2      | Summary and conclusions . . . . .                       | 79        |
| 3.3      | Motivations for this work . . . . .                     | 80        |
| <b>4</b> | <b>Utilising measures of dispersion in tractography</b> | <b>82</b> |
| 4.1      | Introduction . . . . .                                  | 82        |
| 4.2      | Methods . . . . .                                       | 83        |
| 4.2.1    | Tractography . . . . .                                  | 83        |
| 4.2.1.1  | NODDI tractography . . . . .                            | 83        |
| 4.2.1.2  | PICo tractography . . . . .                             | 88        |
| 4.2.1.3  | MRtrix tractography . . . . .                           | 88        |
| 4.2.1.4  | Methodological differences . . . . .                    | 89        |
| 4.3      | Experiments . . . . .                                   | 89        |
| 4.3.1    | Synthetic data . . . . .                                | 89        |
| 4.3.2    | <i>In vivo</i> data . . . . .                           | 92        |
| 4.4      | Results . . . . .                                       | 92        |
| 4.5      | Discussion and conclusions . . . . .                    | 94        |
| <b>5</b> | <b>Neighbourhood exploration</b>                        | <b>98</b> |
| 5.1      | Introduction . . . . .                                  | 98        |
| 5.2      | Particle filters . . . . .                              | 100       |
| 5.2.1    | Neighbourhood exploration framework . . . . .           | 102       |
| 5.2.1.1  | Parameter choices . . . . .                             | 109       |

|          |   |            |
|----------|---|------------|
| 5.3      | Experiments and results . . . . .               | 111        |
| 5.3.1    | Evaluation on synthetic dataset . . . . .       | 111        |
| 5.3.2    | <i>In vivo</i> data . . . . .                   | 111        |
| 5.3.3    | <i>In vivo</i> experiments . . . . .            | 113        |
| 5.4      | Discussion . . . . .                            | 115        |
| 5.5      | Conclusions . . . . .                           | 122        |
| <b>6</b> | <b>Connectivity</b>                             | <b>124</b> |
| 6.1      | Introduction . . . . .                          | 124        |
| 6.2      | Principal networks . . . . .                    | 125        |
| 6.2.1    | Introduction and theory . . . . .               | 125        |
| 6.2.2    | Methods . . . . .                               | 127        |
| 6.2.2.1  | Principal network calculation: . . . . .        | 129        |
| 6.2.3    | Results . . . . .                               | 131        |
| 6.2.4    | Discussion . . . . .                            | 131        |
| 6.3      | Thalamic connectivity . . . . .                 | 134        |
| 6.3.1    | Methods . . . . .                               | 134        |
| 6.3.2    | Results . . . . .                               | 135        |
| 6.3.3    | Discussion . . . . .                            | 138        |
| 6.4      | Conclusions . . . . .                           | 139        |
| <b>7</b> | <b>Discussion and conclusions</b>               | <b>142</b> |
| 7.1      | Future directions . . . . .                     | 144        |
|          | <b>Appendices</b>                               | <b>148</b> |
| <b>A</b> | <b>Publications</b>                             | <b>148</b> |
| A.0.1    | Publications associated with this work. . . . . | 148        |
| <b>B</b> | <b>Sampling from a Bingham distribution</b>     | <b>151</b> |
| B.1      | Rejection sampling . . . . .                    | 151        |

|          |  |            |
|----------|--|------------|
| B.1.1    | Sampling from a Watson distribution . . . . .  | 152        |
| B.1.2    | Sampling from a Bingham distribution using the Watson as the instrumental distribution . . . . . | 152        |
| <b>C</b> | <b>Second principal networks</b>   | <b>154</b> |

# List of Figures

|      |  |    |
|------|--|----|
| 2.1  | Macroscopic anatomy of the brain, showing white matter, grey matter and CSF. . . . .               | 23 |
| 2.2  | Simple illustration of CNS microstructure. Showing the soma, axon, glial cells and myelin. . . . . | 24 |
| 2.3  | 4 major lobes of the brain. . . . .  | 25 |
| 2.4  | Association fibres. . . . .  | 27 |
| 2.5  | Commissural fibres. . . . .  | 28 |
| 2.6  | Corona radiata. . . . .  | 29 |
| 2.7  | Corona radiata histological section. . . . .   | 30 |
| 2.8  | Brownian motion of water molecules. . . . .  | 31 |
| 2.9  | Water molecules restricted inside cylindrical boundaries. . . . .                                  | 34 |
| 2.10 | Nuclear spins in the absence of and presence of a magnetic field $\mathbf{B}_0$ . . . . .          | 36 |
| 2.11 | Net magnetic moment $M$ . . . . .  | 37 |
| 2.12 | Flipping the net magnetisation vector by $90^\circ$ and $180^\circ$ . . . . .                      | 39 |
| 2.13 | Spin echo sequence . . . . .   | 40 |
| 2.14 | PGSE sequence diagram. . . . .   | 41 |
| 2.15 | Illustration of diffusion profiles in varying tissue geometries . . . . .                          | 45 |
| 2.16 | Mean diffusivity (MD), fractional anisotropy (FA) and direction of principal eigenvector. . . . .  | 47 |
| 2.17 | Subvoxel fibre architecture. . . . .   | 48 |
| 2.18 | Illustration of spherical deconvolution. . . . .   | 55 |

|  |    |
|--|----|
| 2.19 Comparison of Watson and Bingham distributions. . . . .   | 58 |
| 2.20 Bingham distributions fit to diffusion data using the NODDI technique. . .  | 58 |
| 2.21 Different fibre configurations with corresponding ODFs. . . . .   | 60 |
| 2.22 NODDI compartments . . . . .  | 60 |
| 2.23 Bingham distributions fit to DW-MRI data in the brain using NODDI. . .  | 64 |
| 3.1 Simple diagram of a tract or streamline, formed from a train of vectors. . .   | 68 |
| 3.2 Deterministic vs. probabilistic tractography methods. . . . .  | 72 |
| 3.3 Schematic illustration of local tractography. . . . .  | 77 |
| 3.4 Schematic illustration of global tractography. . . . .   | 78 |
| 4.1 Tractography on synthetic data to fix curvature prior. . . . .   | 86 |
| 4.2 Binned streamlines for varied values of curvature prior. . . . .   | 87 |
| 4.3 Discretely approximating posterior in equation 4.2 . . . . .   | 88 |
| 4.4 Dispersing phantom structure. . . . .  | 90 |
| 4.5 Tractography on synthetic phantom using PICO and dispersion tractography.  | 91 |
| 4.6 Tractography on synthetic crossing phantom at high and low values of $\gamma$ .  | 91 |
| 4.7 Seed ROIs and waypoints used for <i>in vivo</i> tractography. . . . .  | 93 |
| 4.8 Tractography on <i>in vivo</i> data . . . . .  | 95 |
| 4.9 Binned streamlines for varied values of curvature prior. . . . .   | 95 |
| 4.10 Tractography, using the algorithm described in section 4.2.1.1, from seeds<br>in the corpus callosum (a) and the internal capsule (c). Results using con-<br>strained spherical deconvolution (MRtrix) [118] from the same seed points<br>in the corpus callosum (b) and the internal capsule (d). Overlayed on coro-<br>nal slice of FA map. . . . . | 96 |
| 4.11 Tractography, using the algorithm described in section 4.2.1.1 on 4 major<br>white matter structures, the cingulum (Ci), the occipito-frontal fasciculus<br>(OF), the superior longitudinal fasciculus (SLF) and the inferior longitudi-<br>nal fasciculus (ILF). Overlayed on sagittal slice of FA map. . . . .                                      | 96 |

|     |  |     |
|-----|--|-----|
| 5.1 | Illustration of fanning polarity ambiguity. The two opposing fibre configurations give the same fODF when estimated from diffusion data. . . . .   | 99  |
| 5.2 | Illustration of diverging and converging neighbourhood structure. . . . .  | 101 |
| 5.3 | Illustration of neighbourhood exploration in the case of of diverging (a), converging (b), coherent (c) and curving (d) neighbourhood structure in the tracking direction. Red streamlines are highly weighted, blue are low weighted. . . . .   | 104 |
| 5.4 | Illustration of the algorithm outlined in pseudocode above in algorithm 1.   | 106 |
| 5.5 | Illustration of the stages of neighbourhood exploration: initialisation from the local Bingham distribution (a), particle update and weighting (b), particle selection (c) and tract propagation direction selection (d). . . . .  | 108 |
| 5.6 | Illustration of two extremes of parameter choices which are non-ideal for the neighbourhood exploration framework. In Figure 5.6(a) the neighbourhood exploration doesn't go far enough, it remains within the local voxel and does not gather sufficient information about neighbourhood structure. In Figure 5.6(b) the neighbourhood exploration goes too far and gathers information from structures which are not related to the local voxel structure we are trying to navigate. . . . . | 110 |
| 5.7 | Demonstration of particle filter behaviour in regions of diverging (a), converging (b), coherent (c) and curving (d) neighbourhood structure in the tracking direction. Colour denotes particle weight, blue is low through to red, which is high, yellow is intermediate. . . . .   | 110 |
| 5.8 | 100 repetitions of the tracking algorithm in regions of diverging (a), (b) and converging (c) and (d) neighbourhood structure in the tracking direction. In (a) and (c), particle filter neighbourhood exploration is used, while in (b) and (d) only a curvature prior is used as in chapter 4. . . . .   | 112 |

|      |   |     |
|------|---|-----|
| 5.9  | Tracking from a single seed on a synthetic crossing fibre structure. The algorithm fails to successfully navigate the crossing region due to the dependence of the neighbourhood exploration framework on the means of the Bingham distributions in each voxel. . . . .   | 113 |
| 5.10 | Mean directions of Bingham distributions in a sagittal slice in the Corona Radiata, showing the directional dispersion and polarity. The red arrows illustrate the dispersing structure. . . . .  | 115 |
| 5.11 | ROIs used for the <i>in vivo</i> experiments. ROIs are manually outlined to cover the whole of the corticospinal tract and the pons in the region of the cerebral peduncle, and a location in the white matter in the superior portion of the pre-central gyrus. . . . .  | 116 |
| 5.12 | Tractography from a seed region in the cerebral peduncle and a seed region in the superior portion of the pre-central gyrus with four different algorithms. The red arrows show the anterior connections which are recovered by NODDI-NIT, but are missed or under-represented by alternative algorithms. The yellow arrows point to the region where false positives occur if neighbourhood exploration is not used. . . . . | 117 |
| 5.13 | Tracking from a seed region in the cerebral peduncle and a seed region in the superior portion of the pre-central gyrus for each hemisphere of one subject. . . . .   | 118 |
| 5.14 | Tractography from a seed region in the cerebral peduncle in four subjects, using NODDI-NIT and MRtrix. . . . .  | 119 |
| 5.15 | Tractography from a seed region in the superior portion of the pre-central gyrus in four subjects, using NODDI-NIT and MRtrix. . . . .  | 120 |
| 5.16 | Tractography in 3 major WM fascicles for validation: the cingulum, the inferior longitudinal fasciculus (ILF) and the inferior fronto-occipital fasciculus (IFOF). . . . .  | 121 |

|      |  |     |
|------|--|-----|
| 6.1  | Illustration of principal networks approach on a simple example. Network A can be broken down in to its first (B) and second (C) principal network via PNA, capturing the two canonical subnetworks in the whole. Figure from [27] . . . . .   | 126 |
| 6.2  | Extraction of whole brain structural connectivity network and principal network analysis. . . . .  | 127 |
| 6.3  | Desikan-Killiany atlas . . . . .   | 128 |
| 6.4  | First principal networks derived via NODDI-NIT . . . . .   | 130 |
| 6.5  | First principal networks derived via DT-PICo . . . . .   | 130 |
| 6.6  | Eigenvalues of the first 20 principal networks . . . . .   | 132 |
| 6.7  | Division of the cortex into 10 separate target regions for tractography to facilitate examination of thalamo-cortical connectivity. Rendered on a single subject's brain. . . . .  | 135 |
| 6.8  | Probabilistic mapping of cortical connections to target regions shown in Figure 6.7 for subject 1. Each cortical target region is shown with the probabilistic maps from both NODDI-NIT and DT-PICo. . . . .   | 136 |
| 6.9  | Segmented left thalamus in 3 subjects . . . . .  | 137 |
| 6.10 | NODDI orientation dispersion index (ODI). High values of the ODI indicate regions of high fibre dispersion. The yellow circles highlight the regions of the frontal WM where high fibre dispersion is detected. High fibre dispersion can also be observed throughout the centrum semiovale. . . . | 141 |
| C.1  | Second principal networks . . . . .  | 155 |
| C.2  | Second principal networks . . . . .  | 155 |

# List of Tables

|     |   |     |
|-----|---|-----|
| 6.1 | Cortical GM regions from FreeSurfer parcellation and associated labels. . | 129 |
| 6.2 | Lobe associations of vertices of first PN: NODDI-NIT . . . . .            | 132 |
| 6.3 | Lobe associations vertices of first PN: DT-PICo . . . . .                 | 132 |
| 6.4 | Brain regions and associated colours. . . . .                             | 138 |

# Chapter 1

## Introduction and outline

### 1.1 Introduction

Magnetic resonance imaging (MRI) has proved to be a particularly powerful tool to examine the body. The technique allows exploration of the entire body, yielding 3D volumes of image data without the use of ionising radiation and an extremely flexible range of contrast options. MRI acquisition sequences can be tuned to create contrast between different tissues and even the motion of blood or the diffusion of water at microscopic length scales inside tissue. This flexibility of MRI as a medical imaging tool has led to it becoming highly prevalent in many areas of medicine and biological science.

MRI is of particular importance in neuroimaging, due to its high contrast sensitivity to the various tissue types in the brain, allowing the study of deep brain structure only previously accessible by invasive techniques, which is only possible via post-mortem examination, or during traumatic surgical procedures on a patient or animal subject. Of particular interest in neurology is the ability to determine the boundaries of cancerous regions, lesions or regions of tissue degradation as in diseases such as multiple sclerosis (MS) or Alzheimer's disease.

MRI has proved to be a particularly powerful neurological imaging tool due to the ability to tune the imaging sequences to be contrast-sensitive to the diffusive motion of

water molecules, driven by thermal energy, at microscopic length scales. Water is hugely abundant in the body. Water molecules engage in random walks in a process known as self diffusion. If the sequence is tuned appropriately, a signal drop can be detected when water molecules move over the course of a magnetic pulse sequence. Such an MR imaging technique is referred to as 'diffusion weighted magnetic resonance imaging' (DW-MRI) and is the basis of a considerable volume of neuroimaging research, due to the ability to probe structural trends in tissue at the microscopic scale.

When the motion of water molecules is impeded by tissue structures such as cell membranes, the departure from free diffusion behaviour can be detected and interpreted as information on the geometrical properties of the tissue, particularly the size, shape, and orientation of the cells. This opens up grand possibilities in white matter (WM), where the large majority of the volume consists of densely packed cylindrical cells which connect distinct brain regions over orders of several micrometers to several centimetres. It is possible to derive information from DW-MRI about the orientation of these cells in each voxel of an image volume, yielding a 3 dimensional volume of directional data. Fiber tractography integrates paths by piecing together streamlines through this directional data allowing us insight into the connectivity of the brain. The way the brain is connected as a network is key to understanding its function and how it is affected by pathology or trauma. This has potentially wide ranging impacts in developing our understanding of the brain and also in applications like surgical planning, where knowing the boundaries of WM structures accurately can have critical impacts on patient outcomes.

Mathematical models relate the signal measured from DW-MRI to interesting properties of the structure of WM, including, but not limited to, orientation, which is pertinent in tractography. Other properties which the models can reveal include cell density, cell size, intra-cellular and extra-cellular volume. One of the simplest models of WM is the diffusion tensor (DT) model [11]. The diffusion tensor model works by fitting a covariance matrix to the DW-MRI signals characterising the diffusion characteristics in a given reference frame. From this covariance matrix, various properties can be extracted such

as the mean diffusivity (MD) and the eccentricity of the diffusion profile, often referred to as the diffusion anisotropy [10].

Due to the simplicity of the model the DT has become widely used both in research and clinically, however, the parameters which can be derived from the model are fairly non-specific and the diffusion tensor is affected by a conflation of several structural tissue properties. The DT does not in itself disentangle the effects of complex structural phenomena such as crossing fibres, cerebro spinal fluid (CSF) or grey matter partial volume or fanning or bending of fibres at the sub-voxel scale. DW-MRI research has therefore moved on to more advanced models which aim to disambiguate specific complex structural features of tissue such as crossing and fibres. The resolution of multiple crossing fibre populations existing inside a voxel's boundaries has been approached in numerous ways, including multi-tensor models [121] and other multi-compartment models such as ball and multiple sticks [13]. Various multi-compartment models [112] aim to separate contributions to the signal from CSF and the fibrous compartment. Approaches capable of disambiguating distinct, crossing fibre populations can reduce both false negative and false positive connections resulting from tractography utilising models assuming a single fibre population. Examples include the lack of the lateral callosal (inter-hemispheric) connections (false negatives) or the over-representation of the vertical callosal connections (false-positives). However, there still remain many clear false negative and false positive connections, leading to an incomplete and inaccurate representation of the human connectome via tractography.

These false negatives and false positives arise due to two key limitations: the remaining over-simplicity in the models used to describe the data, which do not account for fanning or bending and the inherently greedy, local nature of widely used tractography algorithms. Sub-voxel scale fanning can be observed in histological microscopy and compares qualitatively with measures obtained from DW-MRI [109, 110]. Techniques have evolved which extend the concept of multiple discrete fibre populations per voxel to a continuous distribution of fibre orientations represented non-parametrically

as a fibre orientation distribution function (fODF) [56, 57] or a continuous diffusion profile [120, 34]. While in theory these non parametric techniques can capture sub-voxel fibre dispersion, recent work [108, 135, 65] has suggested that the use of parametric models of sub-voxel fibre dispersion can lead to more accurate and robust estimation of the degree of dispersion of the fibre architecture in both synthetic data and *in vivo* data.

### 1.1.1 Problem statement

Continuing development of DW-MRI modelling techniques has yielded new sophisticated models of white matter architecture which better represent the underlying tissue structure. These models are advantageous for use in tractography as they give a more accurate depiction of the fibre architecture, however, so far, these models have not been used in tractography techniques. New parametric models of sub-voxel fibre dispersion can help address some of the false negatives and false positives which can arise from ignorance of the variation of WM structure occurring below the sub-voxel scale by providing a more accurate representation of the underlying WM structure. This motivates the use of parametric models of fibre dispersion in tractography. Utilising these models in tractography is not trivial, there are challenges which lie in extracting viable tractography results from the use of such models. In this thesis we aim to implement tractography algorithms which utilise these models and address any technical issues therein.

### 1.1.2 Project aims

The goal of this work is to propose a framework in which to fully utilise parametric models of dispersion in tractography, addressing whatever technical issues lie therein. An extension of the NODDI model [135], using a Bingham distribution [115, 116], is the local model chosen for use as the basis for the tractography algorithms presented. The aims of this PhD thesis are to propose and implement tractography algorithms exploiting the NODDI model, demonstrate their efficacy on synthetic and *in vivo* data and

investigate the impact of the new algorithms on connectivity estimation.

### 1.1.3 Contributions

The contributions of this thesis are as follows:

- The design and implementation of new tractography algorithms utilising the NODDI model as a model of dispersing WM fibre architecture.
  - The implementation of a tractography algorithm using a simple Bayesian formulation to apply a curvature prior, producing smooth tracts. We evaluate the algorithm on synthetic phantoms and *in vivo* data
  - The proposal of a tractography algorithm combining parametric models of sub-voxel fibre dispersion with a neighbourhood exploration technique. This addresses the complications arising in the use of antipodally symmetric distributions such as that used in the NODDI model, specifically the key problem of fanning polarity.
- Validation of the new tractography algorithms in synthetic phantoms and *in vivo* data. Showing that accounting for sub-voxel fibre dispersion addresses false negatives of traditional tractography techniques and validating that the neighbourhood exploration framework effectively addresses the issue of fanning polarity arising in parametric models of dispersion.
- Examination of how the use of the proposed algorithm impacts estimates of global connectivity recovered in investigations of cortico-cortical connectivity and thalamo-cortical connectivity.

### 1.1.4 Thesis outline

Chapter 2 starts with the background of the structure of the brain and basic diffusion properties in tissue. The basic principles of MRI and DW-MRI are then covered followed

by the mathematical models which are used to relate the DW-MRI signal to features of the tissue. Much of the contents of chapter 2 form a chapter in the book "DTI: From theory to practice." edited by W. Van Hecke, which is currently in press. This section covers a selection of the most common models, from the simplest, such as the diffusion tensor (DT) [11] and ball and stick [14], through to more advanced approaches such as constrained spherical deconvolution [117] and the NODDI model [135], which is the model on which the tractography algorithms presented in this thesis are based. Chapter 3 introduces the fundamental concepts of tractography and follows with some of the current popular approaches, including deterministic, probabilistic and global tractography methods. Chapter 4 is the first of the contributions chapters, introducing a simple tractography algorithm utilising the NODDI model as the basis. Part of this work was published in the proceedings of the workshop on computational diffusion MRI workshop (CD-MRI) at the 15th international conference on medical image computing and computer assisted intervention (MICCAI) [94]. Experiments on synthetic and *in vivo* provide evaluation of the efficacy of the algorithm. Chapter 5 introduces the new 'neighbourhood informed tractography' (NIT) technique, which is used alongside the dispersive parametric local model of NODDI to improve the accuracy of the results. The efficacy of the algorithm is evaluated on synthetic phantoms to demonstrate its ability to resolve fanning polarity and also applied on *in vivo* data from 5 healthy subjects. A preliminary version of the work in chapter 5 was presented at the IPMI 2013 conference [95] and a journal paper is currently in preparation and close to submission. Chapter 6 applies the NODDI-NIT algorithm to examining thalamo-cortical and cortico-cortical connectivity and examines the effect of including measures of dispersion in tractography on the recovered connectivity profiles. Chapter 7 summarises the main contributions and overall conclusions, along with a discussion on future directions.

# Chapter 2

## Background

### 2.1 Tissue structure in the brain

The brain is a vastly complex organ. It is housed inside the skull and suspended in cerebrospinal fluid (CSF) which fills the open spaces not occupied by brain tissue such as the sulci and ventricles, provides a protective liquid layer around the brain and facilitates chemical transportation. The tissue which makes up the brain can be roughly divided into two distinct types, grey matter (GM) and white matter (WM) [81]. Grey matter is largely composed of neuronal cell bodies [75], while WM is largely composed of the long-range protrusions of neurons called axons, which serve to connect neurons over large distances. There are other types of cells, collectively referred to as 'glial cells', which exist in both GM and WM such as oligodendrocytes, astrocytes and microglia. These facilitate various functions including biochemical support and immune response. Figure 2.1 shows the organisation of grey matter and WM in the brain. The GM makes up the outer regions of the brain and this region is normally referred to as the 'cortex'. The WM makes up the deeper structure which can be revealed by dissecting the brain. There are some regions of grey matter lying beneath the cortex, deep within the WM and these are often referred to as 'sub-cortical' grey matter.

An simple illustration of the major components of neural tissue is provided in Figure

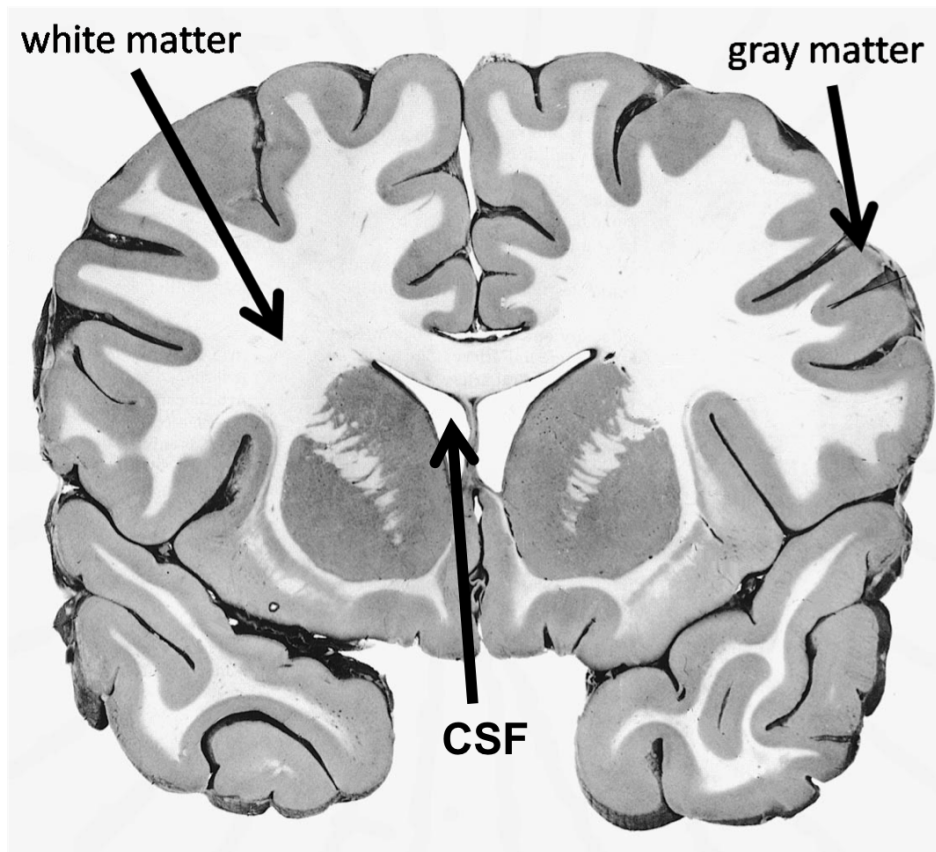


Figure 2.1: Coronal slice of the brain (Atlas of the Human Brain in Section, 2nd ed), showing white matter, grey matter and CSF.

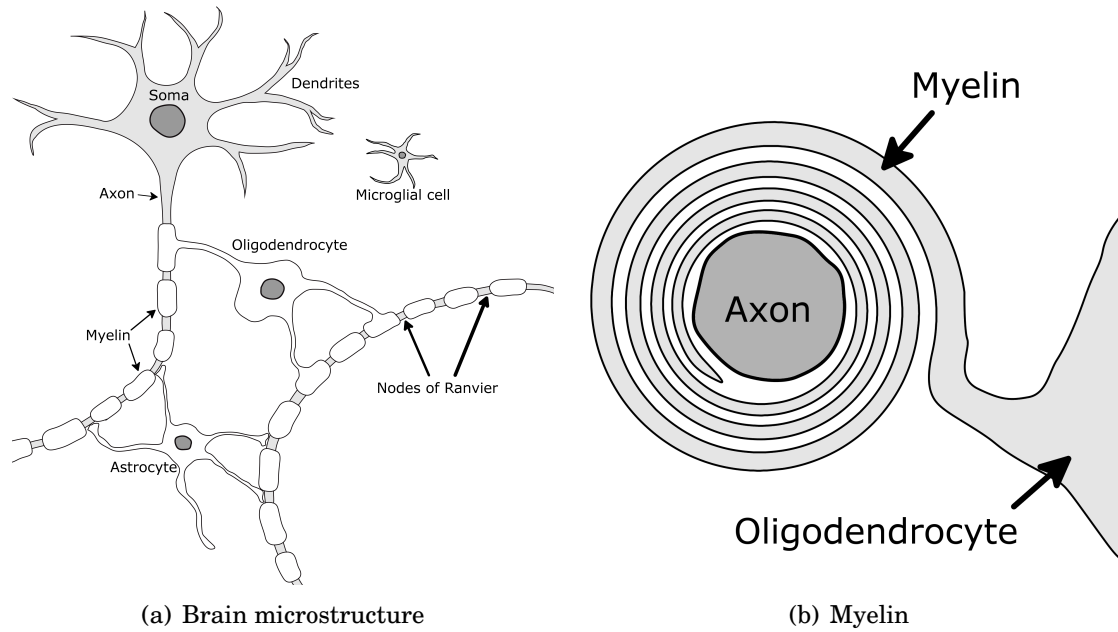


Figure 2.2: Simple illustration of microstructure in the brain .Showing the soma, axon, glial cells and myelin.

2.2(a). The soma is the neuron body, it contains the nucleus and many of the cell's maintenance structures. Typically, neurons have numerous protrusions from the soma collectively referred to as neurites which facilitate electrical communication between separate neurons. The neurites are divided into two distinct types, dendrites and axons. There are typically many dendrites protruding from a single soma, the number and specific structure of the dendrites is highly variable and is dependent on the type of neuron and where it exists in the brain. Each neuron also typically has a single axon. The axon is an extended protrusion of the neuron which can range in length from micrometers to many centimeters and even to over a meter in humans. The axon serves to facilitate long range communication between distinct groups of neurons, which may be in completely distinct regions of the brain or body, while dendrites serve to facilitate communication with neighbouring neurons and with axons terminating in the vicinity [123].

Glial cells are non-neuronal cells which serve a number of purposes such as cell maintenance and metabolic functions, immune response and structural support. There are numerous different types of glia, broadly characterised into two groups, microglia, which form the immune component of the central nervous system and macroglia, which facili-

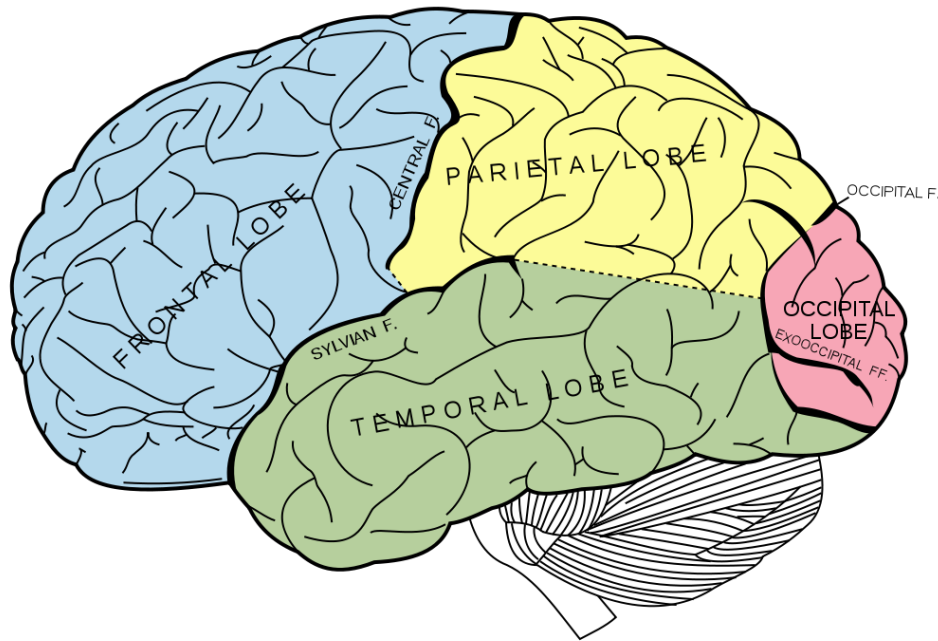


Figure 2.3: Lobes of the brain. Illustration adapted from [47].

tate structural, chemical and nutritional support to other neural cells.

One particular type of macroglia, the oligodendrocyte, has a very specific and important structural function in the central nervous system. Each oligodendrocyte cell exhibits protrusions which wrap around axons forming a protective layer called the myelin sheath. Each protrusion of the oligodendrocyte wraps several times around an axon, forming a multi-layered wall which exists in short repeating sections. The myelin sheath serves in one function as an insulating layer, protecting the axon from electrical interference from neighbouring neural cells and ions and preventing leakage of electrical potential from the axon itself. A second important function of the myelin sheath arises from the discontinuity of the myelin layer. The gaps in between each myelin section are called Nodes of Ranvier and they form points at which electrical potential accumulates and 'hops' to the next gap. This process is referred to as 'saltatory conduction' or 'saltation' and allows rapid and efficient propagation of action potentials along the length of an axon which is faster and more efficient than the wave-like propagation of potential along an unmyelinated axon.

### 2.1.1 Macroscopic structure of the brain

The brain is organised in two hemispheres, which are similar in shape and size, however they do differ in specific details of structure and function. Each hemisphere is divided into 4 major lobes as seen in Figure 2.3: the **frontal lobe** which plays a role in reasoning, language, memory and motor control, the **parietal lobe** which has a role in integrating sensory information, the **temporal lobe** which plays a role in auditory processing and the **occipital lobe** which plays a role in the processing of visual information. The temporal lobe is separated from the frontal lobe by the lateral fissure and the two hemispheres are separated by a prominent central fissure. Each lobe can be subsequently subdivided into regions associated with a particular function distinguished by their cytoarchitecture [18] or divided into regions according to gyral and sulcal patterns based on neuroanatomical conventions and accumulated neuroanatomical knowledge [36, 52].

### 2.1.2 White matter

As mentioned in the previous section, WM is mainly made up of axons [75], which are extended, roughly cylindrical protrusions of neurons which allow the transmission of chemical and electrical impulses between separate neurons and join the brain as a network, facilitating its function. Axons can range in size between several micrometers to many centimeters to over a meter in size in the human central nervous system. The diameter ranges between  $0.1\ \mu m$  to  $20\ \mu m$ , with larger axons facilitating faster transmission of action potentials at a higher spatial cost [123]. The axons are generally grouped in large bundles called fascicles which facilitate gross connections between different brain regions. The neurons in the brain are organised into functional regions with each region performing some particular function. For even basic tasks, communication is required between several of these regions and also with the body through the spinal column or cranial nerves.

The white matter fibres which connect the different regions of the brain are organised

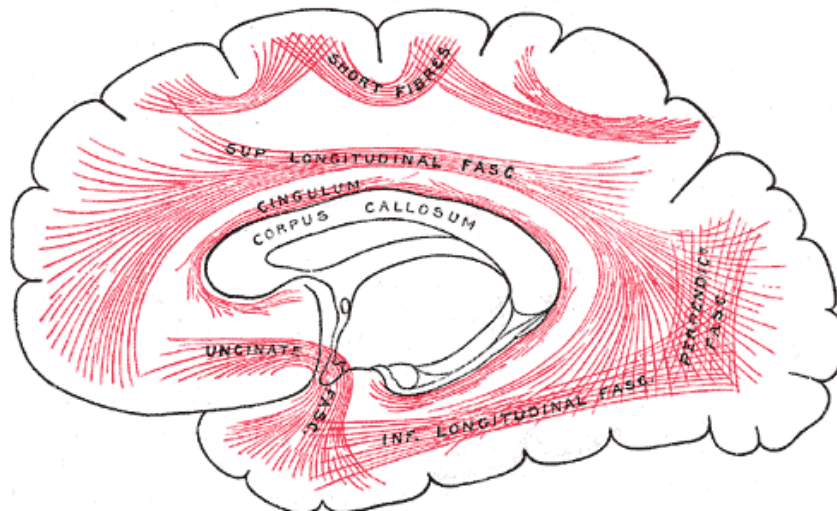


Figure 2.4: Association fibres. Illustration from [47].

into large bundles, referred to sometimes as tracts or fascicles. They can be categorised into 3 separate groups: **association** tracts, which connect regions in the same hemisphere, **projection** tracts, which connect the cortex with subcortical structures in the basal ganglia and the spinal cord and **commisural** tracts, which connect regions in opposing hemispheres.

Figure 2.4 shows the association fibres, the superior longitudinal fasciculus (SLF) which connects regions in the frontal, parietal, occipital and temporal lobes. Also shown are the cingulum (Ci), which runs along the superior edge of the corpus callosum and connects different regions of the limbic system. The inferior longitudinal fasciculus (ILF) connects the temporal and occipital lobe and the uncinate fasciculus connects regions of the temporal lobe with the orbitofrontal cortex. Not shown is the inferior fronto-occipital fasciculus (IFOF) which connects the occipital cortex with parts of the frontal lobe.

Figure 2.5 shows two of the major commisural fibres, the corpus callosum and below it the anterior commissure. The corpus callosum is a very large tract, with an estimated population of 200-250 million axons facilitating large scale connection between the two hemispheres. The other commisural fibres are the anterior commissure, the posterior commissure and the hippocampal commissure, which are all smaller commisural fibres inferior to the corpus callosum facilitating further connection between brain regions in

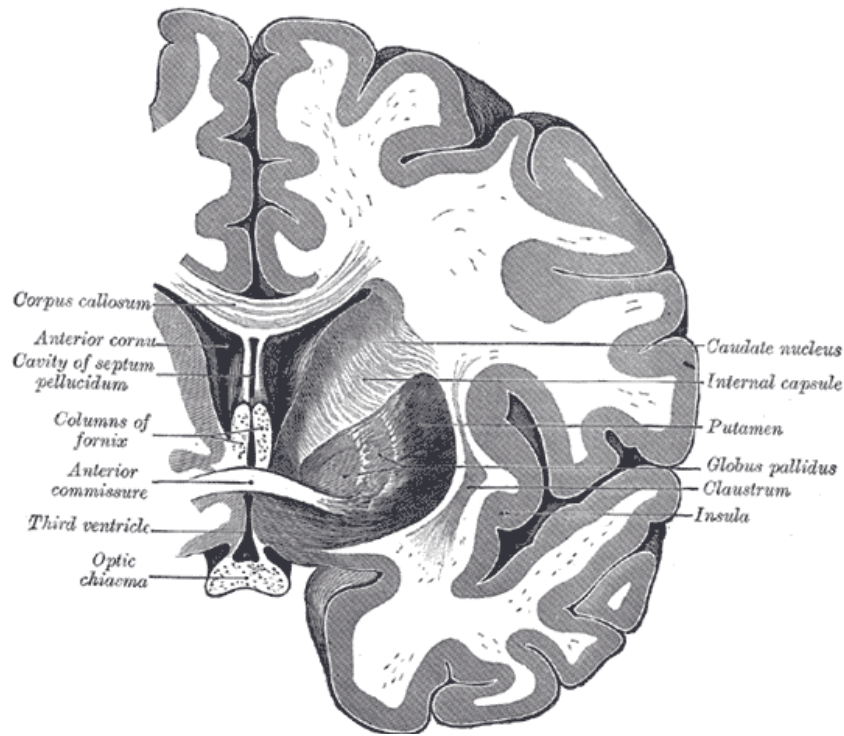


Figure 2.5: Commissural fibres. Diagram from [47]

opposing hemispheres.

Figure 2.6 shows the corona radiata, a structure containing numerous projection tracts, which connects the cortex with the lower regions of the brain, the internal capsule, the spinal column and the cerebral peduncle. Figure 2.7 shows the corona radiata extracted from an *ex vivo* specimen. The corona radiata is a structure where the white matter exhibits significant divergence of fibres, which can be observed in Figure 2.7. This WM structure is of particular importance for this thesis, as we focus on effectively dealing with the dispersion in regions such as the corona radiata in tractography.

## 2.2 Diffusion basics

### 2.2.1 Diffusion in free water

The first observations which led to the understanding of the diffusion of liquids and gases were made in 1826 by the botanist Robert Brown, who was studying the seemingly

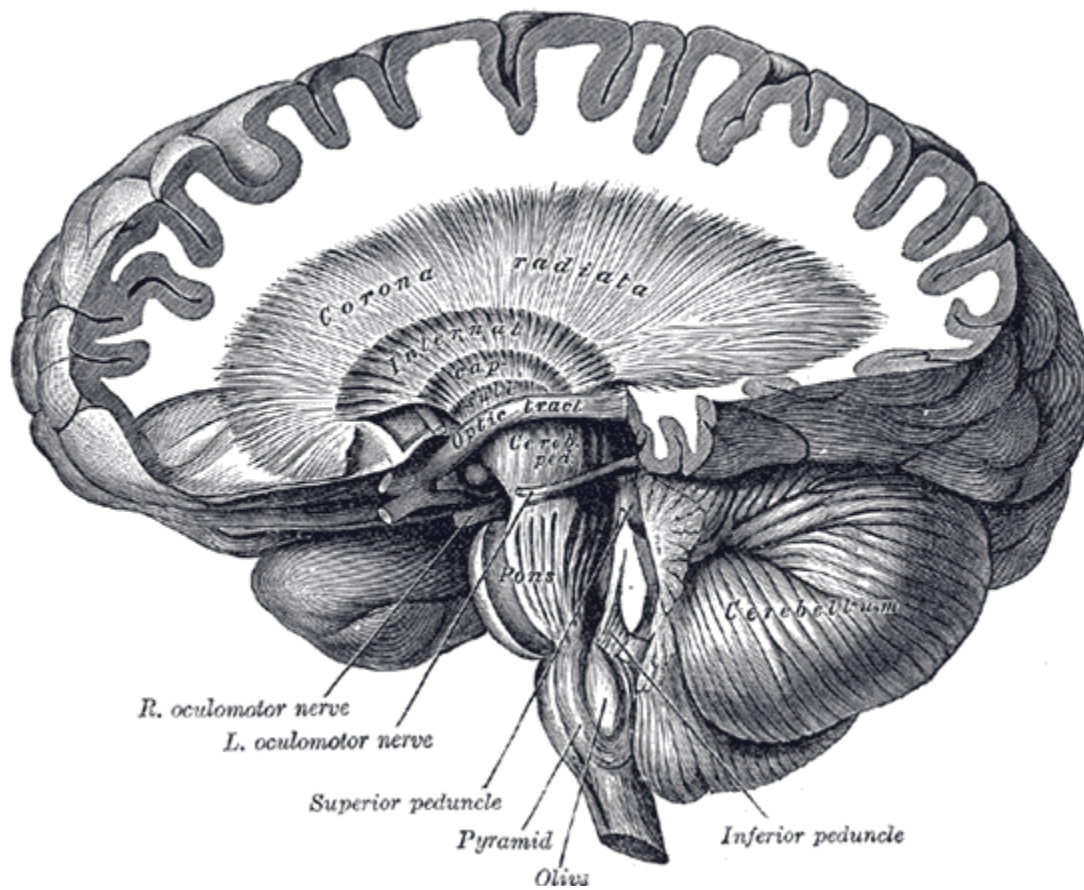


Figure 2.6: Corona radiata. Diagram from [47]

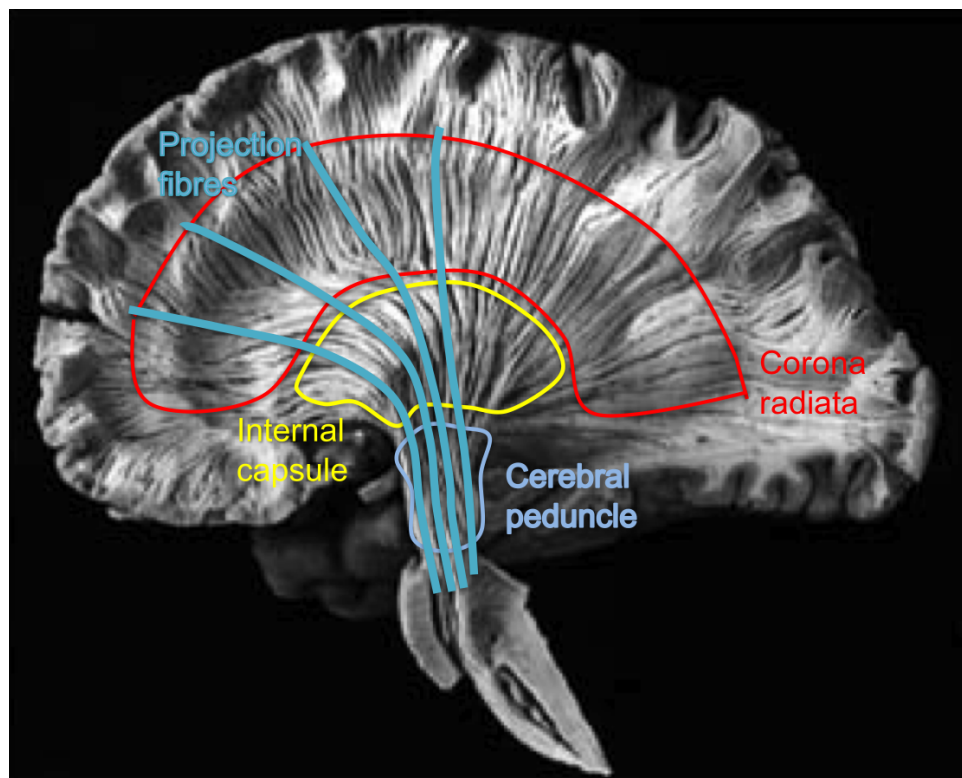


Figure 2.7: Corona radiata histological section with corona radiata, internal capsule and projection fibres illustrated. The projection fibres make up parts of the internal capsule and external capsule and form the corona radiata. Diagram adapted from [129]

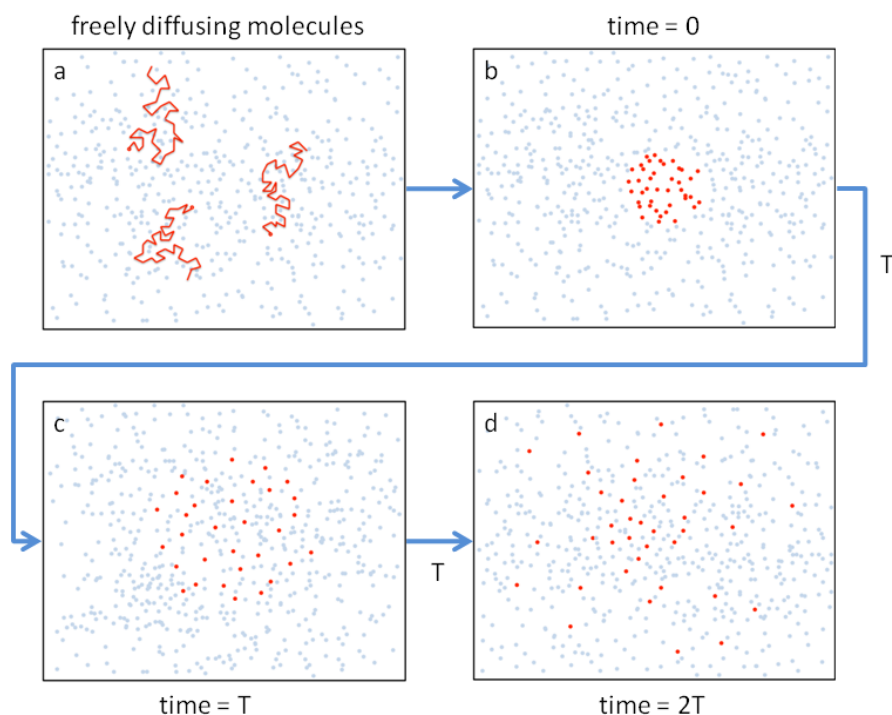


Figure 2.8: Brownian motion of water molecules.

random pattern of motion pollen grains exhibited when suspended in water under a microscope. His initial hypothesis that this motion was due to some biological function of the pollen was rejected and it was later understood that the motion was due to the buffeting of the pollen grains by the water molecules surrounding them. This led to the revelation that liquids and gases are not static and lifeless as they might appear, but the atoms or molecules which make up the fluid undergo constant thermally-driven motion.

Consider a set of water molecules in thermal motion as in Figure 2.8. As they move, they will constantly collide with each other, tracing a chaotic random path as the highlighted molecules do in Figure 2.8a). In Figure 2.8b) a local set are labelled in red. As time progresses to Figures 2.8c) and 2.8d) the labelled molecules spread further apart in a roughly spherical profile. This is akin to the process which governs the spreading of a drop of dye when placed into a clear glass of water. The dye molecules in the water would behave as the labelled molecules do in Figure 2.8.

The diffusion process was summarised mathematically by Adolf Fick in 1855 [42]. Fick's law is given in equation 2.1, where  $\mathbf{J}$  is the net particle flux,  $C$  is the particle concentration and  $D$  is a constant of proportionality known as the diffusion coefficient. Fick's law originally embodied the concept of diffusion in the presence of a concentration gradient, however, diffusive mixing occurs even in the presence of thermal equilibrium, such as in a glass of water. Water molecules diffuse randomly throughout the container (the glass), however, across any arbitrarily defined plane the net flux is zero on average.

$$\mathbf{J} = -D\nabla C \quad (2.1)$$

The dynamics of the thermal motion of water molecules as they collide repeatedly with nearby molecules are too complex to predict in detail. However, it is possible to treat the behaviour of a large ensemble of water molecules in a probabilistic way as Einstein did in 1905, when he introduced the concept of the 'displacement distribution' [41]. The displacement distribution quantifies the fraction of particles which will traverse a certain distance in a given time, or, conversely, the probability that any one particle will traverse a given distance in a given time. Einstein's formulation gives us a probability density function,  $\rho(\mathbf{r})$  quantifying the fraction of particles which have undergone displacement  $\mathbf{r}$  in a time  $t$ . The distribution follows a Gaussian profile in 3 dimensions:

$$\rho(\mathbf{r}) = \frac{1}{\sqrt{(4\pi t D)^3}} e^{-\frac{|\mathbf{r}|^2}{4tD}} \quad (2.2)$$

$D$  is the same diffusion constant from Fick's law in equation 2.1. This gives a 3 dimensional Gaussian distribution with a peak at  $\mathbf{r} = 0$  which is spherically symmetric (i.e. the isoprobability surface is spherical).

Einstein also further derived the mean squared displacement of an ensemble of water molecules after time  $t$ :

$$\langle \mathbf{r}^2 \rangle = 6Dt \quad (2.3)$$

### 2.2.2 Diffusion in neural tissue

The previous section discussed the diffusion properties of water in the absence of boundaries, however, it is how these diffusion properties are affected by the presence of boundaries which allows us to gain unique insight into tissue structure using DW-MRI. If the water molecules encounter hinderances as they are diffusing, the mean squared displacement over a set time will be lower than that observed in free diffusion. Hence the diffusion constant  $D$  in equation 2.3 will *appear* to be lower. Therefore, in a biological tissue, we normally refer to the 'apparent diffusion coefficient' (ADC) [74]. Figure 2.9 illustrates the behaviour of water diffusion when restricted inside cylindrical boundaries. As the molecules diffuse, they are impeded when they encounter a boundary and hence inside these cylinders, they tend to progress along the axis of the cylinder, as in this direction they are not impeded by boundaries. This leads to anisotropic diffusion behaviour. The diffusion profile, which in free water is spherical, becomes elongated along the axis of the cylinders due to the restriction of motion caused by the cylinder walls. The earliest and simplest model to capture the anistoropic behaviour of water in organised media such as parallel cylinders was the diffusion tensor (DT) [11]. Equation 2.2 can be extended to include directional dependence on the displacement vector  $\mathbf{r}$ :

$$\rho(\mathbf{r}) = \frac{1}{\sqrt{(4\pi t|\mathbf{D}|)^3}} e^{-\frac{\mathbf{r}^T \mathbf{D}^{-1} \mathbf{r}}{4t}} \quad (2.4)$$

where

$$\mathbf{D} = \begin{bmatrix} D_{xx} & D_{xy} & D_{xz} \\ D_{xy} & D_{yy} & D_{yz} \\ D_{xz} & D_{yz} & D_{zz} \end{bmatrix} \quad (2.5)$$

$\mathbf{D}$  is normally referred to as the 'diffusion tensor'. The diffusion tensor is a symmetric positive definite matrix, hence it has 6 unique elements. It generally takes the form of an ellipsoid with a special case arising when all non-diagonal elements are zero and

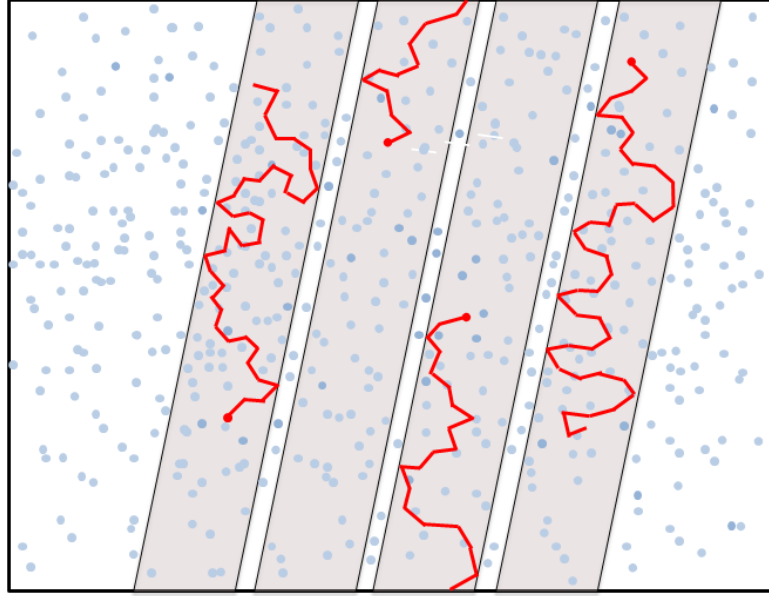


Figure 2.9: Water molecules restricted inside cylindrical boundaries.

$D_{xx} == D_{yy} == D_{zz}$  which is a sphere, representing isotropic diffusion. The concept of the diffusion tensor is explored in further detail later in section 2.4.1.

The DT is particularly applicable for characterising the diffusion properties in WM since it consists of many bundles of coherent axons, which affect water diffusion in much the same way as the parallel cylinders in the previous conceptual example. Singular value decomposition of the diffusion tensor yields eigenvectors which define the principal axes of the ellipsoid and corresponding eigenvalues which define the corresponding diffusivities. The eigenvector with the largest corresponding eigenvalue defines the major axis of the ellipsoid, the axis in which the diffusion of water is least hindered, which in turn generally corresponds to the average orientation of the axes of the cylindrical boundaries. This is a particularly powerful property of the diffusion tensor as it yields a measure which can be interpreted as the predominant direction of axons in white matter using diffusion weighted magnetic resonance imaging.

## 2.3 Diffusion weighted magnetic resonance imaging

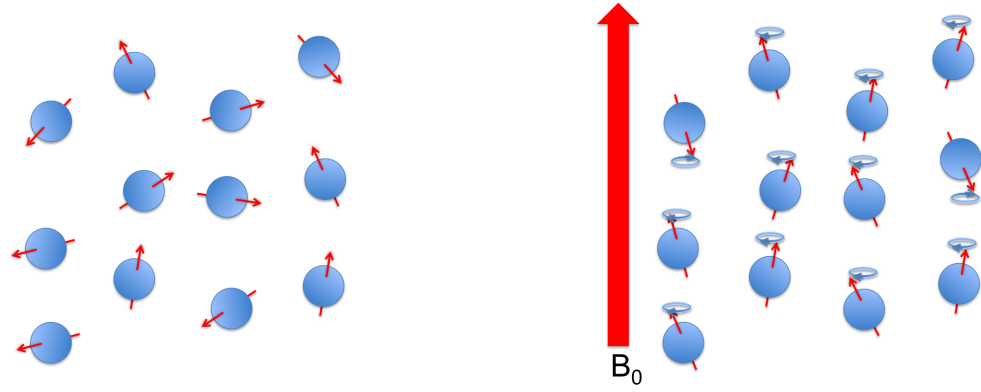
Diffusion weighed magnetic resonance imaging (DW-MRI) is a technique which sensitises the signal recorded by an MRI machine to the diffusion of water in tissue, such that a change in diffusion properties results in a change in the signal detected. Specifically, DW-MRI is tuned in such a way that diffusion creates attenuation of the signal, that is, a signal drop is present where there is high diffusion. In this section, we give a concise overview of the concepts of nuclear magnetic resonance (NMR) followed by a description of how to apply diffusion weighting.

### 2.3.1 Basic principles of magnetic resonance imaging (MRI)

Magnetic resonance imaging is, as the name suggests, dependant on the behaviour of atomic spins in the presence of magnetic fields. An atomic nucleus with an odd number of nucleons possesses a magnetic moment  $\mu$  due to its spin angular momentum  $\mathbf{I}$ , a quantum mechanical property of subatomic particles and nuclei. These are related by  $\mu = \gamma \mathbf{I}$ .  $\gamma$  is the gyromagnetic ratio - a constant specific to the nucleus in question. In the case of a hydrogen nucleus the gyromagnetic ratio has a value of  $2.68 \times 10^8$  rad/(sT). The gyromagnetic ratio dictates the frequency with which a nucleus will precess around a magnetic field.

For the purposes of this thesis, it is only necessary to consider the hydrogen nuclei in water molecules, as it is these which give rise to the signal detected in DW-MRI and in most MRI applications. They are the most abundant nucleus type present in biological tissue. However other nuclei are used in some specialised MRI techniques.

In the absence of any external magnetic fields the magnetic moments of the spins are randomly oriented, as in Figure 2.10(a). In the presence of an external magnetic field  $\mathbf{B}_0$ , the magnetic moments of the nuclei align and precess around the axis of the applied field as in Figure 2.10(b). The spins of hydrogen nuclei adopt one of two possible energy states, a lower one aligned with the magnetic field and a higher energy state



(a) spins randomly aligned in absence of external magnetic field

(b) spins aligned with  $B_0$

Figure 2.10: Nuclear spins in the absence of and presence of a magnetic field  $B_0$ . When the magnetic field is applied the magnetic moments of the nuclei precess around the axis of the field, either aligned or anti-aligned.

which is anti-aligned. Thermal energy causes many of the spins to exist in the higher, anti-aligned state, however, more nuclei exist in the lower, aligned energy state, giving rise to a net magnetic moment  $\mathbf{M}$ . The ratio of spins in the aligned state  $N^-$  to the anti-aligned state  $N^+$  at a temperature  $T$  is governed by the Boltzmann relationship:

$$\frac{N^+}{N^-} = e^{\frac{-\Delta E}{\kappa T}} \quad (2.6)$$

where  $\Delta E$  is the energy difference between the two states.

While the nuclei exist in only two separate states, they are not static. The spin moment precesses around the axis of the applied magnetic field  $B_0$ . The frequency of precession is a key factor in MRI data acquisition and is given by the Larmor equation [17]:

$$\omega_0 = \gamma B_0 \quad (2.7)$$

where  $\omega_0$  is the angular frequency of precession of a spin, otherwise known as the Larmor frequency. As there are hydrogen nuclei in both the aligned and antialigned state, the majority of the net magnetisation is cancelled out and in order to generate a detectable signal in an MRI experiment there must be as large a net magnetic moment

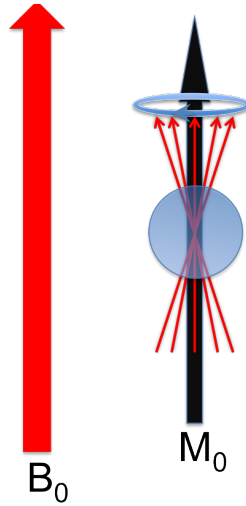


Figure 2.11: Net magnetic moment  $M$ .

as possible, i.e. the ratio of the particles in the aligned state to those in the anti-aligned state must be as large as possible. Hence to achieve this, a significant magnetic field is required to generate practical signal to noise ratios (SNR). Standard MRI scanners have a very strong static magnetic field generated by a superconducting magnet of the order of several Tesla. Clinical human MRI scanners generally have fields of 1-3 tesla and the latest technological developments have allowed fields of up to 7 Tesla. Pre-clinical animal scanners can have a smaller bore and 9 Tesla and above is common. The static magnetic field of the MRI scanner is normally denoted as  $\mathbf{B}_0$ . Spins in different physical locations can be spatially located by the application of an additional magnetic field gradient, which adds linearly to the  $\mathbf{B}_0$  field, by gradient coils which lie inside the bore of the scanner.

The sum of all the magnetic moments of all the nuclei creates a net magnetisation vector  $\mathbf{M}$ , illustrated in Figure 2.11.

### 2.3.1.1 Excitation and relaxation

Signal is generated by perturbing the net magnetisation vector  $\mathbf{M}$  with a radio frequency (RF) pulse. The RF pulse is applied by a hardware insert in the MRI scanner and resonance is achieved by producing an RF pulse with the same frequency as the Larmor frequency of the precessing hydrogen nuclei. This excites the magnetisation vector and

perturbs it out of alignment with  $\mathbf{B}_0$ . It is perturbed out of alignment with  $\mathbf{B}_0$  by a specific angle, governed by the length of the RF pulse, which is determined by the context of the application. Commonly it is perturbed by  $90^\circ$ , into the plane perpendicular to  $\mathbf{B}_0$  or by  $180^\circ$ . The component of the net magnetisation vector  $\mathbf{M}$  in the plane perpendicular to  $\mathbf{B}_0$ ,  $M_{xy}$  then rotates around the axis of  $B_0$  at the Larmor frequency (the z-axis is assumed to be aligned with  $\mathbf{B}_0$ ). For a flip angle of  $90^\circ$   $M_{xy} = M_0$  and  $M_z = 0$ . This moving net magnetic moment induces a signal in the receiver coils which is used to create an image.

After the magnetisation vector has been excited with the application of the RF pulse the net magnetisation then returns to the equilibrium state, aligned with  $\mathbf{B}_0$ , in a process of relaxation. As it does the signal induced in the receiver coils attenuates. This process is called the free induction decay (FID). The transverse magnetisation  $M_{xy}$  decays as the longitudinal magnetisation  $M_z$  recovers to its original (thermal equilibrium) value  $M_0$ . The longitudinal magnetisation recovers with a time constant  $T_1$ :

$$M_z(t) = M_{z,eq}(1 - \exp\left(\frac{-t}{T_1}\right)) \quad (2.8)$$

This is referred to as 'spin-lattice' relaxation. The transverse magnetisation  $M_{xy}$  also decays with another time constant  $T_2$  due to the dephasing of spins as their magnetic moments interact with each other. This is known as 'spin-spin' relaxation. The decay of the signal  $S(t)$  at time  $t$  is dictated by the relationship given in equation 2.9.

$$S(t) = M_0 \exp\left(\frac{-t}{T_2}\right) \quad (2.9)$$

At any particular location  $\mathbf{x}$ , the magnetic field experienced by the spin is given by  $B = B_0 + \mathbf{G}\mathbf{x}$  [22]. Where  $\mathbf{G} = (G_x, G_y, G_z)$  defines a magnetic field gradient in a specific direction.

If we consider the effect of the gradient  $\mathbf{G}$  on the precession of the nuclei spins with reference to equation 2.7, we can see that spins at a position  $x$  will have a position-dependent precession frequency given by:

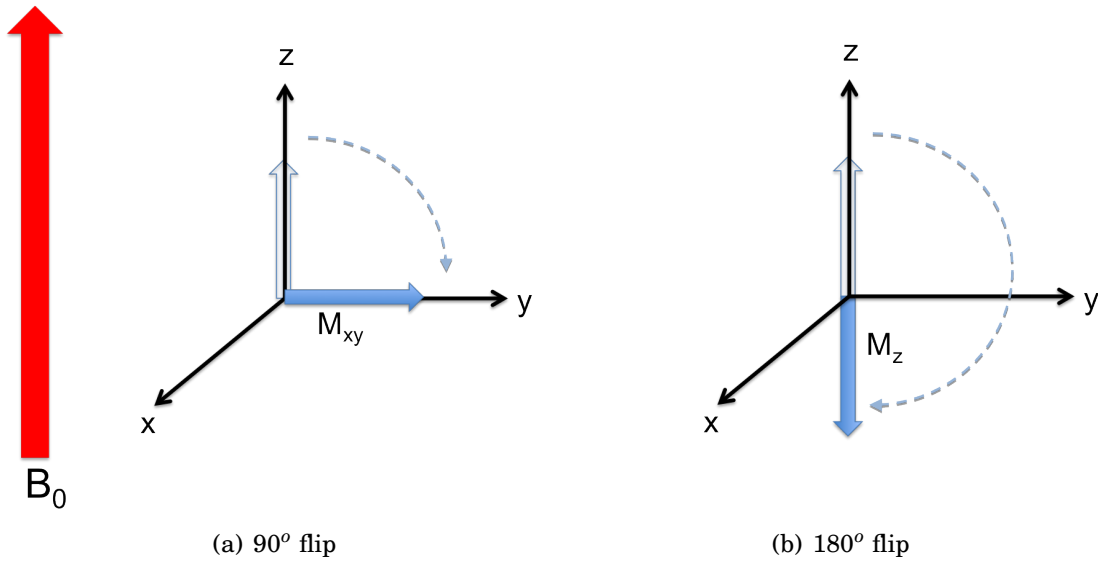


Figure 2.12: Flipping the net magnetisation vector by  $90^\circ$  and  $180^\circ$ .

$$\omega(x) = \gamma B(x) = \gamma(B_0 + Gx) \quad (2.10)$$

Therefore spins at different spatial locations precess at different frequencies. This can be used to spatially locate the spins when collecting signal to form an image. A 'slice select' gradient can be applied during the application of the RF pulse to only excite a thin slice of protons, then further gradients are applied during image acquisition to distinguish protons from different physical locations. The image is acquired in frequency space or 'k-space' and can be reconstructed using a Fourier transform (FT).

### 2.3.1.2 $T_2^*$ and magnetic field inhomogeneity:

$T_2$  decay assumes that the main  $\mathbf{B}_0$  field is homogeneous, where in reality it is not. There are always imperfections in the  $\mathbf{B}_0$  field in any real MRI scanner and biological tissues also exhibit susceptibility effects which create further field inhomogeneity. The dephasing of spin precession due to these effects is denoted  $T_2^*$  decay or  $T_2^*$  relaxation. By using the spin echo sequence described in the next section, we can discount  $T_2^*$  effects, simplifying the process of acquiring magnetic resonance images.

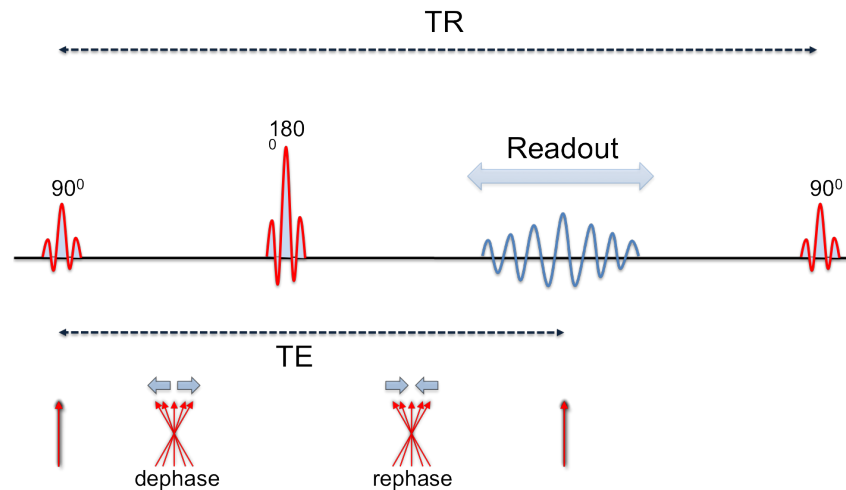


Figure 2.13: Spin echo sequence

### 2.3.1.3 Spin echo sequence

As the FID decays very quickly, it is not useful to read it with the receiver coils, so a second  $180^\circ$  RF pulse is applied to produce an 'echo'. The  $180^\circ$  RF pulse reverses the phase relationship of the spins so the dephasing which caused the decay of the transverse magnetisation is now reversed and the magnetic moment precessions now rephase and produce a measurable signal at a time normally denoted as  $TE$ . The  $180^\circ$  RF pulse is applied at  $TE/2$ . At this time, we then collect the signal to form the image using 'readout' gradients to spatially locate the spins. After a time  $TR$ , the process is repeated to read the next line of the image. During an MRI sequence, this process is normally repeated for each line of voxels and the length of  $TR$  along with the intended dimensions of the image dictate the length of time the scan will require. Figure 2.13 gives an illustration of the spin echo sequence.

## 2.3.2 Diffusion weighted magnetic resonance imaging

This section introduces the basic theory behind sensitising the MRI signal to diffusion. The pulsed gradient spin-echo (PGSE) sequence was proposed by Stejskal and Tanner in 1965 [113] and has become ubiquitous in diffusion weighted imaging. The PGSE sequence utilises the same spin-phase interactions used to spatially locate spins to also

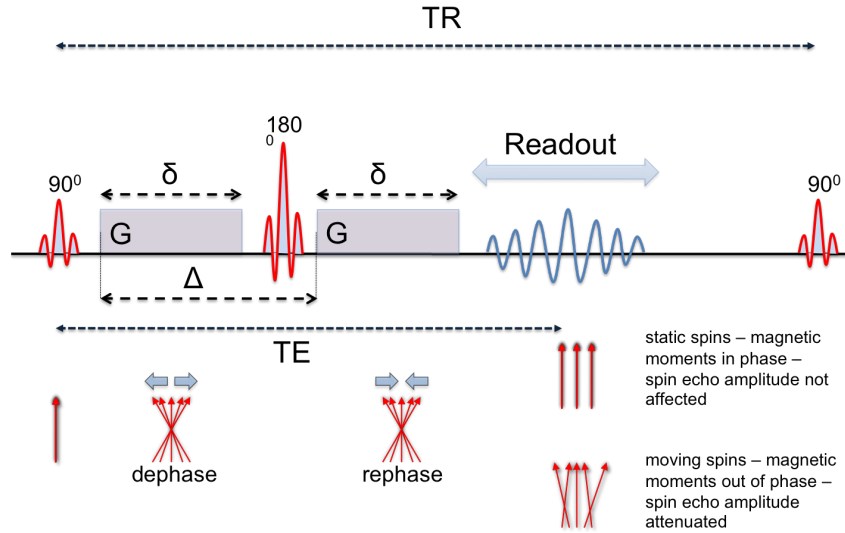


Figure 2.14: The PGSE sequence. The  $180^\circ$  RF pulse between the readout gradients effectively reverses the polarity of the second gradient with respect to the first.

apply diffusion weighting. The key to the PGSE sequence is to apply a magnetic gradient for some fixed time  $\delta$ , during which spins in different locations will diverge in phase, then apply the *effective* opposite gradient for the same fixed time. After the first gradient pulse the spins across a sample will accrue a phase difference with other spins according to their location. The second gradient pulse then acts in the opposite sense, as it is the opposite polarity. For any spin which has not moved, this will have the effect of returning it to its original phase, however, for any spin which has moved, upon the action of the second gradient pulse, it will not return to its original phase as it will experience a different local magnetic field according to equation 2.10. This creates a signal loss in an area in which water molecules are diffusing, the signal loss is greater the further the water molecules travel in between the two gradient pulses. Therefore the application of the pulsed gradients before the image readout has the effect of quantifying the amount of diffusion in each voxel parallel to the direction of the applied gradient  $\mathbf{G}$ .

Figure 2.14 outlines the PGSE sequence. The key parameters which govern the amount of diffusion weighting are the magnitude of the gradient pulse  $G$ , the time width of the pulses  $\delta$  and the time elapsed between the pulses  $\Delta$ . The diffusion weighted signal  $S$  then obeys the equation:

$$A = \frac{S}{S_0} = e^{-\left(\gamma^2 G^2 \delta^2 \left(\Delta - \frac{\delta}{3}\right)\right) D} \quad (2.11)$$

where  $G$  is the gradient strength,  $\Delta$  is the time elapsed between the pulses,  $\delta$  is the time width of the pulses and  $\gamma$  is the gyromagnetic ratio for the proton and  $D$  is the diffusion constant.  $S_0$  is the signal without diffusion weighting.  $A = S/S_0$  is the *attenuation*. Alongside multiple diffusion weighted images with different gradient directions, the  $S_0$  signal is acquired in an image taken with no diffusion weighting, often referred to as a b-zero image.

Equation 2.3.2 is normally summarised as:

$$\frac{S}{S_0} = e^{-bD} \quad (2.12)$$

where:

$$b = \left(\gamma^2 G^2 \delta^2 \left(\Delta - \frac{\delta}{3}\right)\right) \quad (2.13)$$

$b$  is normally referred to as the 'b-value' and is a commonly used summary parameter.

Equation presumes the gradients are ideal, i.e. they instantly switch to their maximum value. However, in real MRI scanners the gradients do not switch instantly, eddy currents are created by ramps at the beginning and end of a gradient pulse. Extra terms are required in equation 2.3.2 to account for this completely. This leads to numerous essential practical considerations. However, the basic theory remains the same so the discussion of gradient slew is beyond the scope of this thesis.

### 2.3.2.1 Q-space

A concept used in certain diffusion imaging techniques is that of *q-space* and the *q-vector*. Kärger and Heink [67] demonstrated that for an idealized pulse sequence with infinitesimally short gradient pulses measured signal attenuation  $A(\mathbf{q}) = S(\mathbf{q})/S_0$  is the 3-D Fourier transform of the diffusion scatter pattern  $p(\mathbf{r})$ :

$$A(\mathbf{q}) = \int_{\mathbb{R}^3} p(\mathbf{r}) \exp(-i\mathbf{q}^T \mathbf{r}) d\mathbf{r} = \mathcal{F}[p(\mathbf{r})] \quad (2.14)$$

Where:

$$\mathbf{q} = \gamma \delta \mathbf{G} \quad (2.15)$$

The set of all 3D  $q$ -vectors is referred to as  $q$ -space, a concept that was formalised by Callaghan in 1992 [20]. This concept is used in  $q$ -space imaging and other diffusion techniques such as diffusion spectrum imaging (DSI) [125, 124] and  $q$ -ball imaging [120, 122].

## 2.4 Modelling white matter architecture

In order to successfully extract information about tissue structure, it is necessary to model how the tissue structure affects the DW-MRI signal. A mathematical model relates the measured signal with specific tissue properties which are of interest in a parsimonious manner. The tissue properties are often represented by spacial distributions or parameters which relate to various identifiable physical features of the tissue, for example, the size or density of cells or the orientational arrangement.

### 2.4.1 The diffusion tensor

The earliest model conceived is the aforementioned diffusion tensor (DT) which remains widely used [113, 9]. It provides a measure of diffusion anisotropy which indicates structural details of the tissue and also a principal direction which indicates an average fibre direction in white matter. The diffusion tensor model fits a covariance matrix to the measured signals, characterising the diffusion in a particular reference frame. The DT model uses a 3x3 covariance matrix:

$$\mathbf{D} = \begin{bmatrix} D_{xx} & D_{xy} & D_{xz} \\ D_{xy} & D_{yy} & D_{yz} \\ D_{xz} & D_{yz} & D_{zz} \end{bmatrix} \quad (2.16)$$

The diffusion tensor is, by definition, symmetric positive definite, hence there are only 6 unknown elements to determine. The diffusion tensor can be coupled with the diffusion weighted signal using the  $b$ -matrix, which is analogous to the scalar  $b$ -factor.

$$\frac{I_2}{I_1} = e^{-\mathbf{bD}} \quad (2.17)$$

where:

$$\mathbf{b} = \begin{bmatrix} b_{xx} & b_{xy} & b_{xz} \\ b_{xy} & b_{yy} & b_{yz} \\ b_{xz} & b_{yz} & b_{zz} \end{bmatrix} \quad (2.18)$$

equation 2.17 can be expanded:

$$\frac{I_2}{I_1} = \exp(-b_{xx}D_{xx} - b_{yy}D_{yy} - b_{zz}D_{zz} - 2b_{xy}D_{xy} - 2b_{xz}D_{xz} - 2b_{yz}D_{yz}) \quad (2.19)$$

As there are 6 unknown elements to the diffusion tensor, at least 6 diffusion encoded images are required to resolve the equation in each voxel (7 if we include the  $b = 0$  image). The directions chosen must be non-collinear and non-coplanar. However, if only 6 images are used, the data will be fit exactly, including noise, hence generally, many more than 6 diffusion encoding directions are used.

The tensor can be estimated via a simple ordinary least squares (OLS) approach. This is a very simple and efficient way to fit the diffusion tensor, however, it is not necessarily the best. Alternative approaches opt for weighted least squares (WLS) [10], non-linear least squares or outlier rejection [24].

The tensor model captures the anisotropic diffusion profile in the presence of coher-

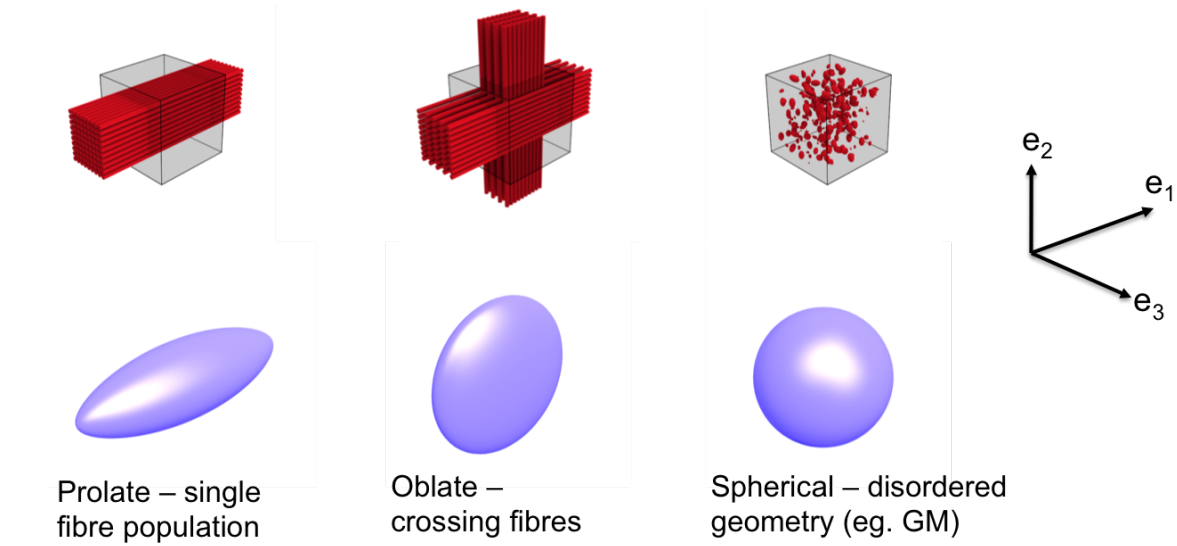


Figure 2.15: Illustration of diffusion profiles in varying tissue geometries. The tensor profile is shown in the case of a single, coherent bundle of fibres, crossing fibres, and disordered geometry such as a region of GM.

ently oriented fibres, and also yields several scalar measures reflecting tissue structure, quantifying diffusion properties such as diffusion anisotropy. A major limitation however is the inability of the diffusion tensor to capture meaningful information in situations where the fibre architecture inside a voxel is not a single, coherent bundle, but could be one of a number of other possible configurations. Some examples of diffusion tensor profiles corresponding to distinct tissue geometries are given in Figure 2.15.

#### 2.4.2 Extracting informative measures from the diffusion tensor

Several useful things can be extracted from the diffusion tensor which can be used to infer properties of tissue structure. First and foremost, as the diffusion tensor  $D$  is symmetric positive definite it can be decomposed into real eigenvalues  $\lambda_i$  and corresponding eigenvectors  $\mathbf{e}_i$ :

$$\mathbf{D} = \mathbf{E} \mathbf{\Lambda} \mathbf{E}^{-1} \quad (2.20)$$

$$\mathbf{E} = \begin{bmatrix} \mathbf{e}_1 & \mathbf{e}_2 & \mathbf{e}_3 \end{bmatrix} \quad (2.21)$$

$$\Lambda = \begin{bmatrix} \lambda_1 & 0 & 0 \\ 0 & \lambda_2 & 0 \\ 0 & 0 & \lambda_3 \end{bmatrix} \quad (2.22)$$

If we assume by convention that  $\lambda_1 > \lambda_2 > \lambda_3$  then the eigenvector  $\mathbf{e}_1$  with the biggest eigenvalue identifies the dominant diffusion direction and can be interpreted (cautiously) as the probable dominant fibre direction in WM. Caution must be used in this interpretation as there may be confounding factors which could make the assumption that the principal eigenvector denotes the dominant fibre direction in a voxel such as a partial volume of GM or CSF, or multiple fibre populations within the voxel.

Informative scalar measures can also be derived from the diffusion tensor:

- The mean diffusivity (MD):

$$MD = \frac{\lambda_1 + \lambda_2 + \lambda_3}{3} = \langle \lambda \rangle \quad (2.23)$$

- The fractional anisotropy (FA):

$$FA = \sqrt{\frac{3}{2}} \frac{\sqrt{(\lambda_1 - \langle \lambda \rangle)^2 + (\lambda_2 - \langle \lambda \rangle)^2 + (\lambda_3 - \langle \lambda \rangle)^2}}{\sqrt{\lambda_1^2 + \lambda_2^2 + \lambda_3^2}} \quad (2.24)$$

- The linear coefficient (CL) [127], which gives a measure of the linearity of the diffusion tensor profile:

$$CL = \frac{\lambda_1 - \lambda_2}{\lambda_1} \quad (2.25)$$

- The planar coefficient (CP) [127], which gives a measure of the planarity of the diffusion tensor profile:

$$CP = \frac{\lambda_2 - \lambda_3}{\lambda_1} \quad (2.26)$$

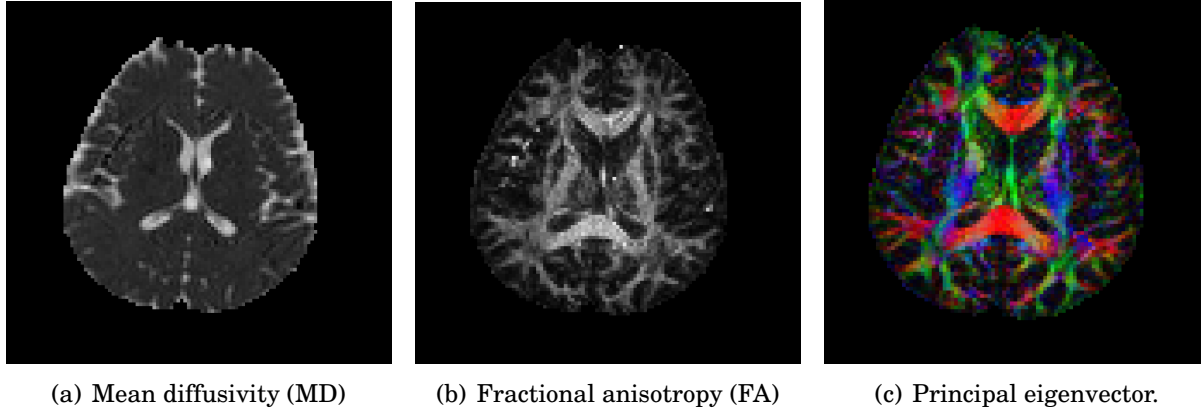


Figure 2.16: Mean diffusivity (MD) 2.16(a), fractional anisotropy (FA) 2.16(b) and direction of principal eigenvector 2.16(c). The principal eigenvector is displayed using the common anatomically-related colour scheme of blue - inferior→superior, red - left→right and green - posterior→anterior.

- The spherical coefficient (CS) [127], which gives a measure of the sphericity of the diffusion tensor profile:

$$CS = \frac{\lambda_3}{\lambda_1} \quad (2.27)$$

FA and MD are rotationally invariant diffusion metrics which are commonly used in research and clinical applications for investigating pathology [38] or functional differences between individuals [69]. FA, MD and principal eigenvector maps are shown in Figure 2.16. FA is typically high in dense, coherently oriented white matter, as is CL. CP is typically high in regions of crossing fibres and CS is higher in regions of CSF and GM, these can all be highly useful metrics depending upon the application.

A major limitation of the diffusion tensor is that it assumes Gaussian diffusion, an assumption which breaks down in populations of water molecules restricted inside cell boundaries. Over long enough timescales, the diffusion characteristics of these water molecules deviate from Gaussian, hence this can lead to modelling errors with the diffusion tensor.

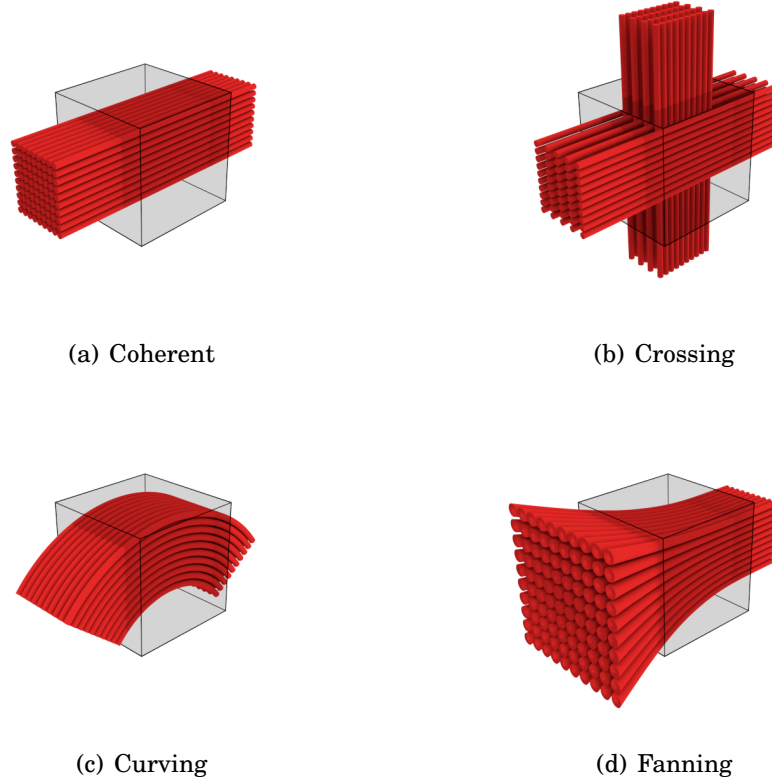


Figure 2.17: Illustrations of possible configurations of sub-voxel fibre architecture.

### 2.4.3 Complex sub-voxel fibre architecture

The characteristic size of the primary structures we are examining in DWI for tractography, the axons, is in the range  $0.5\text{-}20\mu\text{m}$ . This is 2-3 orders of magnitude below the DW-MRI resolution, which is typically  $2\text{-}3\text{mm}$  for common DW-MRI acquisitions. Therefore complexities can arise in the tissue structure lying within the boundaries of any particular voxel. The simplest models, including the diffusion tensor, can only comprehensively summarise the white matter fibre architecture within a voxel if the fibre configuration conforms to a single, highly coherent bundle of parallel axons, which does not deviate in direction across the entire volume of the voxel, as demonstrated in Figure 2.17a). Figures 2.17b-c) illustrate other conceivable sub-voxel architectures which can arise and are known to exist in white matter. The white matter fibres within a voxel may cross (Figure 2.17b), bend (Figure 2.17c) or fan (Figure 2.17d) within the boundaries of a single voxel.

By using only a single, unique direction to summarise the sub-voxel fibre architec-

ture illustrated in Figures 2.17 b)-d), the underlying white matter structure is misrepresented, and this leads to false negative or false positive connections in resulting tractography based on these models. In many cases of complex sub-voxel white matter architecture, the basic diffusion tensor model can be actively misleading [121, 103]. For example, in the case of two fibre bundles crossing at an acute angle, the diffusion tensor will actually yield the average orientation of the two combined, and no useable information relating to either individual bundle.

To address the limitations of these simplistic models of white matter, DW-MRI research has focussed on the development of more comprehensive models, which capture the extra structural complexity of voxels with complex sub-voxel fibre architecture. One of the primary focusses has been on capturing crossing fibre structure, where two distinct fibre populations cross inside the voxel, the fibres of each population interdigitating with those of the alternate population(s). Crossing fibres are an inherent complication in DW-MRI, as it is known that fibre populations intersect each other at a far smaller scale than any DW-MRI resolution conceivable in the foreseeable future could resolve.

#### **2.4.4 Multi-compartment models**

The first step towards more comprehensive modelling of the tissue in a voxel is compartmentalisation. The assumption is that the water inside the voxel can be broken up into separate compartments or 'partial volumes', each of which exhibits a different diffusion behaviour depending on its specific environment. Each compartment subsequently has a unique contribution to the resulting DW-MRI signal. The measured DW-MRI signal is therefore assumed to be a sum of the signal contributions for all compartments. For example, water diffusion inside fibres will exhibit a highly anisotropic diffusion behaviour, as it is restricted almost entirely to diffusing along the axis of the fibre, while the water outside and around fibres can percolate through the fibrous lattice, and therefore will exhibit more isotropic diffusion properties. Compartmentalisation separates these two water populations to be treated with a different mathematical model, which more

accurately captures the diffusion behaviour.

#### 2.4.4.1 Ball and stick model

A prominent example of a DW-MRI model which features such a compartmentalisation is the Ball and Stick model [14]. The ball and stick model models the diffusion of the intra-cellular water inside parallel axons as an infinitely thin stick and models the extra cellular water which exists around the axons as a 'ball', which is simply a compartment modelling hindered, isotropic diffusion. These two separate compartments could be considered as special cases of the diffusion tensor, with the stick being a diffusion tensor for which the diffusion along all eigenvectors except the principle direction is zero, and the ball being an entirely isotropic tensor with the diffusion along all eigenvectors being equal.

The signal  $S_i$  for the  $i^{th}$  diffusion weighted acquisition with gradient direction  $\mathbf{r}_i$  the signal is given by:

$$S_i = S_0((1-f)\exp(-b_i d) + f \exp(-b_i d \mathbf{r}_i^T \mathbf{R} \mathbf{R}^T \mathbf{r}_i)) \quad (2.28)$$

where  $S_0$  is the MR signal without diffusion weighting,  $d$  is the diffusivity,  $b_i$  and  $\mathbf{r}_i$  respectively are the b-value and gradient direction associated with the  $i^{th}$  MR acquisition.  $f$  is the volume fraction of the anisotropic compartment in the voxel, and  $\mathbf{R} \mathbf{R}^T$  is the anisotropic diffusion tensor along the principle diffusion direction  $(\theta, \phi)$ :

$$A = \begin{bmatrix} 1 & 0 & 0 \\ 0 & 0 & 0 \\ 0 & 0 & 0 \end{bmatrix} \quad (2.29)$$

The ball and stick model represents one of the simplest ways to compartmentalise a tissue model. However it doesn't in itself approach the aforementioned complexities of complex sub-voxel fibre architecture such as crossing, curving or fanning as it still relies on the assumption of a single, coherent fibre population which does not deviate over the

volume of the voxel.

To address the issue of multiple fibre populations per voxel for a simple compartment model such as the ball and stick is conceptually trivial. The model can be modified to incorporate multiple 'stick' compartments to represent each distinct fibre population [13]:

$$\mu_i = S_0((1 - \sum_{j=1}^N f_j) \exp(-b_i d) + \sum_{j=1}^N f_j \exp(-b_i d \mathbf{r}_i^T \mathbf{R}_j \mathbf{A} \mathbf{R}_j^T \mathbf{r}_i)) \quad (2.30)$$

Here, the elements with subscript  $j$  represent the respective elements given in equation 2.28, for the  $j^{th}$  of  $N$  fibre populations. While in theory this extension is a simple one, in practice it is not simple to apply. The primary issue is one of model selection. This model actually represents an effectively infinite series of possible models, one for each allowable value of  $N$ , which can stem from 0 (no fibre population) to  $\infty$  fibre populations. A very large number of fibre bundles is clearly physically unrealistic and a significant concern when allowing a flexible number of fibre populations is overfitting. Hence many different approaches are taken to appropriately and robustly decide on the number of fibre populations, from Bayesian techniques such as automatic relevance determination (ARD) [13] and model ranking via the Bayesian information criterion (BIC) [82], to frequentist methods using bootstrapping [100]. An in depth discussion of this issue is beyond the scope of this thesis and can be found in the respective references.

#### 2.4.4.2 Multi-tensor model

A similar solution for crossing fibres to the ball and multi-stick representation, which simply uses multiple instances of a model used to represent single fibre bundles are multi-tensor models. A multi-tensor model could be thought of as a generalisation of the ball and multi-stick model, with the restriction that one tensor must be isotropic and the other tensors must have non-zero diffusivity along only one axis released. The caveat of this generalisation is that the model has more parameters which must be estimated, which can have challenging practical consequences. Therefore implementations of multi-tensor models tend to resort to some restrictions on the tensors such as cylindri-

cal symmetry [6] or fixing eigenvalues [121].

These conceptually simple (but often practically challenging) approaches to modelling multiple fibre populations per voxel have been generally successful and widely exploited in diffusion imaging. However, a major limitation of these models and related approaches, especially when considering their application in tractography, is that they still fail to capture the sub-voxel fibre architecture represented in Figures 2.17 c) and d). From the parameters describing each fibre population, from the aforementioned multi-fibre models, only the orientation of the  $j^{th}$  bundle  $(\theta_j, \phi_j)$  can be extracted from the estimated parameters of the model, in the case of the fanning and curving represented in Figures 2.17 c and d, a continuous range of fibre orientations exists in the voxel, which cannot be accurately summarised by a singular orientation estimate, or a limited number of them.

### 2.4.5 Non-parametric approaches

A set of alternative approaches to modelling sub-voxel fibre architecture exists which releases the dependence on simplistic geometric models of fibre architecture. These are normally grouped under the definition of 'non-parametric' approaches. These approaches aim to estimate an 'orientation distribution function' (ODF) from the diffusion data. The ODF is a spherical distribution function which represents, as a probability distribution, the probability of something having a particular given orientation and is effectively a 3 dimensional, spherical realisation of a probability distribution function (PDF). What that 'something' is depends upon the method. There are several techniques which estimate a 'diffusion ODF' (dODF), which is the probability that a diffusing water molecule moves in a particular direction. In free water the dODF would be uniform over the sphere, in a single coherent bundle of fibres, the dODF would be sharply peaked along the direction of the fibres as this is the direction in which diffusion is least restricted. Alternative techniques estimate the 'fibre ODF' (fODF) which represents the probability that a fibre exists in the voxel with a particular given orientation. As with the dODF, in the case of a

single coherent fibre bundle, the fODF would be sharply peaked along the fibre direction (in theory, for a bundle of absolutely parallel fibres it would be a delta function). However, in the case of free water, theoretically, the fODF should be zero throughout the sphere, as there are no fibres.

This leads to an obvious realisation when it comes to the applicability to tractography, that the fODF is inherently more useful, as it attempts to directly represent the structural organisation of the fibres we are trying to track. Information useful to tractography can be extracted from dODFs. For example, the peaks in the function can be assumed to represent the mean directions of fibre bundles, however, this is an indirect measure of fibre architecture and summarises the fibre architecture in the voxel in a similarly limited fashion to the multi-compartment models mentioned in section 2.4.4. The fODF directly represents the estimated distribution of fibre orientations inside each voxel directly and therefore encapsulates the information we require for tractography much more comprehensively.

#### 2.4.5.1 Diffusion spectrum imaging

Diffusion spectrum imaging (DSI) [125, 124] attempts to reconstruct the diffusion scatter pattern  $p$  directly and hence estimates the dODF. The diffusion scatter pattern is the 3-dimensional displacement of water molecules and its properties provide insights into the underlying tissue structure in which the water is diffusing. DSI estimates  $p$  by taking the inverse Fourier transform of the q-space samples  $A(\mathbf{q})$ :

$$p(\mathbf{r}) = \mathcal{F}^{-1}[A(\mathbf{q})](\mathbf{r}) \quad (2.31)$$

DSI samples q-space using a grid based scheme. The Fourier transform of these q-space samples then yields samples of the diffusion PDF on a grid of displacements  $\mathbf{x}$ . The dODF can then be reconstructed by projecting the samples from the grid onto a sphere:

$$\psi(\hat{\mathbf{x}}) = \int_0^\infty (\alpha \hat{\mathbf{x}}) d\alpha \quad (2.32)$$

Where  $\psi(\hat{\mathbf{x}})$  is the dODF evaluated on the unit vector  $\hat{\mathbf{x}}$ .

The primary limitation of DSI is the acquisition requirements to cover q-space with a grid which is typically orders of magnitude more than typical DTI acquisitions, normally 500-1000.

#### 2.4.5.2 Q-ball imaging (QBI)

Q-ball imaging [120, 122] estimates the dODF using a spherical q-space sampling scheme, which is much more efficient than the grid-based scheme used in DSI. Q-space is sampled using a high angular resolution (HARDI) acquisition, using q-space samples with a fixed radius.

Q-ball approximates the dODF  $\psi(\hat{\mathbf{r}})$  using the Funk-Radon transform (FRT). The FRT of a spherical function  $f(\hat{\mathbf{r}})$  is the integral of  $f(\hat{\mathbf{r}})$  over the great circle  $\mathcal{C}(\hat{\mathbf{r}})$  that lies in the plane perpendicular to  $\hat{\mathbf{r}}$  through the origin.

$$\psi(\hat{\mathbf{r}}) = \int_{\mathcal{C}(\hat{\mathbf{r}})} A(\mathbf{q}) d\hat{\mathbf{q}} \quad (2.33)$$

Radial basis functions can be used to represent  $\psi(\hat{\mathbf{r}})$ . Alternative methods employ a modified spherical harmonic basis to represent  $\psi(\hat{\mathbf{r}})$  [53, 34], which has the advantage that the FRT can be performed analytically.

#### 2.4.5.3 Persistent angular structure MRI (PAS-MRI)

PAS-MRI [57, 4, 102] seeks to compute a spherical function related to the fODF as a projection of  $p$  onto the sphere. Using the same efficient spherical HARDI q-space sampling as Q-ball imaging, PAS-MRI seeks to recover the persistent angular structure (PAS) which exists within all isoprobability contours of the diffusion scatter pattern  $p$ .

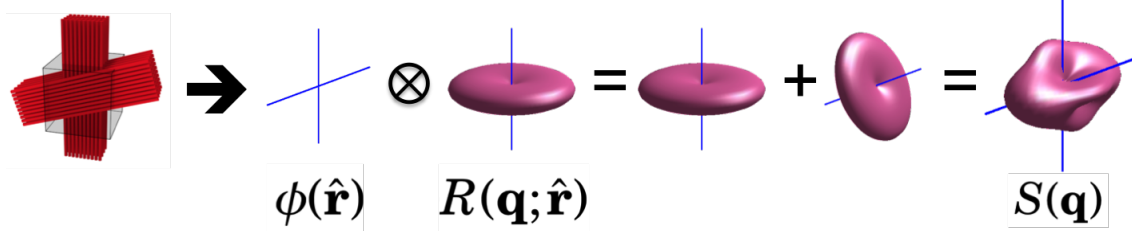


Figure 2.18: Illustration of spherical deconvolution. The single fibre response function  $R(\mathbf{q}; \hat{\mathbf{r}})$  is convolved with the ground truth fODF  $\phi(\hat{\mathbf{r}})$  to give the signal  $S(\mathbf{q})$ .

#### 2.4.5.4 Spherical deconvolution

The most prevalent non-parametric method of directly estimating the fODF is spherical deconvolution [56, 117, 66, 32, 8, 96]. Spherical deconvolution relies on the assumption that the diffusion signal  $S(\mathbf{q})$  can be modelled as the convolution of the fODF,  $\phi(\hat{\mathbf{r}})$ , with a response function, which is the signal measured from a single fibre population with orientation  $\hat{\mathbf{r}}$ :

$$S(\mathbf{q}) = \int \phi(\hat{\mathbf{r}}) R(\mathbf{q}; \hat{\mathbf{r}}) d\hat{\mathbf{r}} \quad (2.34)$$

Spherical deconvolution can be seen as an extension of the multi-stick or multi-tensor model, with the allowable number of fibre populations increased to infinity and represented by a continuous spherical distribution. Figure 2.18 illustrates the concept, a ground truth fODF which consists of 2 distinct fibres when convolved with the single fibre response function gives the diffusion signal.

This then becomes an inverse problem to estimate the feature of interest, the fODF. The deconvolution operation can be performed by representing the fODF using a set of spherical harmonics. The set of spherical harmonics used is restricted to those which produce an antipodally symmetric, real-valued function. The operation can be simplified to a matrix multiplication:

$$\mathbf{s} = \mathbf{R}\mathbf{f} \quad (2.35)$$

where  $\mathbf{f}$  and  $\mathbf{s}$  are the  $n_c \times 1$  spherical harmonic coefficient vectors of the fODF,  $\phi(\hat{\mathbf{r}})$  and the signal  $S(\mathbf{q})$  respectively and  $\mathbf{R}$  is the rotational harmonic matrix of  $R(\mathbf{q}; \hat{\mathbf{r}})$ . Assuming that the response function is axially symmetric, it can be shown that  $\mathbf{R}$  is a diagonal matrix. the elements of  $\mathbf{R}$  can be calculated from the spherical harmonic coefficients of the response function [56, 117]. Therefore it follows by inverting equation 2.35, we get:

$$\mathbf{f} = \mathbf{R}^{-1} \mathbf{s} \quad (2.36)$$

Spherical deconvolution can be used to provide measures characterising white matter diffusion, to reflect scalar measures from the DT such as FA and MD [33].

The basic spherical deconvolution approach is highly susceptible to noise, which produces high angular resolution artefactual lobes in the recovered fODF. This includes negative lobes, which cannot be interpreted as physically plausible. Low pass filtering the harmonic series can mitigate this to some extent at the expense of angular resolution. However, a non-negativity constraint drastically reduces noise-sensitivity and increases the physical relevance of the resultant fODF. This is the basis of the 'constrained spherical deconvolution' (CSD) technique [117].

## 2.4.6 Advanced parametric approaches

The extension of the simple multicompartment models discussed in section 2.4.4 from a limited set of fibre directions to a continuous distribution on the sphere opens the possibility of capturing sub-voxel fibre structures exhibiting continuous orientation dispersion such as the fanning and bending configurations demonstrated in Figures 2.17 c) and d). By their nature these fibre configurations require a continuous spherical distribution to represent them.

Recent work has proposed advanced parametric models which capture sub-voxel orientation dispersion [108, 135, 65, 115]. These models make use of parametrized, continuous, spherical distributions which are suitable for modelling orientation dispersion. The

spherical distributions used feature a mean axis and concentration parameters which control the spread of the probability distribution around this mean direction. In [135], the Watson distribution is used, while in [108, 65, 115] the Bingham distribution is used. The Bingham distribution is a generalisation of the Watson distribution with elliptical contours (see Figure 2.20). The key difference is that the Watson distribution is cylindrically symmetric around the mean direction, while the Bingham distribution is able to capture anisotropic orientation dispersion which doesn't exhibit cylindrical symmetry around the mean axis. The Bingham distribution is therefore able to capture orientation dispersion which exists in only one plane. This planar dispersion is an expected feature of white matter. The Bingham distribution is shown to explain DW-MRI data more accurately than the Watson distribution [115]. Therefore it is a better choice of model for tractography applications. Figure 2.19 shows visualisations of Watson and Bingham distributions for comparison, showing the primary distinction of cylindrical symmetry for the Watson distribution which is a special case of the more general Bingham distribution.

The Bingham distribution [16] is an antipodally symmetric function on the sphere with a mean direction  $\boldsymbol{\mu}$  and two concentration parameters  $\kappa_1$  and  $\kappa_2$  which control the degree of dispersion along the two axes orthogonal to the mean direction  $\boldsymbol{\mu}_1$  and  $\boldsymbol{\mu}_2$  respectively:

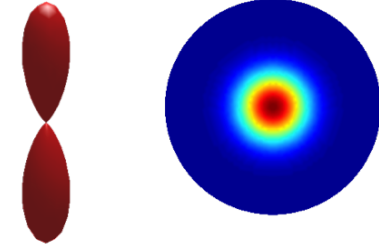
$$f(\mathbf{n}) = F_1\left(\frac{1}{2}, \frac{3}{2}, \kappa_1, \kappa_2\right)^{-1} \exp[\kappa_1(\boldsymbol{\mu}_1 \cdot \mathbf{n})^2 + \kappa_2(\boldsymbol{\mu}_2 \cdot \mathbf{n})^2], \quad (2.37)$$

where  $F_1$  is the hypergeometric function (note:  $F_1(1/2, 3/2, \kappa_1, \kappa_2)$  is a number, not a function). The factors of 1/2 and 3/2 are set as such for defining directions on a 3 dimensional sphere. The Bingham distribution can be further generalised for higher-dimensional hyperspheres.

The key advantage of utilising such a parametrized model of dispersion is that it is able to capture orientation dispersion representative of the fanning and curving fibre configurations shown in Figures 2.17 c) and d) with a limited number of degrees of freedom.

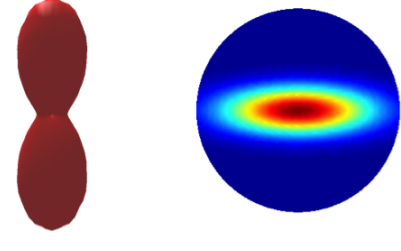
$$f(\mathbf{n}) = W(\mathbf{n}; \mu, \kappa) = F_1\left(\frac{1}{2}, \frac{3}{2}, \kappa\right)^{-1} \exp[\kappa(\mu \cdot \mathbf{n})^2]$$

$$f(\mathbf{n}) = F_1\left(\frac{1}{2}, \frac{3}{2}, \kappa_1, \kappa_2\right)^{-1} \exp[\kappa_1(\mu_1 \cdot \mathbf{n})^2 + \kappa_2(\mu_2 \cdot \mathbf{n})^2]$$



$x \odot$   
 $y \rightarrow$   
 $z \uparrow$

(a) Watson distribution



$x \uparrow$   
 $y \rightarrow$   
 $z \odot$

(b) Bingham distribution

Figure 2.19: Comparison of Watson and Bingham distributions. The Watson distribution is governed by a single concentration parameter  $\kappa$  and is cylindrically symmetric while the Bingham distribution is governed by two concentration parameters  $\kappa_1$  and  $\kappa_2$ , allowing elliptical contours which can represent anisotropic dispersion. The Bingham distribution is a generalisation of the Watson distribution, with the Watson distribution being the special case of the Bingham distribution when  $\kappa_1 = \kappa_2$ .

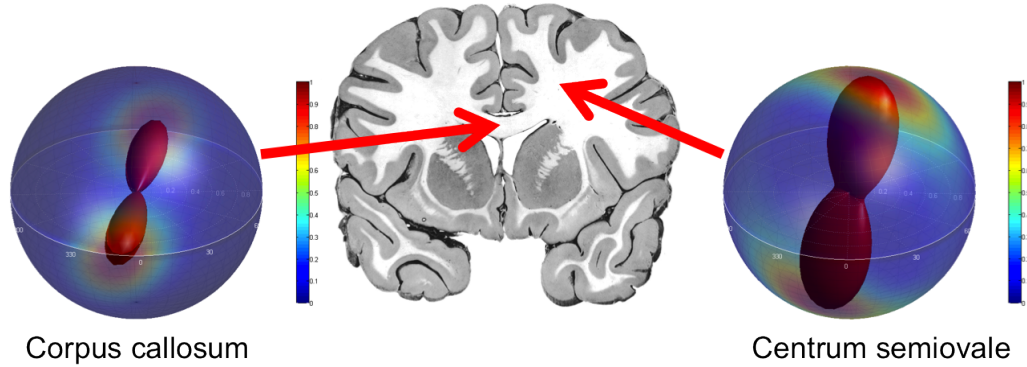


Figure 2.20: Bingham distributions fit to diffusion data using the NODDI technique. We see one example from the corpus callosum and another from the centrum semiovale, two areas with distinctly different dispersion characteristics. In the centrum semiovale, we see an example of anisotropic dispersion. The spheres show the Bingham distribution as both a red surface, for which the distance of a point on the surface to the origin is equal to the normalised PDF value defined for the unit vector between the surface point and the origin. The probability is also projected onto the transparent spheres, with the probability defined by the colour, blue being low probability and red being high probability. These are two useful ways of visualising spherical distributions.

5 parameters in total are required to define the Bingham distribution, two for the mean direction, one for the secondary axis (fanning axis) and two concentration parameters  $\kappa_1$  and  $\kappa_2$ . This is a significant advantage over the spherical deconvolution approach outlined in section 2.4.5.4, for which, due to the number of spherical harmonic coefficients the inverse problem is ill-posed. This makes spherical deconvolution highly susceptible to over-fitting and spurious fODF features due to noise. Various compromises are required to overcome this which sacrifice angular resolution.

Sotiropoulos *et al* demonstrate in [108] that a parametric model of dispersion using the Bingham distribution more robustly and more accurately captures sub-voxel fibre dispersion in simulations and real brain data when compared to alternative methods including CSD and PAS-MRI.

### 2.4.7 The NODDI tissue model

For the tractography methods developed later in this thesis, the NODDI model is chosen as a parametric model of fibre dispersion [135]. Therefore, in the following, we outline some of the main features of the NODDI model.

The NODDI technique was developed by Zhang *et al* in 2012 and originally utilised a Watson distribution to model neurite dispersion. NODDI is an abbreviation of 'neurite orientation dispersion and density imaging'. The technique was further developed using the Bingham distribution to model neurite dispersion more accurately. The Bingham distribution was shown to better explain DW-MRI data than the Watson distribution by comparison using the Bayesian information criterion (BIC) [115].

The Bingham NODDI model gives a spherical distribution in each voxel, which represents an estimate of the range of white matter fibre orientations bounded by the respective voxel. The Bingham distribution is capable of modeling anisotropic dispersion, so it can more accurately reflect the dispersion of WM fibres. We fit the Bingham model to diffusion data using an extension of the NODDI technique [135], which uses a multicompartment model, modelling CSF, an isotropic compartment (ball) and the fibrous

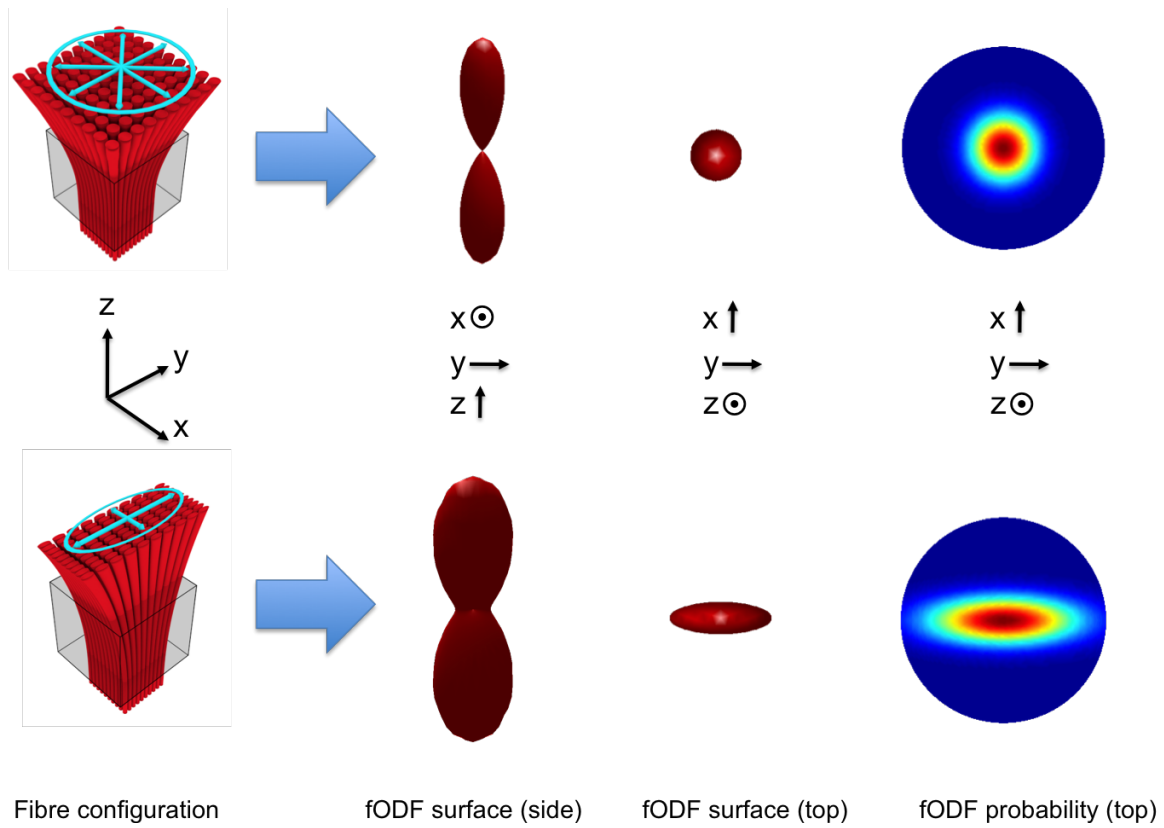


Figure 2.21: Different fibre configurations with corresponding ODFs. The upper row shows cylindrically symmetric dispersion, which can be accurately summarised by a cylindrically symmetric ODF such as a Watson distribution. The lower row shows anisotropic dispersion, the dispersion along one axis is greater than that along the orthogonal axis. This requires an ODF with elliptical contours such as the Bingham distribution to represent the dispersion correctly.

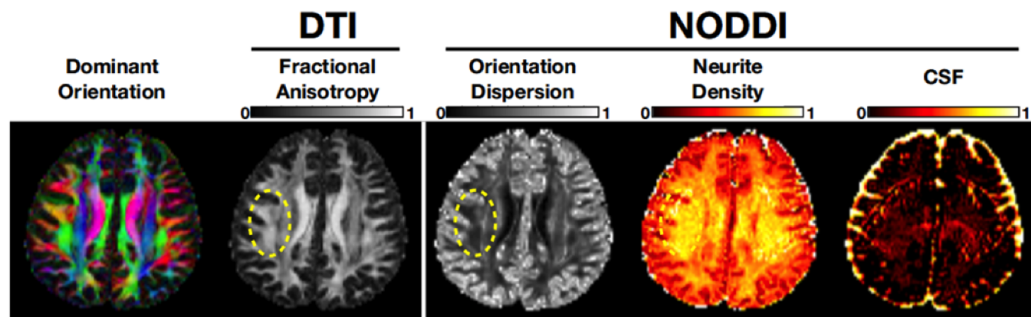


Figure 2.22: Separate compartments contributing to the diffusion signal, disambiguated by NODDI: fibrous compartment with dispersion, isotropic compartment and CSF. Diagram adapted from [135].

compartment sperately.

Further details on the NODDI model and acquisition design can be found in [135, 115], what follows is an overview of the important features. The NODDI model is a multi-compartment model which disambiguates a conflation of multiple tissue features giving rise to the diffusion weighted signal.

The normalised signal  $A$  can be writen as (following the notation in [135]):

$$A = (1 - v_{iso})(v_{ic}A_{ic} + (1 - v_{ic})A_{ec}) + v_{iso}A_{iso} \quad (2.38)$$

where  $A_{ic}$  and  $v_{ic}$  are the normalised signal and volume fraction of the intra-cellular compartment,  $A_{ec}$  is the normalised signal of the extra-cellular compartment and  $A_{iso}$  and  $v_{iso}$  are the normalised signal and volume fraction of the CSF compartment.

#### 2.4.7.1 Intra-cellular compartment

The intra-cellular compartment is modelled by a distribution of *sticks* [14] (see section 2.4.4). The model is designed to capture fibre structure which can be coherent or dispersed, such as the fanning structures present in the corona-radiata. The normalised signal for the intracellular compartment  $A_{ic}$  is given by:

$$A_{ic} = \int_{S^2} f(\mathbf{n}) \exp(-bd_{\parallel}(\mathbf{q} \cdot \mathbf{n})^2) d\mathbf{n} \quad (2.39)$$

where  $\mathbf{q}$  and  $b$  are the gradient direction and  $b$ -value.  $f(\mathbf{n})d\mathbf{n}$  gives the probability of sticks having orientation  $\mathbf{n}$  and  $\exp(-bd_{\parallel}(\mathbf{q} \cdot \mathbf{n})^2)$  gives the signal attenuation due to un-hindered diffusion along a stick with intrinsic diffusivity  $d_{\parallel}$  and orientation  $\mathbf{n}$ . The orientation distribution  $f(\mathbf{n})$  is modelled with a Bingham distribution as given in equation 2.37.

#### 2.4.7.2 Extra-cellular compartment

The extra-cellular compartment is modelled with anisotropic (Gaussian) diffusion as a cylindrically symmetric tensor. The diffusion in the extra-cellular compartment is hindered by the presence of the neurites and their distribution, hence the intra-cellular and extra-cellular compartments are coupled by the orientation distribution function  $f(\mathbf{n})$ :

$$\log A_{ec} = -b\mathbf{q}^T \left( \int_{S^2} f(\mathbf{n}) D(\mathbf{n}) d\mathbf{n} \right) \mathbf{q} \quad (2.40)$$

$D(\mathbf{n})$  is a cylindrically symmetric tensor with principal direction of diffusion  $\mathbf{n}$ .  $d_{\parallel}$  (parallel to  $\mathbf{n}$ ) is the same as  $d_{\parallel}$  for the intra-cellular compartment and the perpendicular diffusivity is set using the tortuosity model [114]:  $d_{\perp} = d_{\parallel}(1 - v_{ic})$ .

#### 2.4.7.3 CSF compartment

The CSF compartment is modelled as isotropic Gaussian diffusion with diffusivity  $d_{iso}$ :

$$A_{CSF} = \exp(-bd_{iso}) \quad (2.41)$$

### 2.4.8 NODDI protocol and fitting

An optimized protocol for data acquisition is derived using the experiment design optimization procedure detailed in [5]. The optimization suggests two HARDI shells, one with 30 directions at a low  $b$ -value of 711 s/mm<sup>2</sup> and another with a higher  $b$ -value of 2855 s/mm<sup>2</sup>. The NODDI model is fit to the DW-MRI data using an adapted version of the fitting routine described in [7], which involves a three stage process of an initial grid search, followed by gradient descent, using a Rician noise model. The final MCMC step used in [7] is omitted due to it having a high computational and time expense while yielding negligible effect on the accuracy of the fitted NODDI parameters.

Summary of NODDI model parameters:

- $v_{ic}$ : intra-cellular volume fraction
- $v_{iso}$ : isotropic volume fraction
- $\kappa_1$  and  $\kappa_2$ : concentration parameters of the Bingham distribution
- $\mu_1$  and  $\mu_2$ : mean and fanning axis of the Bingham distribution
- $d_{\parallel}$ : intrinsic free diffusivity
- $d_{iso}$ : isotropic diffusivity

The diffusivities are fixed to their respective typical values *in vivo*:  $d_{\parallel} = 1.7 \times 10^{-3}$  and  $d_{iso} = 3.0 \times 10^{-3}$  as in [7] and [134]. Further details can be found in [135].

## 2.4.9 NODDI metrics

### 2.4.9.1 Orientation dispersion index (Watson distribution)

The original NODDI model, which uses the Watson distribution for the fibrous compartment, characterises orientation dispersion with a metric, known as the 'orientation dispersion index' (ODI) which is given by:

$$ODI = \frac{2}{\pi} \arctan(1/\kappa) \quad (2.42)$$

where  $\kappa$  is the concentration parameter of the Watson distribution used to define orientation dispersion as in the original NODDI model [135].

### 2.4.9.2 Orientation tensor and dispersion anisotropy index (Bingham distribution)

The extension of the NODDI model to use the Bingham distribution introduces new metrics to quantify dispersion and dispersion anisotropy [115, 116]. The metrics are

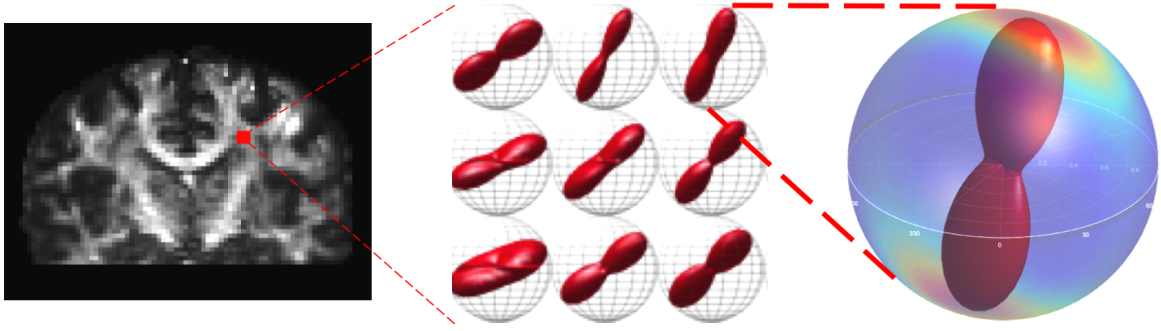


Figure 2.23: Bingham distributions fitted to data in the brain using NODDI.

derived from the orientation tensor (OT). The OT is defined as the scatter matrix of an ODF such as the Bingham distribution:

$$T_{i,j} = \int_{S^2} \mathbf{n}_i f(\mathbf{n}) \mathbf{n}_j d\mathbf{n} \quad (2.43)$$

The primary and secondary eigenvalues of the OT,  $\tau_1$  and  $\tau_2$ , are functions of the concentration parameters  $\kappa_1$  and  $\kappa_2$  with corresponding eigenvectors  $\boldsymbol{\mu}_1$  and  $\boldsymbol{\mu}_2$  which are exactly those in equation 2.37. The dispersion can then be quantified by the primary eigenvalue of the OT,  $\tau_1$ , which is inversely proportional to the ODI in the Watson NODDI model. A second metric, the dispersion anisotropy index (DAI), quantifies the dispersion anisotropy and is defined by  $DAI = \frac{\tau_2 - \tau_3}{\tau_1}$ .

## 2.5 Summary and conclusion

This chapter has given a summary of the various methods of modelling WM fibre architecture using measurements from DW-MRI. There are a myriad of options for modelling, and this chapter covers only a representative subset of all the models available in DW-MRI research. The choice of model can depend on the application. Factors to be considered include the information we wish to gain from modelling the white matter architecture and the application context. For example, a simple model like the diffusion

tensor may be sufficient to describe the changes in neural tissue a clinical researcher is seeking to observe, however, as the model is overly simplistic, it provides inconsistent information in areas where it is not sufficient to describe various features of the tissue, including partial volumes of CSF or GM and WM, or crossing, fanning or curving fibres. In the case that more complex fibre architecture is being studied, a more complex model may be appropriate, such as CSD to resolve crossing fibres and derive tract-specific metrics [33]. CSD may not be appropriate in cases where the acquisition is not adequate, CSD may not work well on noisy data with a limited number of directions, in which case a simpler model may be more robust and provide usable metrics. Judicious choices must be made as more complex models come hand in hand with more fitting complexities and the requirement for higher quality acquisitions.

**Tractography applications:** With the advent of better MRI technology, acquisition design and processing techniques to refine the data, high quality HARDI acquisitions are becoming commonplace in research and viable in clinical applications. Hence DW-MRI models are progressing towards better descriptions of neural tissue structure as is the case with the latter models covered in this chapter in sections 2.4.5 and 2.4.6. For tractography, using the model which most accurately describes white matter fibre architecture is the most appealing option.

The DT and ball and stick are too simple to realistically extract all the information required for tractography and often a conflation of various factors affects the accuracy of the orientational estimates due to modelling errors. These models fail to capture complex fibre architectures such as fanning and crossing. Using multiple fibrous compartments in multi-stick or multi-tensor models can improve upon this, but the over-simplicity of these models can cause identifiability issues between volume fractions and individual diffusivity parameters.

Non-parametric approaches offer an elegant method of extracting numerous features of the fibre architecture of the voxel and can resolve crossing fibres. dODF techniques can

provide information useful for tractography, peaks can be extracted fairly reliably from the dODF, although the dODF in itself is not explicitly useful for tractography as it characterises features of water diffusion and does not directly characterise the distribution of fibre orientations. fODF techniques are much more applicable to tractography as the fODF is in itself useful as a measure of the distribution of WM fibres traversing a voxel. Therefore directions can be directly sampled from the fODF for streamline propagation in probabilistic tractography. fODF techniques can suffer from errors in the recovered fODF due to noise and can misidentify fanning and crossing fibre configurations [83].

The parametric models described in section 2.4.6 offer the most promising avenues for tractography. These models accurately describe fanning fibre architecture with a limited number of parameters and can capture dispersing fibre structure more robustly and accurately than competing non-parametric methods [108].

# Chapter 3

## Tractography

### 3.1 Tractography

Tractography is the process of piecing together the directional information derived from the methods described in section 2.4 to infer connectivity between distinct functional brain regions. Starting from a given seed point within the brain, a tractography algorithm integrates a streamline through the image volume by extracting directional information from the data in the voxel corresponding to each respective location on the streamline. As the streamline has traced the directional information derived from DW-MRI data, which is assumed to represent the direction of WM fibres at the physical location of each voxel, that streamline can then be assumed to represent a potential connection between the seed point and the termination location of the given streamline. Alternatively, the spatial form of the streamline itself may be interpreted as representing the structure of a WM fascicle, which has implications in surgical planning, where certain WM features may be important to avoid in surgical procedures to avoid post-operative functional deficit [131, 25, 72].

A tract can be modelled as a 3D space curve  $\mathbf{r}(s)$ , which is parameterized by its arc length  $s$ . To reflect the information extracted from the diffusion data, the tangent at arc length  $s$  must be equal to the voxelwise directional information given by the vector field

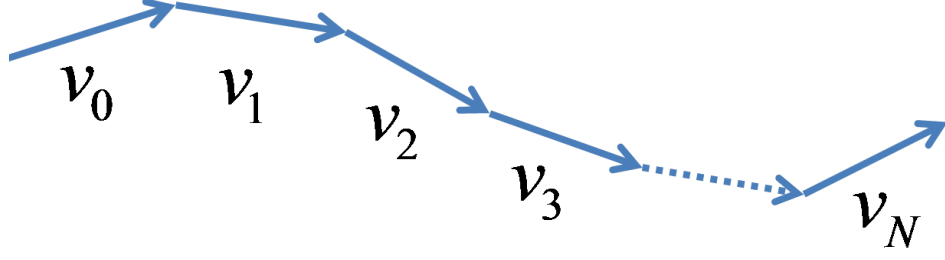


Figure 3.1: Simple diagram of a tract or streamline, formed from a train of vectors.

$\mathbf{v}$  which is derived from the models described in section 2.4 (for example the principal eigenvector of a diffusion tensor or the orientation of the stick component of the ball and stick model):

$$\frac{d\mathbf{r}(s)}{ds} = \mathbf{v}[\mathbf{r}(s)] \quad (3.1)$$

Equation 3.1 can be solved by integration:

$$\mathbf{r}(s) = \int_{s_0} \mathbf{v}[\mathbf{r}(s)] ds \quad (3.2)$$

In practice the integral in equation 3.2 is broken down into a discrete approximation. Starting at a seed point  $\mathbf{r}_0$  a step of size  $\Delta$  is taken in the direction  $\mathbf{v}(\mathbf{r}_0)$  to location  $\mathbf{r}_1$ , such that  $\mathbf{r}_1 = \mathbf{r}_0 + \mathbf{v}(\mathbf{r}_0)\Delta$ . This process is repeated until some termination criteria is reached:

$$\mathbf{r}_{i+1} = \mathbf{r}_i + \mathbf{v}(\mathbf{r}_i)\Delta \quad (3.3)$$

Thus the tract is formed as a train of vectors joined end to end as illustrated in Figure 3.1. At each step  $i$ , the vector  $v_i$  is drawn from the vector field  $\mathbf{v}$  which is derived from directional information extracted from a diffusion model such as those described in section 2.4.

The key difference between differing tractography algorithms is the way the vector  $v_i$  at each iteration  $i$  is drawn.

Tractography methods generally rely on two general assumptions about WM structure: (i) WM fascicles are smooth and present low curvature and (ii) WM fascicles interconnect regions of GM and therefore do not stop in WM. This is based on anatomical knowledge gained from histological examinations such as that shown in Figure 2.7. The use of these assumptions may be dependent on context, for example in neurosurgical planning, defining the shape of fascicles in the body of the WM does not necessarily require that streamlines end in GM, hence this assumption may be relaxed. These assumptions govern choices when designing tractography algorithms such as parameter choices, prior assumptions on curvature and termination or tract selection/rejection criteria.

**Seeding tractography:** streamlines are integrated from an initial point, referred to as a *seed point* and the choice of this seed point is determined by the requirements of the application. A seed point is often chosen by a voxel location, and the seed point may be defined in the centre of the voxel. Alternatively, random points within the voxel boundaries may be chosen. In many applications multiple adjacent voxels are defined as seeds in a *region of interest* (ROI). The voxels are normally defined by drawing ROIs onto a rendering of the FA image, or a T1 image and the ROI often corresponds with a particular WM or GM structure in the brain. If a ROI is defined on a T1 image, a subsequent transformation is then required to locate the seed points in the coordinate system of the DW-MRI images to perform tractography. In certain applications, such as those studying the whole brain as a network, the entire brain volume, or the entire white matter volume may be used as a ROI to seed tractography.

Currently, most tractography research and clinical application relies on manually defined seed regions, usually defined by an experienced researcher or clinical scientist who is familiar with both the relevant neuroanatomy and the technicalities of tractography. This remains the most effective way of localising seed regions and waypoints and no method of automatically placing seeds is currently well established. However, it must al-

ways be noted that this leaves room for bias in ROI placement which leads to subsequent effects in tractography results. Different researchers may have differing approaches to delineating anatomical features or anatomical features may be distorted in the image by noise, artefacts or pathological lesions such as tumours or regions of tissue degeneration. While judicious placement of ROIs by sufficiently experienced practitioners is normally adequate to ensure the veracity of results, potential biases must always be kept in mind when interpreting results.

**Termination criteria:** termination criteria differ depending on application context and algorithm specifics. The most basic termination criteria is based on a streamline reaching an area outside of the brain. This is normally implemented using a brain mask, which identifies all voxels which are considered to be either WM or GM and excludes other features such as CSF or parts of the skull. Further to this, tracts may be terminated upon entry into a region of interest (ROI) defined by either a region of voxels or a 3D structure defined by a mesh. Such termination criteria are common when finding connectivity between certain brain regions with ROIs defined manually or via automatic parcellation or segmentation. Other choices include terminating tracts when they enter an area of low FA, below a certain threshold, in DTI tractography. The rationale being that areas of low FA tend to be associated with high uncertainty in the principle diffusion direction therefore there exists a high potential for error in subsequent streamline steps. Some algorithms also terminate based upon an assumption of limited curvature, i.e. if the next streamline step is highly deviated from the previous one, then the streamline will be terminated at this point.

### **3.1.1 Deterministic tractography**

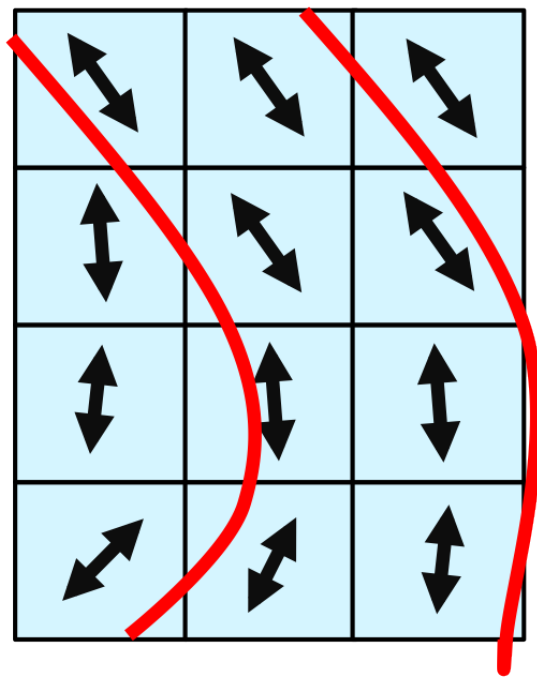
Early tractography approaches focussed on the diffusion tensor model described in section 2.4.1. These assumed that the fibre direction in a voxel could be described by the principal eigenvector of the diffusion tensor and used simple interpolation to derive the

fibre direction at an arbitrary location. FACT (Fiber Assignment by Continuous Tracking) [79] made use of nearest neighbour interpolation and later techniques made use of trilinear interpolation [28, 12]. Alternatively the information contained in the diffusion tensor can be used more comprehensively by deflecting the streamline direction at each step [73, 126], going beyond the use of the principle direction alone. These techniques described in the previous section are normally described as 'deterministic', as repeating the process from the same seed point reproduces the same result.

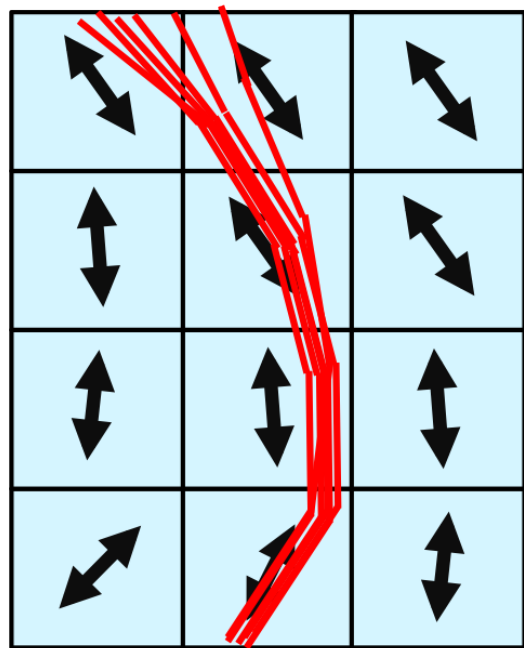
Deterministic tractography techniques are limited by the fact that DW-MRI is susceptible to noise, and hence uncertainty in the dominant fibre direction(s) in a voxel leads to a paradox in deterministic tractography, which only yields a single unique streamline per seed while uncertainty about the fibre direction(s) in each voxel would suggest a range of potential trajectories through each one. Errors may also arise due to modelling errors, as the microscopic anatomy of WM is more complex than a fibre reconstruction model which yields a single, or a limited number of, unique fibre directions per voxel. Deterministic methods are also susceptible to integration errors which accumulate along the streamline, due to the need to use a finite approximation to the continuous integral in equation 3.2.

### **3.1.2 Probabilistic tractography**

The deterministic tractography algorithms described in the previous section presume a unique fibre direction can be derived at each location and as such any seed point leads to a unique and well defined terminal location. Noise in the DW-MRI data creates a subsequent uncertainty on the dominant fibre direction in a voxel and therefore errors in the global trajectory of the streamline. Encountering a single voxel with errors in local fibre orientation estimates can lead to deterministic streamlines taking the wrong path and subsequent errors in global connectivity estimation. Therefore 'probabilistic' tractography techniques aim to characterise the uncertainty in the dominant fibre direction in each voxel, forming an 'uncertainty ODF' (uODF), then generate an ensemble of



(a) Deterministic tractography.



(b) Probabilistic tractography.

Figure 3.2: Deterministic vs. probabilistic tractography methods. Deterministic tractography integrates one streamline per unique seed location. Probabilistic tractography integrates many from each seed location, forming a distribution of potential connections.

tracts in a Monte-Carlo simulation, sampling a propagation direction  $v_i$  from the uODF corresponding to the current location of the tract at iteration  $i$ . The density of streamlines reaching various different image regions can then be interpreted as representing the probability of connection to the seed point, forming a distribution of potential connections from each seed point. The distribution is normally characterised by generating *visitation* maps which quantify the number of streamlines traversing each voxel in the brain volume. From any given seed point,  $N$  streamlines are generated and the index of connectivity  $I$  for voxel  $c$  is given by:

$$I(c) = \lim_{N \rightarrow \infty} I(c, N) \approx \frac{\mu(c, N)}{N} \quad (3.4)$$

where  $\mu(c, N)$  is the number of times voxel  $c$  is traversed by a streamline.

The number of streamlines seeded per voxel or per seed region differs depending upon the application. High numbers of 1000-5000 streamlines seeded per voxel are common for a single seed or for a small number of voxels defined as an ROI. Lower numbers per voxel may be used where large ROIs are used for seeding. In whole-brain network studies [26, 55, 49] the whole brain volume, or the whole WM volume may be used to seed streamlines, in which case lower numbers between 1 and 100 per voxel are more common to make the eventual streamline database more manageable and reduce processing times.

Different methods exist for estimating the uODF, including Markov chain Monte Carlo (MCMC) [14, 13] and bootstrapping [84]. Both deterministic and probabilistic techniques were extended to account for multiple fibre populations per voxel, using models as described in section 2.4 [85, 13, 117, 62].

The methods of estimating fibre orientation uncertainty can be separated into three main categories, *bootstrap* methods, *calibration-based* methods and *Bayesian* methods.

### **3.1.2.1 Bootstrap estimates of uncertainty**

Bootstrapping is a statistical method for deriving measures of accuracy on statistical samples. Certain implementations employ the traditional bootstrap method by acquiring multiple repeats of the diffusion weighted data [64], although a significant limitation of this is the amount of data required, producing lengthy scans and limiting the scope of practically viable acquisitions. This problem can be overcome by using the residual bootstrap, which simulates repeated sampling by resampling the residuals of a statistical sample, essentially artificially simulating repeated measurements [63, 128]. In these methods, a model, the DT, is fitted to the DW-MRI data, the residuals are then modified, and the diffusion tensor is refit numerous times, giving an artificial population of fibre estimates from a single dataset, which gives an estimate of the uncertainty in fibre direction caused by noise.

### **3.1.2.2 Calibration-based estimates of uncertainty.**

These methods rely on a calibration experiment to determine a relationship between some feature of the data reconstruction and the uODF, using synthetic data. Parker [86, 84, 85], Cook [30] and Lazar [71] construct a mapping from some rotationally invariant feature of the fibre orientation estimate using simulations. Parker [86] achieves this by creating a population of deflection angles between a known fibre direction and an estimate reconstructed by fitting the DT to noisy synthetic data. The deflection angles are then modelled with a Gaussian distribution for several levels of anisotropy, which then allows a linear model to be fit summarising the relationship between the FA and the Gaussian variance. This can then be used to infer the variance in each voxel during tractography.

### **3.1.2.3 Bayesian estimates of uncertainty**

In these methods, Bayesian inference is used to estimate a distribution of propagation directions, characterising the uncertainty without making simplifying assumptions about

the distribution. Behrens [14] and Hosey [54] make use of MCMC to sample the full posterior distribution of fibre orientations and other parameters of the diffusion model in each voxel as a pre-processing step, before selecting directions from these distributions as probabilistic streamlines are integrated. These methods require significant memory overhead due to the need to store the full range of fibre directions in every voxel as the distribution is not parametrized compactly using a model. Friman uses a Bayesian approach live while integrating streamlines [45], this has the advantage of having no computationally intensive pre-processing step with associated storage requirements, but requires certain simplifying constraints on the diffusion model and more calculation at each streamline step.

### **3.1.3 fODF and dODF tractography techniques**

Various methods have been proposed which sample propagation directions for tractography directly from the ODFs derived from HARDI reconstructions. Some approaches sample orientations from dODFs [21, 87, 35]. These are limited by the indirect relationship between the underlying fibre configuration and the dODF. The dODF exhibits properties related to the fibre configuration, such as maxima at the orientation of fibre bundles, but it also exhibits significant components of diffusion along other orientations. A better approach is to sample directly from the fODF, which directly models the fibre configuration in the voxel [119] and so is inherently more useful for tractography. By utilising the fODF directly a tractography algorithm can cover all WM fibre directions suggested by the data, instead of selecting only limited features of the fibre distribution such as mean direction. By ignoring the full range of possible trajectories through a voxel, we risk false negative connections in tractography.

It should be noted that while tractography methods which sample propagation directions directly from dODFs and fODFs are often referred to as 'probabilistic', they are not probabilistic in the same sense that the methods described in sections 3.1.2.1, 3.1.2.2 and 3.1.2.3 which deal with the uncertainty in fibre direction due to noise. dODF and fODF

probabilistic tractography methods do not select from a population of fibre orientations per voxel due to assumed uncertainty in the data, but due directly to a spread of real fibre directions suggested by the data.

### **3.1.4 Global tractography**

Global tractography algorithms attempt to find the global configuration of fibres which best explains the observed data, attempting to solve for all possible trajectories between two points [59] or over the entire brain volume simultaneously [43, 70, 91, 105, 106]. This is in contrast to the previously described streamline methods which integrate each streamline individually progressing from the seed point, which are collectively termed 'local' tractography methods. Global approaches simulate large ensembles of streamlines via various methods and use a diffusion signal model to synthesise the diffusion data which would correspond to each given candidate set of candidate streamlines. They then compare the synthesised DW-MRI signal with the measured DW-MRI signal and progressively minimise the difference via optimisation. Methods of computing the candidate sets vary from selecting subsets of a pre-defined colossal database of streamlines derived from local-tractography methods [105] to modelling fibre pathways as independent line segments which join to form connecting streamlines [43, 70, 91] or parametrised 3D space curves [59, 132]. Optimisation methods vary for each method and include differential evolution [105], simulated annealing [70], genetic optimisation [132] and MCMC [59]. This methodology has the advantage that local voxel-wise modelling complexities such as crossing fibres or curving or fanning fibres do not have to be considered as the voxel-wise model is effectively replaced by the set of candidate pathways traversing each voxel (see Figure 3.4).

#### **3.1.4.1 Advantages**

The global approaches potentially minimise errors caused by noisy voxels on a streamline path, which might cause a locally-propagated streamline to deviate, where global

## Local tractography

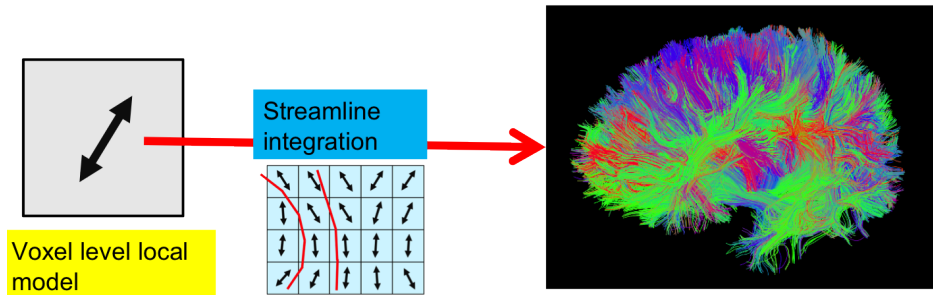


Figure 3.3: Schematic illustration of local tractography. Local tractography takes information from a local diffusion model, resolved voxelwise prior to tractography, then integrates deterministic or probabilistic streamlines from this information.

methods evaluate the validity of a particular streamline in a candidate set using its entire length. Global tractography supports the evidence of the streamlines traversing a particular voxel with further evidence from all the other voxel locations each streamline intersects, pooling information globally to resolve local fibre architecture. Hence when it comes to complexities in subvoxel architecture, global tractography can theoretically account for any and every conceivable configuration, including crossing, kissing, curving and fanning. In practice, however, accounting for any and every conceivable subvoxel architecture is essentially impossible, as it would require evaluating any and every possible ensemble of candidate streamlines.

### 3.1.4.2 Limitations

The major drawback of global methods is therefore the computational expense of finding the solution. As the problem becomes so high dimensional, with many millions of parameters governing the configuration of any ensemble of candidate streamlines, searching for the global minimum is practically impossible and so sub-optimal solutions must be accepted. Ad-hoc simplifications must be relied upon to find solutions in acceptable timescales. Given the computational expense, the efficacy of global tractography methods has been questioned when compared thoroughly with local methods [76].

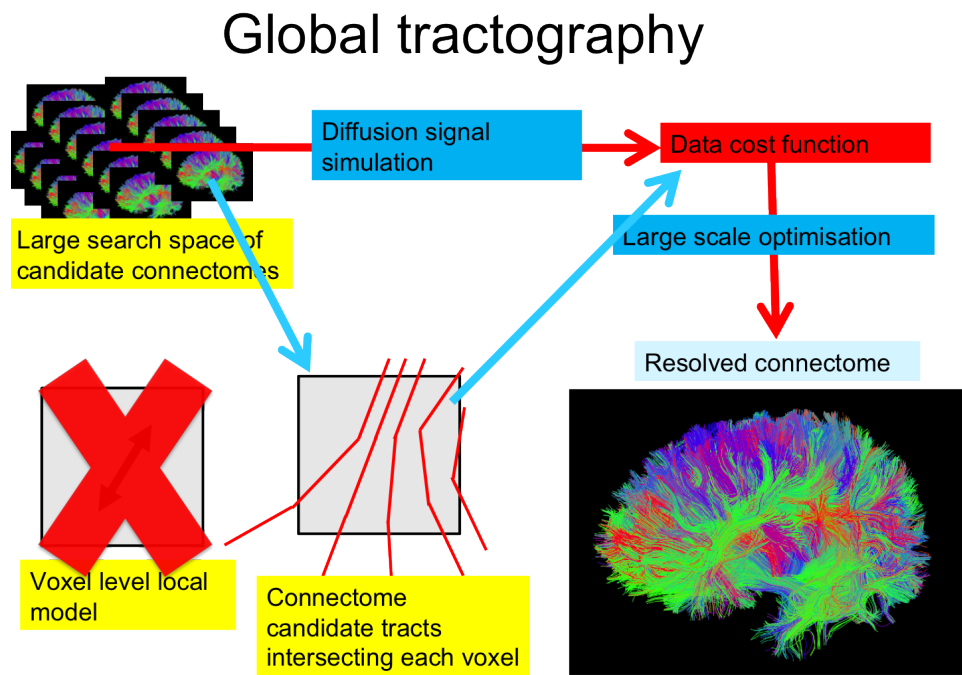


Figure 3.4: Schematic illustration of global tractography. Global tractography queries how well an entire candidate set of streamlines explains the data simultaneously, removing the need for a local model. The local model is replaced by the candidate streamlines traversing each voxel.

## 3.2 Summary and conclusions

This chapter has given an overview of a selection of the main tractography methods in recent research. As interest in tractography grew in DW-MRI research, tractography methods evolved from simple deterministic algorithms to stochastic implementations designed to account for uncertainty due to noise in DW-MRI data.

As hardware technology and acquisition design has improved, SNR in DW-MRI has become higher in standard acquisitions, with high SNRs of 20 routinely achieved and higher SNRs of 30 and above can be achieved given appropriate resources. HARDI acquisitions have become fairly routine in most research and therefore uncertainty due to noise has become less of a problem in tractography.

Recent DW-MRI modelling research has therefore been more concentrated on accurately modelling the underlying white matter architecture. Due to the limitation of the resolution of DW-MRI being of the scale of 1-3mm, complex fibre structure inside a voxel, such as the fanning and bending configurations shown in Figure 2.17 c) and d), can be such that a limited set of discrete directions (for example 2 or 3) is not adequate to accurately describe the underlying white matter architecture.

This leads to false negative and false positive connections in tractography. While it might be assumed that orientation dispersion in the underlying white matter structure would be reflected in the uODF as uncertainty in the dominant fibre direction, this is not the case in general. Sotiropoulos *et al* show in [108] that sub-voxel fibre orientation dispersion is not captured by the aforementioned uncertainty based methods, the shape of the uODF does not reflect the shape of the fODF in a voxel with fanning fibre structure and consistently focusses on the average fibre direction. The uODF only exhibits dispersion in the dominant, or average, fibre direction due to noise. Orientation dispersion in the uODF cannot be assumed to directly reflect orientation dispersion in the underlying fibre structure, although it may be influenced by it in an unpredictable way.

### 3.3 Motivations for this work

Global methods and local methods present two opposing ways of approaching the problem of examining WM structure and connectivity. Global tractography methods adopt a 'top down' approach, starting by attempting to examine all possible configurations simultaneously, avoiding the complex modelling decisions which must be made at the local, voxel-wise level. Local tractography methods adopt an opposing methodology, a 'ground up' approach, attempting to resolve fibre structure locally at the voxelwise level first, then using this information to build global connectivity estimates one streamline at a time. Both methodologies present corresponding drawbacks. Global tractography presents a theoretically appealing solution which is not, in practice, computationally tractable. If the global minimum of the optimisation problem could be found, it would provide the best solution, however, due to the scale of the problem, this is not practically possible. Local tractography presents a much more computationally approachable solution, but is hindered by the problem of DW-MRI signal models being unable to accurately describe WM fibre structure.

This motivates the use of models which more accurately describe sub-voxel fibre architecture in tractography, deriving propagation directions directly from an fODF modelling sub-voxel fibre dispersion, to account for all possible trajectories through an image volume. With the advent of new DW-MRI tissue models that accurately describe dispersing fibre architecture, it is timely to find ways of using these models in tractography. As shown by Sotiropoulos in [108], the most appropriate models for capturing complex sub-voxel architecture exhibiting orientation dispersion are those described in section 2.4.6. Chapter 4 describes a tractography algorithm based on an extension of the NODDI model [135, 115], a parametric model utilising the Bingham distribution to model sub-voxel fibre dispersion.

While improving the local, voxel-wise model has potential benefits for tractography, the global tractography paradigm of pooling data from multiple voxels to resolve am-

biguities in the locally derived information remains a powerful concept. A method for utilising extra information which can be gained from considering voxels aside from that in the immediate vicinity of the streamline front without inflating the problem to computationally intractable proportions can further improve tractography. In chapter 5 we propose a tractography algorithm combining parametric dispersion models with neighbourhood exploration, bridging the gap between global and local tractography.

# Chapter 4

## Utilising measures of dispersion in tractography

### 4.1 Introduction

This chapter introduces a novel tractography algorithm exploiting a parametric model of dispersion as described in section 2.4.6. The hypothesis is that by making use of parametric models capturing sub-voxel orientation dispersion we can address some of the flaws of traditional tractography techniques by using models which more accurately represent the underlying white matter architecture. Most currently available tractography algorithms only utilise a small number of discrete directions to represent the range of potential fibre orientations in any given voxel with only noise-based deviations from these directions accounted for in the model [14, 13, 86, 84]. Others utilise a more comprehensive fODF [56, 117], but the spherical distributions used to represent the fODF in each voxel do not accurately and robustly model sub-voxel fibre dispersion [108].

Areas of the brain such as the corona radiata exhibit significant fibre dispersion, which is observable in *ex vivo* dissections such as that shown in Figure 2.7. Parametric models of fibre dispersion [135, 65, 108] are able to model this dispersion more accurately and robustly than alternative models [108], therefore they are good candidates for

tractography algorithms.

Due to the more complex nature of the fibre dispersion models, some technical challenges are anticipated, and this work has focussed on finding solutions to these technical challenges. The tractography algorithm described in the following is based on the NODDI model described in section 2.4.7. We first outline the technical details of the tractography algorithm, which builds upon a technique proposed by Friman *et al* [46], which uses the DT as a DW-MRI model, to utilise the more advanced NODDI model. We then examine the behaviour of the tractography algorithm on a synthetic dispersing fibre structure, showing that utilising the NODDI model in tractography addresses the false negatives inherent in results from simpler tractography algorithms, which do not account for sub-voxel fibre dispersion. Further investigation is then carried out on *in vivo* data of a human subject to validate the advantages of utilising dispersion models in tractography on real data.

## 4.2 Methods

### 4.2.1 Tractography

#### 4.2.1.1 NODDI tractography

In the following, we adapt the approach used by Friman *et al* in [46]. This approach allows us to employ a fully probabilistic framework exploiting distributions based on fibre dispersion while applying suitable priors to enforce smoothness on streamlines derived from the DW-MRI data. Friman’s approach accommodates only the uncertainty in the principle diffusion direction induced by noise, image artefacts and partial volume effects; we instead incorporate underlying fibre dispersion directly in the ODF used to guide the tractography.

We may model a pathway as a train of vectors, as described in chapter 3,  $v_{1:n} = \{\hat{v}_1, \dots, \hat{v}_n\}$ . Paths can be built sequentially by drawing vectors  $\hat{v}_1$  to  $\hat{v}_n$  from the PDF

corresponding to the appropriate step  $p_i(\hat{v}_i|\hat{v}_{i-1},D)$  in sequential order and terminating upon some appropriate criteria like exiting a brain mask or a white matter mask.  $p_i(\hat{v}_i|\hat{v}_{i-1},D)$  is different for each step on the path and is dependent on the data at the relevant 3D location.

Hence the problem of building up the streamline  $v_{1:n} = \{\hat{v}_1, \dots, \hat{v}_n\}$  breaks down to an iterative process of sampling from the PDF  $p_i(\hat{v}_i|\hat{v}_{i-1},D)$  at each step  $i$ . The one exception is for the point  $i = 1$  for which  $\hat{v}_{i-1}$  is not known and  $\hat{v}_1$  is sampled from  $p_1(\hat{v}_1|D)$ .

To propagate the streamline through the image, starting from a seed, we choose a propagation direction  $v_i$  from a distribution formed from the product of the local ODF and a prior on the allowable deviation from the previous direction  $v_{i-1}$ :

$$P(\hat{v}_i|\hat{v}_{i-1},D) = \frac{P(\hat{v}_i|D)P(\hat{v}_i|\hat{v}_{i-1})}{P(\hat{v}_i)}, \quad (4.1)$$

This so far is similar to the approach given in [46]. In [46] the likelihood  $P(\hat{v}_i|D)$  is calculated by modelling a cylindrical DT with the assumption of a Gaussian distribution of potential directions due to noise and comparing this with the underlying data. This is aimed at accounting for uncertainty in fibre direction due to noise, in contrast to our method, in which the model used is based on the distribution of fibre directions estimated in each voxel by the NODDI technique. Due to the complexity of sampling from the posterior distribution, Friman chooses to discretise the spherical posterior by evaluating it on 2562 unit vectors derived from the vertices of a 4-fold tessellation of an icosahedron, which is the chosen approach we use in the following.

The model used to describe the probability of an fibre existing in a voxel with orientation  $\hat{v}_i$  given the DW-MRI data  $D$  is the Bingham model described in section 2.4.7. The Bingham model has a mean axis  $\mu$ , a primary fanning axis  $\mu_1$  and two concentration parameters describing the degree of dispersion along the two orthogonal fanning axes  $\kappa_1$  and  $\kappa_2$ . Therefore equation 4.1 can be rewritten:

$$P(\hat{v}_i|\hat{v}_{i-1}, \mu, \mu_1, \kappa_1, \kappa_2) = \frac{P(\hat{v}_i|\mu, \mu_1, \kappa_1, \kappa_2)P(\hat{v}_i|\hat{v}_{i-1})}{P(\hat{v}_i)}, \quad (4.2)$$

where  $P(\hat{v}_i|\mu, \mu_1, \kappa_1, \kappa_2)$  is the Bingham distribution described above.

$P(\hat{v}_i|\hat{v}_{i-1})$  defines the prior used to impose smoothness on the propagated streamlines.

For this we use a distribution given by:

$$P(\hat{v}_i|\hat{v}_{i-1}) = \begin{cases} (\hat{v}_i^T \hat{v}_{i-1})^\gamma, & \text{if } \hat{v}_i^T \hat{v}_{i-1} \geq 0. \\ 0, & \text{if } \hat{v}_i^T \hat{v}_{i-1} < 0. \end{cases} \quad (4.3)$$

Sampling from this joint distribution allows exploration of the potential path directions in dispersive fibre regions while regularizing the curvature of the path.  $\gamma$  defines the strength of the curvature prior. Low values accommodate large degrees of deviation per streamline step, exploring more of the dispersion in each voxel, however, this also produces highly irregular streamlines. Higher values promote smooth, slowly curving pathways which correspond to known tract geometries.

We find the most appropriate value for  $\gamma$  using simulated data exhibiting dispersing structure, which is described in the next section, which models a region of highly dispersive ODFs. Figure 4.1(a) shows that low values of  $\gamma$  such as 1, results in irregular streamlines. However, at a significantly higher value of  $\gamma = 50$  (Figure 4.1(f)), such a strong prior on curvature can limit the potential trajectories of the streamlines, limiting full exploitation of the dispersive ODFs. Satisfactory results can be achieved for a range of intermediate values. For this demonstration of the algorithm we choose  $\gamma = 24$  (Figure 4.1(d)).  $\gamma$  may reasonably be tuned within this range for other applications if necessary. Figure 4.2 shows the distribution of streamlines as they reach the top of the phantom at  $y = 6$ , which are binned into 4 separate bins per unit length on the  $x$ -axis, creating a total of 32 bins across the 8 units shown in Figure 4.4.  $\gamma$  is increased from 0 in intervals of 4.  $\gamma = 24$  is chosen as it gives the distribution which most closely replicates the distribution given by the phantom streamlines. The behaviour of the tractography algorithm

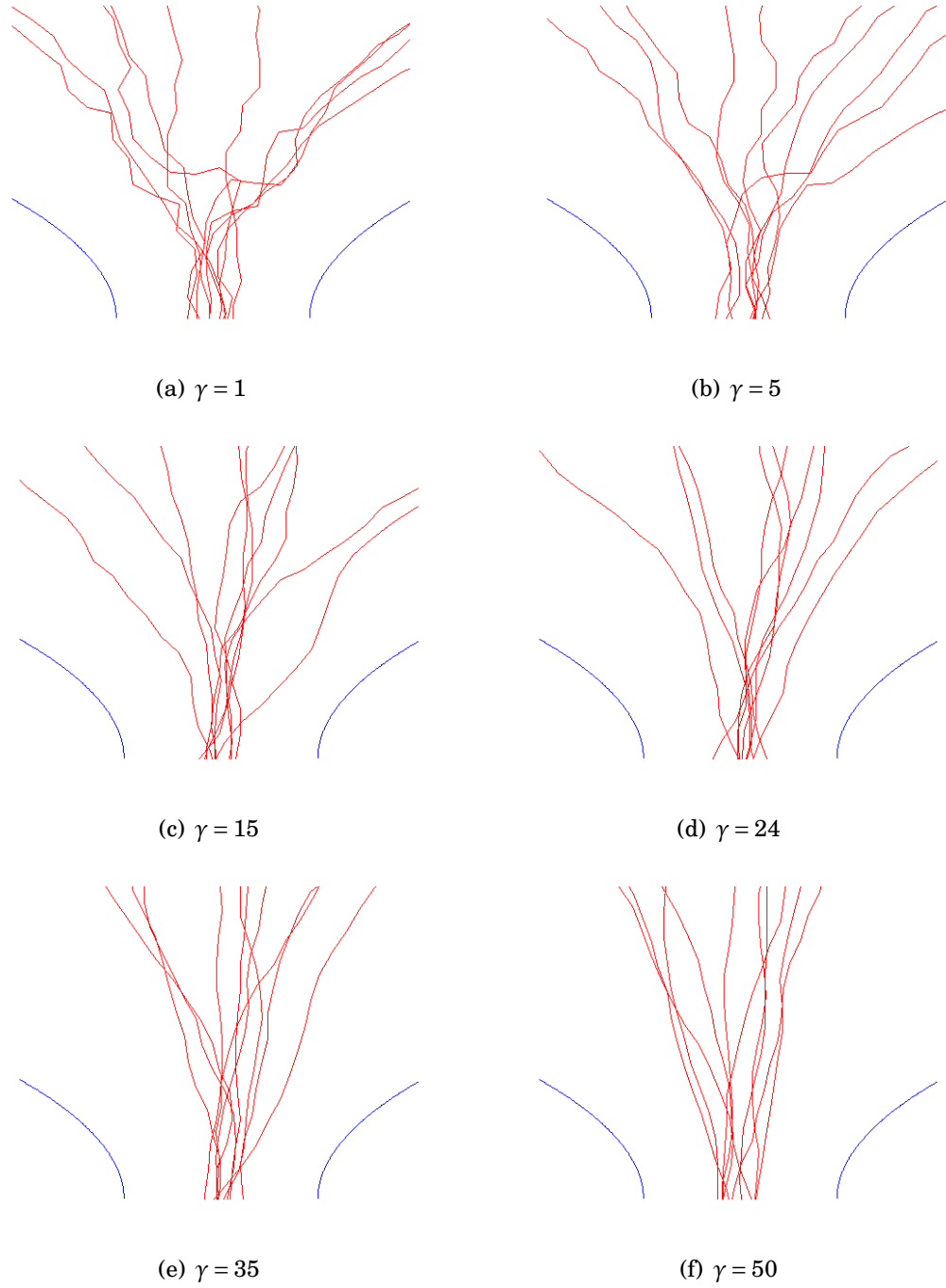
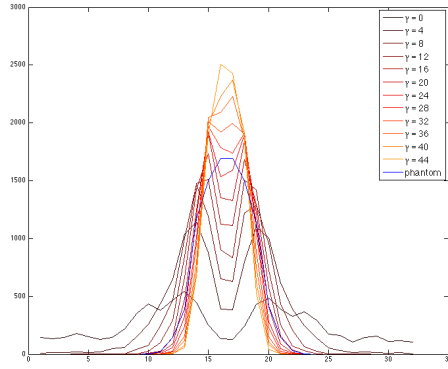
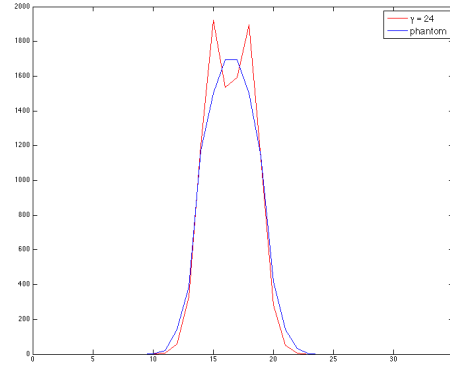


Figure 4.1: Tracking through a synthetic region of dispersion utilising different values of the constant  $\gamma$  in equation 3. In figure 4.1(a)  $\gamma = 1$ , in figure 4.1(d)  $\gamma = 24$  and in figure 4.1(f)  $\gamma = 50$ . The blue lines represent the extremities of the same phantom shown in figure 4.4.



(a) Binned streamlines for range of  $\gamma$  and for phantom streamlines.



(b) Binned streamlines for  $\gamma = 24$  and phantom streamlines.

Figure 4.2: Streamlines binned according to  $x$  location at top of phantom ( $y = 6$ ) in Figure 4.4 for varying values of  $\gamma$ , compared against streamlines extending from the same seed point in the phantom.  $\gamma = 24$  gives the closest profile to the distribution of streamlines from the phantom. There are 4 bins per unit length, making a total of 32 bins.

at extreme values of  $\gamma = 0$  and  $\gamma = 50$  in *in vivo* data is shown in Figure 4.9. It can be observed that at  $\gamma = 0$ , what is effectively a random walk through the field of Bingham distributions does not create strong connections to the cortex, as the streamlines spread out too much before they reach the cortex, producing a lot of false positives. At the other extreme of  $\gamma = 50$ , the curvature prior overwhelms the influence of the data, meaning the streamlines tend not to follow the data well, and they are focussed on a particular region of the cortex.

Sampling from the posterior distribution  $P(\hat{v}_i | \hat{v}_{i-1}, \mu, \mu_1, \kappa_1, \kappa_2)$  is not trivial. Rejection sampling can be used to sample from a standard Bingham distribution. However, to evaluate the full posterior, given by equation 4.2, a discrete approximation is required (Figure 4.3). Therefore, a set of vectors is defined which is very close to uniformly distributed over the sphere using the vertices of a 4 fold tessellation of an icosahedron. Equation 4.2 can then be evaluated for each of these vectors, and sampling from the resulting discrete distribution is then trivial.

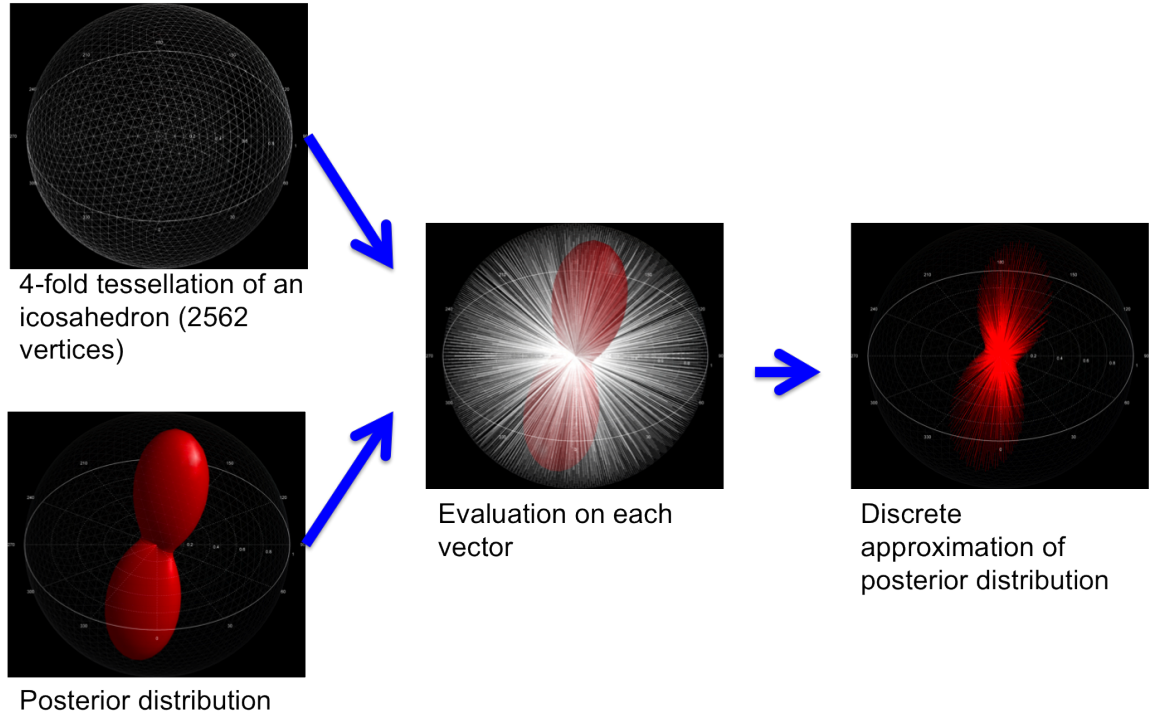


Figure 4.3: Schematic illustration of discretely approximating posterior distribution in equation 4.2

#### 4.2.1.2 PICo tractography

For comparison, PICo tractography is used as an example of a tractography algorithm which estimates deviation in fibre direction in each voxel due to noise only. The PICo tractography algorithm used is based on the algorithm given in [86] as implemented in the Camino software package [31]. The algorithm uses the DT as a model of diffusion and estimates the deviation of the principal direction in each voxel due to noise and fibre divergence via a 'calibration-based' approach, as described in section 3.1.2.2. The uncertainty of the principle direction is approximated based on the FA and the relative magnitudes of the second and third eigenvalues,  $\lambda_2$  and  $\lambda_3$  of the diffusion tensor.

#### 4.2.1.3 MRtrix tractography

For further comparison with an fODF-based tractography technique, the MRtrix software package is used to perform CSD and subsequent tractography. The MRtrix tractography technique utilises the fODFs derived from CSD which are described in section 2.4.5.4,

sampling a direction from the dODF given in each voxel located at the streamline front to propagate the streamline. The fODF in each voxel is an estimation of the WM fibre orientation profile and is presumed to be minimally impacted by noise.

#### 4.2.1.4 Methodological differences

The NODDI-based tractography algorithm described in section 4.2.1.1 differs from the two algorithms given in sections 4.2.1.2 and 4.2.1.3 in its use of a parametric model explicitly modelling dispersion. PICO tractography models the deviation of the fibre direction in each voxel based only on noise and features of the simple DT model. MRtrix tractography utilises the non-parametric fODF given by CSD, which has many degrees of freedom. In theory, the fODF given by CSD can model dispersion, however, the experiments carried out by Sotiropoulos *et al* in [108] show that the parametric models of dispersion used by NODDI are more accurate than CSD.

## 4.3 Experiments

### 4.3.1 Synthetic data

Synthetic data was used to determine the effect of utilising dispersion measures in tractography. A numerical simulation of a fibre configuration exhibiting subvoxel fibre dispersion was created. Figure 4.4 shows the structure of the phantom and the layout on the voxel grid. Each strand was then broken into line segments, each 1/10th the dimension of a voxel and the diffusion signal from each of these segments was simulated as a cylindrically symmetric DT with  $d_{\perp} = 3.5101 \times 10^{-4} \text{ mm}^2/\text{s}$  and  $d_{\parallel} = 2 \times 10^{-3} \text{ mm}^2/\text{s}$ , with the principal orientation of the DT dictated by the orientation of the line segment. The simulated DW-MRI signal generated from each line segment was then added to the signal for the voxel which bounded it, and the signal for each voxel normalised. Rician noise was added to each voxel to simulate an SNR of 20. The diffusion tensor was then fit to the simulated data using the Camino diffusion toolkit [31]. The Bingham NODDI

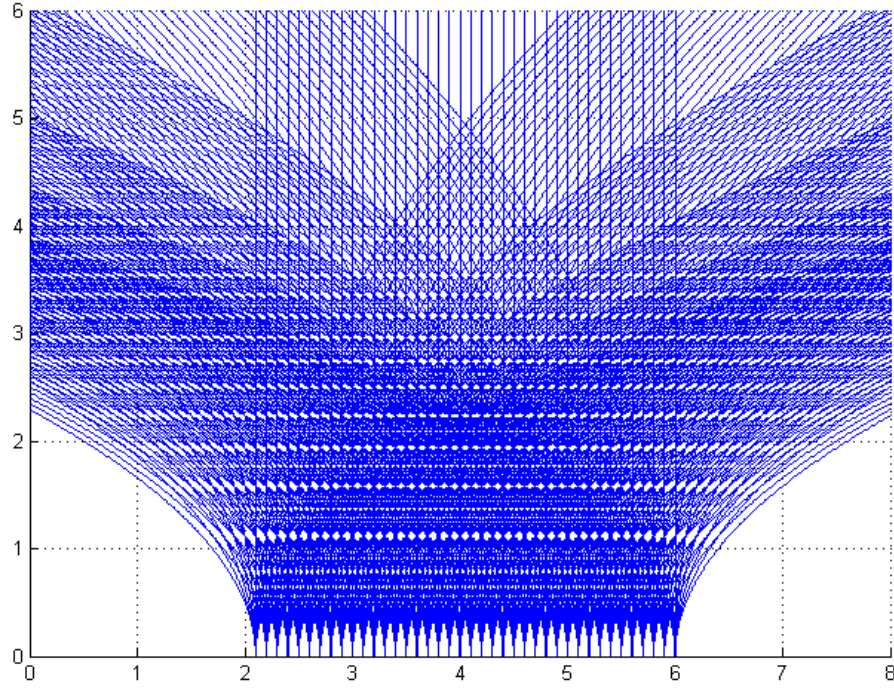


Figure 4.4: Structure of synthetic dispersing phantom. The blue lines show a subset of the strands forming the structure, for illustration the grid outlines the voxel boundaries.

model was also fit to the simulated data and used for tractography. The algorithm proposed in the previous methods section is compared against results from standard PICO tractography in Figure 4.7 tracking 200 streamlines from a seed point at the base of the phantom. The stepsize used for the tractography in the synthetic experiments is half the size of the voxel, which reflects the 1mm stepsize used in the 2mm voxels in the *in vivo* experiments described in the following.

A synthetic crossing fibre structure was created with the same method as described above. The algorithm proposed in the methods section was used to perform tractography from a single seed point at the base of the phantom using two different values of the curvature prior of  $\gamma = 2$  (Figure 4.6(a)) and  $\gamma = 24$  (Figure 4.6(b)).

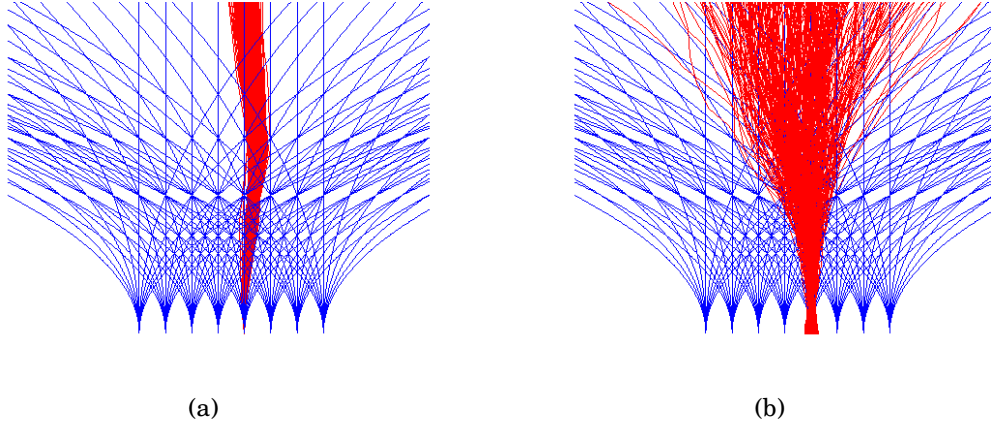


Figure 4.5: Tractography based on standard PICO tractography techniques (Figure 4.5(a)) and using the tracking algorithm described in the previous section (Figure 4.5(b)). The Blue lines represent a sparse selection of the underlying fibres of the phantom described in section 4.3.1. The red lines represent the tracking result.

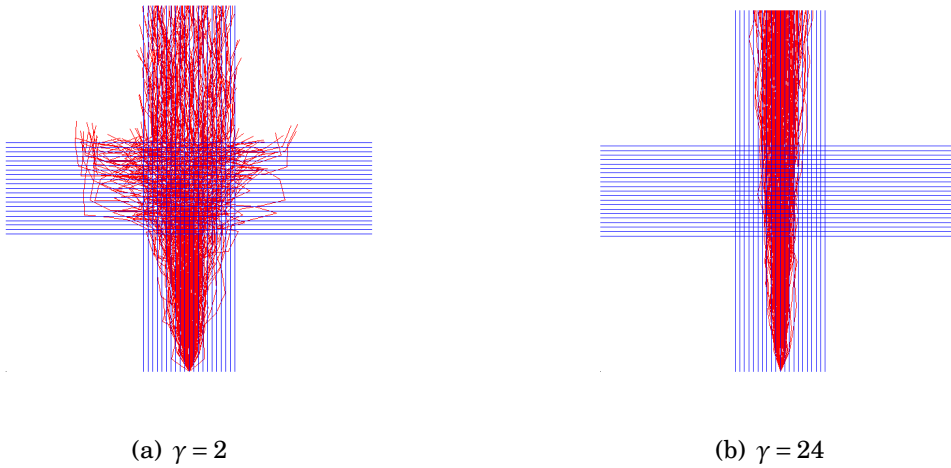


Figure 4.6: Results of tractography from a single seed point on a synthetic crossing fibre structure at high and low values of the curvature prior  $\gamma$ .

### 4.3.2 *In vivo* data

To examine the practical impact of utilising tractography based on measures of dispersion, we apply our tracking algorithm to *in vivo* data of a subject. DW-MR images of a healthy male were acquired on a clinical 3T Philips system with isotropic voxels of 2mm, TE=78ms, TR=12.5, with one 30 direction shell and one 60 direction shell with  $b$ -values of 711 s/mm<sup>2</sup> and 2855 s/mm<sup>2</sup> respectively. This dataset is the same as that used in [135]. The Camino software toolkit [31] was then used to fit the DT to the data and perform standard PICO tractography from a single voxel seed in the mid-sagittal corpus callosum. For further comparison, the data was processed using the CSD method, using the MRtrix software package [118], which was also used to perform tractography. The step-size for the proposed algorithm and DT-PICO tractography is 1mm, for MRtrix it is left as default at 0.2mm. As the CSD implementation in the MRtrix software package cannot utilise multishell data, the 60 direction shell was used for CSD as a higher  $b$ -value and many directions is optimal for CSD processing.

## 4.4 Results

The experiments on simulated data shown in Figure 4.7 show that tracking with traditional methods (Figure 4.5(a)) which ignore underlying fibre dispersion risks a large amount of false negative connections due to the limited exploration of the underlying fibre structure in regions exhibiting fibre dispersion. Figure 4.5(b) shows the proposed algorithm explores connectivity more thoroughly in dispersing regions in this simple synthetic phantom. Figure 4.6 demonstrates the value of utilising the curvature prior and justifies the chosen value of  $\gamma = 24$ . In Figure 4.6(a) we see that false negatives occur in the crossing region with an innappropriately low value of  $\gamma$  as the single Bingham distribution does not explicitly model the separate fibre populations, it instead models them as an oblate, disc-like PDF. Using a higher value of  $\gamma = 24$  the crossing region is successfully navigated in Figure 4.6(b), with no false positive connections. Figure 4.8 demonstrates

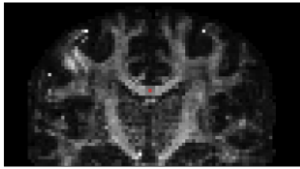
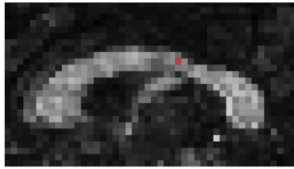
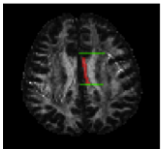
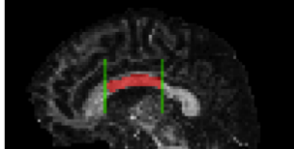
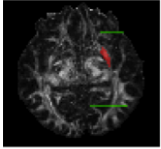
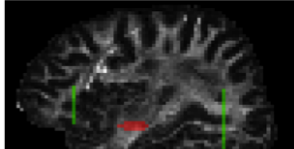
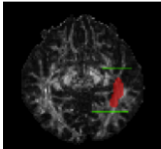
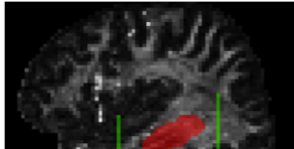
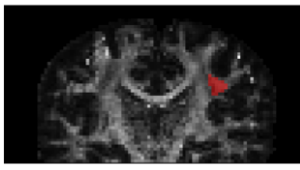
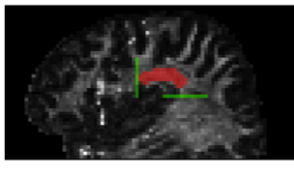
|  |   |   |
|--|---|---|
| Mid saggital CC<br>– single voxel              |    |    |
| Cingulum (Ci)                                  |    |    |
| Inferior fronto-occipital<br>fasciculus (IFOF) |   |   |
| Inferior longitudinal<br>fasciculus (ILF)      |  |  |
| Superior longitudinal<br>fasciculus (SLF)      |  |  |

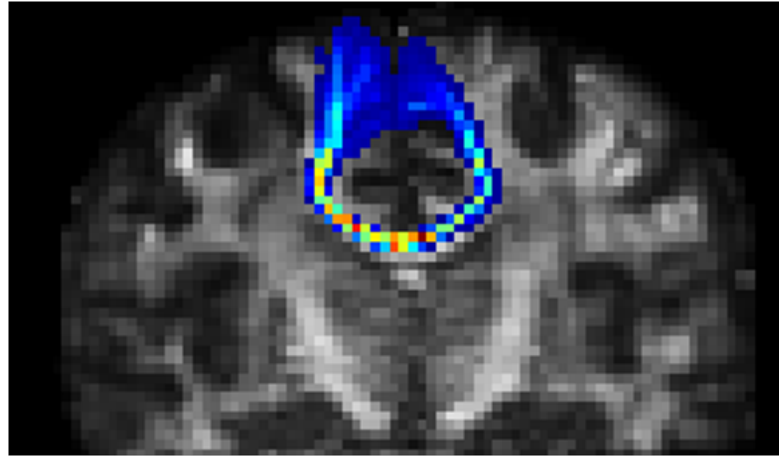
Figure 4.7: ROIs used for *in vivo* tractography overlaid on slices of FA map of subject. The red regions indicate the seed voxels while the green regions indicate the waypoints. Each streamline must intersect all distinct regions of waypoint voxels to be retained and contribute to the final connection probability map. It should be noted that the ROIs exist in multiple slices and not all ROI voxels are shown, the images here demonstrate the locality of the seed and waypoint regions.

the performance of both standard DT-PICo tractography (Figure 4.8(a)) and the algorithm presented in the previous section (Figure 4.8(b)) tracking from a seed voxel in the mid sagittal corpus callosum. For both tracking examples, 5000 streamlines in total are propagated from a single seed voxel. Streamlines are terminated upon entry into a mask defining the brain boundary. Figure 4.10 shows tractography from a seed in the corpus callosum, using the proposed algorithm (a) and using CSD (MRtrix) (b). The algorithms give similar results. Figure 4.10 c) and d) shows tractography between two ROIs in the internal capsule and a waypoint defining the the pre-central gyrus using the proposed algorithm and MRtrix respectively. It can be clearly seen that the proposed algorithm gives a more even spread of connectivity to the cortex from the internal capsule. Figure 4.11 shows tractography performed on 4 major white matter structures which are well delineated using most standard tractography algorithms, using ROI and waypoint placement guidance derived from [23] and [80]. All *in vivo* results are displayed as visitation maps with a threshold of 1% of maximum intensity.

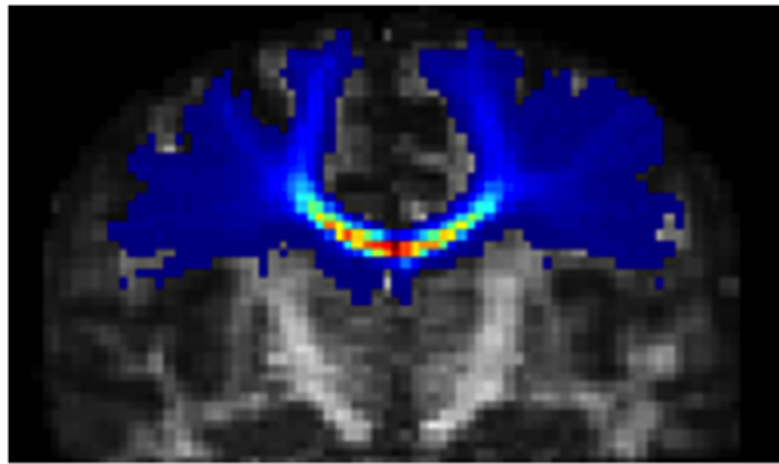
## 4.5 Discussion and conclusions

In this chapter, we presented a tractography algorithm exploiting the Bingham NODDI model of sub-voxel fibre dispersion. Results in synthetic phantoms prove that the algorithm is capable of following dispersing fibre structures more effectively than algorithms based on simpler DWI models which do not account for dispersion. We also prove that utilising an appropriate curvature prior, the algorithm is capable of navigating crossing fibre regions, despite separate fibre populations not being explicitly accounted for by the NODDI model.

Results from tractography seeded midsagittally in the corpus callosum show that the algorithm is able to address the false positives of traditional tractography techniques based on the diffusion tensor, successfully navigating a region of both crossing fibres and fibre dispersion which a DT based approach cannot. We find that the algorithm gives



(a) DT-PICo



(b) Proposed algorithm

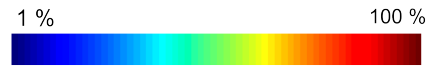
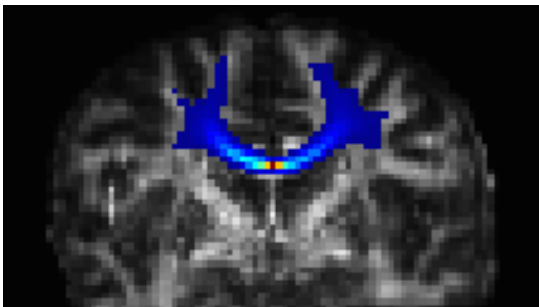
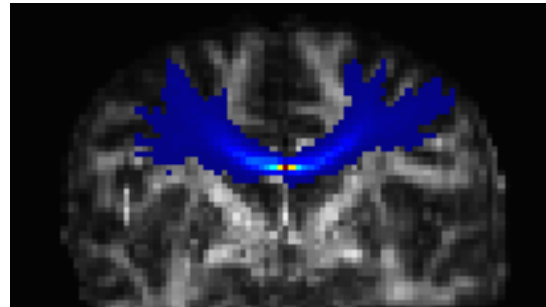


Figure 4.8: Visitation map of tractography based on standard DT-PICo tractography (Figure 4.8(a)) and using the tracking algorithm described in section 4.2.1.1 (Figure 4.8(b)) overlaid on FA map.



(a)  $\gamma = 0$



(b)  $\gamma = 50$

Figure 4.9: Tractography from single voxel seed in the middle of the corpus callosum at extreme values of the prior parameter  $\gamma = 0$  and  $\gamma = 50$  overlaid on coronal slice of FA map.

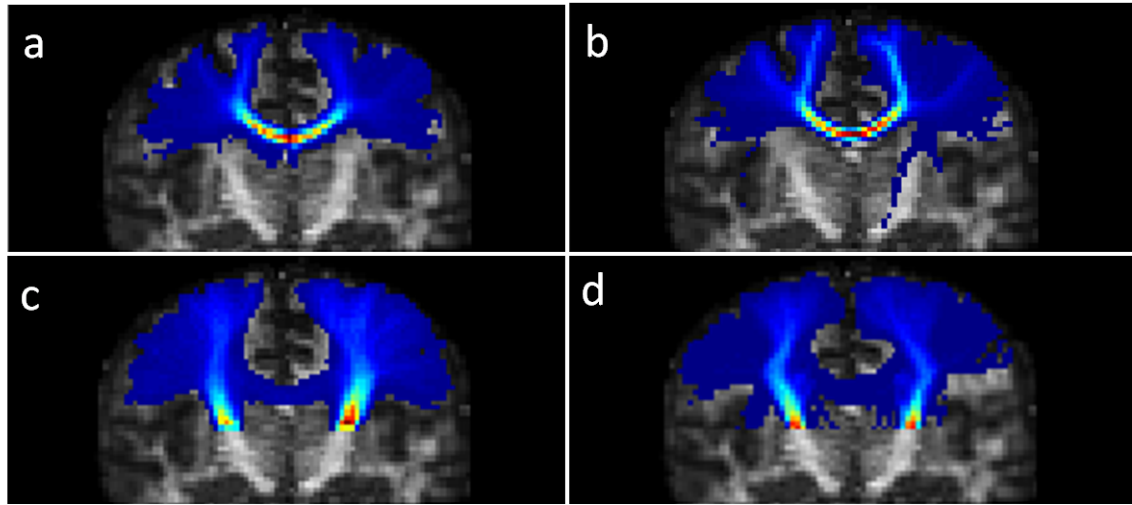


Figure 4.10: Tractography, using the algorithm described in section 4.2.1.1, from seeds in the corpus callosum (a) and the internal capsule (c). Results using constrained spherical deconvolution (MRtrix) [118] from the same seed points in the corpus callosum (b) and the internal capsule (d). Overlaid on coronal slice of FA map.

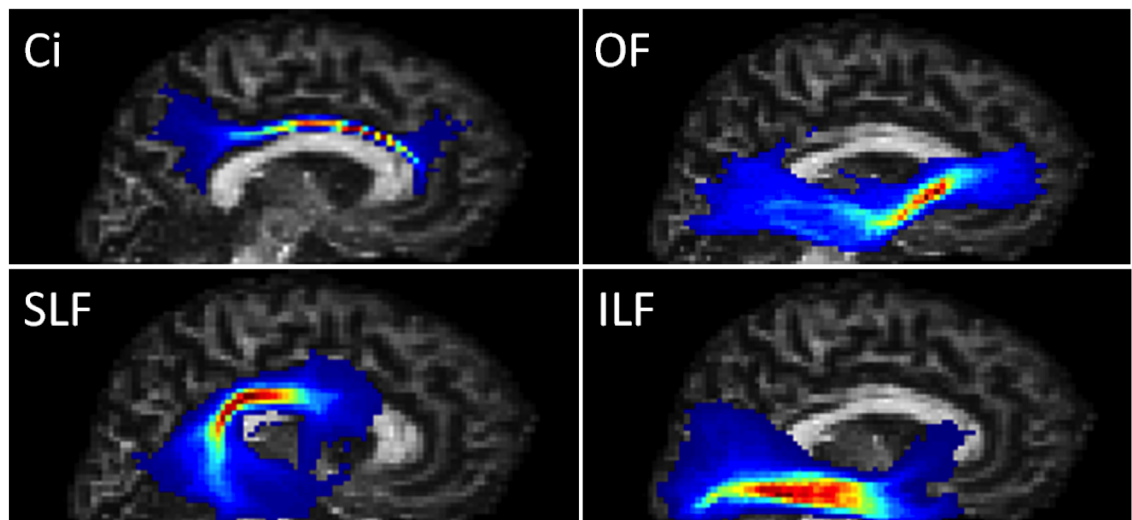


Figure 4.11: Tractography, using the algorithm described in section 4.2.1.1 on 4 major white matter structures, the cingulum (Ci), the occipito-frontal fasciculus (OF), the superior longitudinal fasciculus (SLF) and the inferior longitudinal fasciculus (ILF). Overlaid on sagittal slice of FA map.

comparable results to CSD, a state of the art fODF technique which models crossing fibres explicitly. This suggests that with the aid of a curvature prior, a tractography algorithm exploiting a single-direction parametric model of dispersion is able to navigate through multi-fibre regions as was shown in the synthetic experiments. When tracking from the internal capsule to the pre-central gyrus the proposed algorithm gives a more even spread of connections than MRtrix, which tends to favor the connections to the superior regions of the cortex, indicating that CSD may not be effectively capturing fibre dispersion in this region. While the algorithm can navigate multifibre regions, the extension of the NODDI model to explicitly model separate fibre populations and the dispersion therein with separate Bingham distributions should improve results, although fitting multiple Bingham distributions would be technically challenging and should be a focus of future work.

There is, however, one important point we must be aware of. If we consider the synthetic phantom shown in Figures 4.4 and 4.7, while the propagated streamlines correctly disperse as they travel upwards, if we were to seed in the top of the phantom, we would get unintended dispersion in the estimated streamlines, as the Bingham distributions are antipodally symmetric and do not distinguish the polarity of dispersion. We therefore risk false positives if we are tracking in the direction opposing dispersion.

The results presented here demonstrate the potential benefits of using parametric models of sub-voxel fibre dispersion in tractography. The simple algorithm presented here navigates crossing fibre regions successfully and exploits dispersion in areas where it is prominent. However, further development is required to address the issue of fanning polarity. When tracking in a direction opposing the direction of fibre dispersion, the algorithm presented here risks false positives caused by the ambiguity presented by antipodally symmetric parametric dispersion models. The following chapter presents a methodology to address this issue.

# Chapter 5

## Neighbourhood exploration

### 5.1 Introduction

In chapter 4 we presented a new tractography algorithm based on a parametric model of dispersion. We show that models of dispersion can be exploited in tractography to address false negatives of traditional tractography techniques which do not model the sub-voxel white matter architecture accurately. When using such models of dispersing white matter architecture it is important to address the fact that ambiguities arise in interpreting the ODF estimated in a voxel due to the inherent antipodal symmetry of diffusion weighted measurements and the lack of intra-voxel spatial specificity of the recovered distributions [58, 108, 103]. This leads to a number of potentially confounding configurations of white matter structure. Well known examples include kissing vs. crossing, curving vs. fanning and fanning polarity [58] which is illustrated in Figure 5.1. Such configurations existing at the sub-voxel scale require extra information to resolve the existing ambiguities of the ODF. If the ambiguities are not addressed, this will lead to false positives in tractography.

In order to address these ambiguities in the local voxel model of fibre orientation, we can make use of information from neighbouring voxels in the vicinity of the streamline front in addition to the local model. Savadjiev *et al.* [97, 98] demonstrate that information

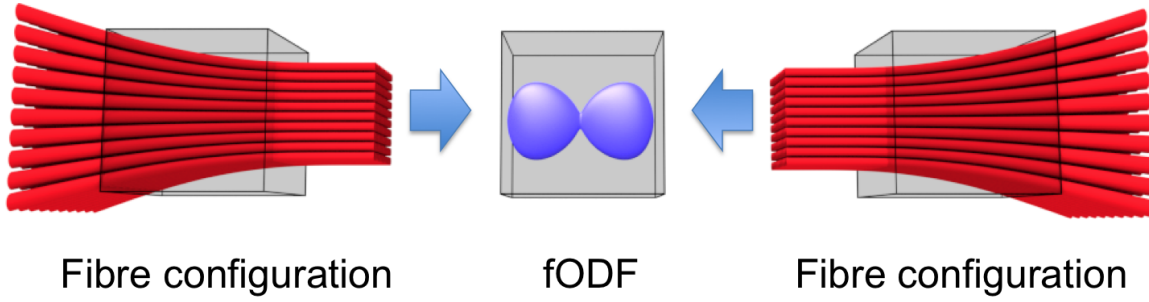


Figure 5.1: Illustration of fanning polarity ambiguity. The two opposing fibre configurations give the same fODF when estimated from diffusion data.

from a voxel's neighbourhood can be used to disambiguate sub-voxel fibre architectures such as curving and fanning. Using helical curves projected into the neighbourhood of a voxel, Savadjiev derives markers distinguishing and quantifying fanning and crossing fibres and fanning polarity within each voxel. The method parametrises the set of streamline selections enabling evaluation of those which are most consistent with forthcoming local structure. These methods demonstrate nicely the potential of leveraging voxel neighbourhood information for disambiguating fibre architecture at the subvoxel level. These methods however do not make use of a parameterised local model of dispersion and carry a computational expense due to the complexity of the helical model of streamlines, which would be costly to apply in a probabilistic tractography framework.

Using a local model capturing dispersion gives us a measure of fanning in each voxel, but does not distinguish the polarity of the fanning. We can recruit information from the local neighbourhood in order to mitigate false positives while tracking through a region of dispersing fibres. In Figure 5.2 a diverging and converging neighbourhood are illustrated. To the intuitive eye of a human, the distinction between these two configurations is obvious and leads naturally to an interpretation of the likely structure in the target voxel. We seek a method to enable a tractography algorithm to understand the difference between these two configurations.

This motivates the development of a neighbourhood exploration scheme to gather

information from the neighbourhood of the current tracking location to resolve the ambiguities of the voxel-based fODFs which can be effectively combined with a local model of fibre dispersion.

In the following we present a new tractography algorithm which utilises a 'neighbourhood exploration framework' to pool information drawn from both a local model of dispersion and the voxels in the neighbourhood of the streamline front to make informed decisions on the next streamline step such that we can account for sub-voxel fibre fanning and its associated polarity. As in the previous chapter, the tractography algorithm exploits the Bingham NODDI model as a local model of dispersion. The tractography method presented in this section will be referred to henceforth as 'neighbourhood informed tractography' (NIT) and as it is based on the NODDI model, it will be referred to as NODDI-NIT.

We first introduce the neighbourhood exploration framework, we then examine and validate the behaviour of the algorithm in synthetic reconstructions of canonical fibre configurations. The algorithm is then applied to *in vivo* data of 5 subjects, utilising seed regions which spawn streamlines passing through an area of significant dispersion, with a distinct polarity - the corona radiata, performing tractography in opposing directions through this region. We compare the *in vivo* results with other tractography methods, including CSD based tractography (MRtrix) [118] and DT-PICo tractography (Camino) [31] along with the method presented in the previous chapter. For clarity, the tractography algorithm described in the previous chapter will be referred to in the following as ND-track, short for 'neurite dispersion tracography' when contrasting it with NODDI-NIT.

## 5.2 Particle filters

Particle filters are a set of Monte Carlo posterior density estimation methods to estimate state variables given a set of observations using recursive Bayesian estimation used in non-linear, non-Gaussian dynamical systems. Particle filtering is alternatively known

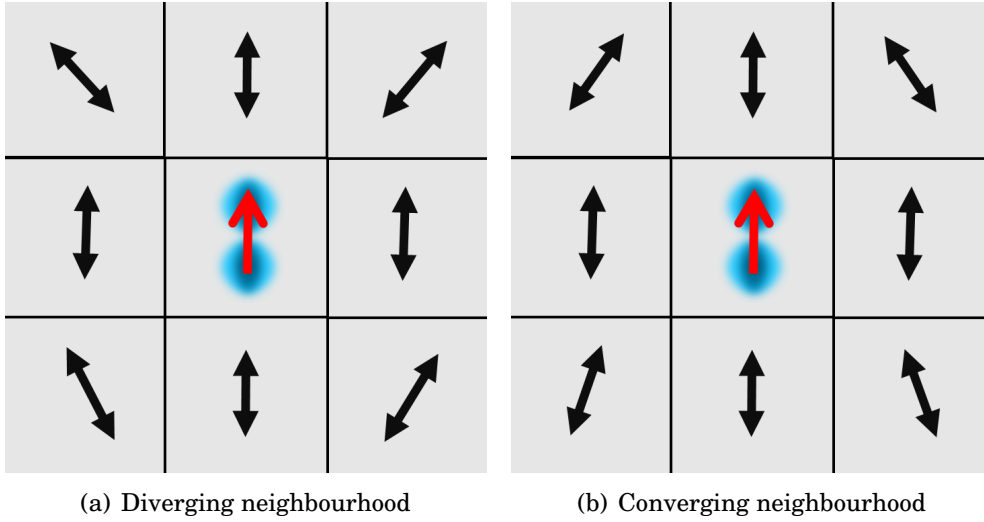


Figure 5.2: Illustration of diverging and converging neighbourhood structure.

as sequential Monte Carlo (SMC). The objective of the particle filter is to estimate the posterior density of the state variables  $\mathbf{x}$  given the values of the observation process  $\mathbf{y}$  with a known model which relates  $\mathbf{y}$  to  $\mathbf{x}$ .

Recursive Bayesian estimation techniques aim to estimate an unknown probability density function iteratively using incoming measurements and are commonly used in applications where the data is incoming in a real-time datastream. Via an iterative process of prediction and innovation, predictions are made at each timestep  $k$  on the state of the system  $x_k$  given the information known from the previous step  $k-1$  and the observations made in that step  $y_{k-1}$ . The particles are then weighted according to a likelihood model providing a discrete approximation to the posterior density  $p(x_k|y_0, y_1, \dots, y_k)$ , otherwise known and the 'filtering distribution'. In contrast to real-time applications, in tractography, where the data is static, the purpose of using a recursive Bayesian estimation technique is different. Although we have all the data at hand immediately, the high dimensional nature of the problem and the data means that considering *all* the data in one go is computationally intractable. A tractography algorithm attempts to find a 3 dimensional pathway through a 3 dimensional image volume between one point and another. Hence as it progresses from a seed point, *incoming* data is that which we encounter at each incremental point in the pathway corresponding to the appropriate coordinates at

the streamline front.

Particle filters have been used previously in tractography methods [19, 133, 88, 111, 99]. None so far have been based on a parametric model of sub-voxel fibre dispersion. These methods approximate the distribution of all tracts of a particular length emanating from a single seed over large distances. This can be problematic as it yields a very large state space which requires many particles and a high degree of degeneracy can arise among the particle set. This problem can be mitigated by resampling the particle set, but this may reject viable pathways in favour of others with only slightly higher weights. Stamm [111] utilises a multi-modal particle filtering method to address this problem, however, this still leaves a large state space and little focus is given to resolving details of structure more local to the tract front.

If a particle filter method can be used to examine candidate pathways over shorter ranges, it can be much more effective. We propose in the following section a tractography method which utilises a particle filter framework to gather information more locally, informing each step of a tract individually from information in the near neighbouring voxels as opposed to estimating a filtering distribution globally. The filtering distribution then becomes the set of potential streamlines projecting into the near neighbourhood of the current tracking location and those most consistent with oncoming structure are chosen for further propagation.

### **5.2.1 Neighbourhood exploration framework**

In this section we describe a technique that creates a neighbourhood-informed ODF (NI-ODF) from the local dispersion estimates by fusing the information drawn from the local model with information gathered from the neighbourhood structure of the dominant fibre orientation. We draw candidate directions from the local dispersion fODF and propagate these directions into the neighbourhood. By examining the coherence of each projected streamline with neighbourhood structure we can then weight each of these candidate directions according to the coherence of the respective projected streamline with the

neighbourhood structure. This process is illustrated in Figure 5.3 for various canonical neighbourhood structures. The streamlines which are misaligned with neighbourhood structure are downweighted (coloured in blue) and the streamlines which align with the neighbourhood structure have their weights increased (coloured in red). This shows that fanning polarity and curvature can be distinguished. In the case of a diverging neighbourhood structure, the streamlines propagated from the dispersed candidate directions drawn from the fODF in the relevant voxel find good alignment with the neighbourhood structure and are therefore evenly weighted. In contrast, in the presence of a convergent oncoming neighbourhood structure, the streamlines propagated from the peripheral candidate directions drawn from the local fODF misalign with neighbourhood structure and are downweighted. In the case of a curving structure, the candidate directions propagating against the curve are penalised and those following the curve are assigned higher weights.

This neighbourhood exploration scheme falls naturally into a particle filter framework. Through a process of prediction and update, the particle filter provides a discrete approximation of a posterior distribution  $p(x_k|y_{0:k})$  on a time-varying parameter  $x_k$  at timestep  $k$  given the observations  $y_{0:k}$  for timesteps  $0, 1, 2, \dots, k$  and the initial state distribution  $p(x_0)$ . At each timestep  $k$ ,  $N$  particles are propagated by sampling from an importance density  $\pi(x_k^{(i)}|x_{0:k-1}^{(i)}, y_{0:k})$ , then assigned importance weights  $w_k^{*(i)}$  which depend on a likelihood model  $p(y_k|x_k^{(i)})$ . Subsequently the discrete approximation to the posterior distribution  $p(x_k|y_{0:k})$ , denoted by  $\tilde{w}_k^{(i)}$ , is computed by normalising  $w_k^{*(i)}$ . This operation of a particle filter is summarised in Algorithm 1. Further details on particle filtering can be found in [39].

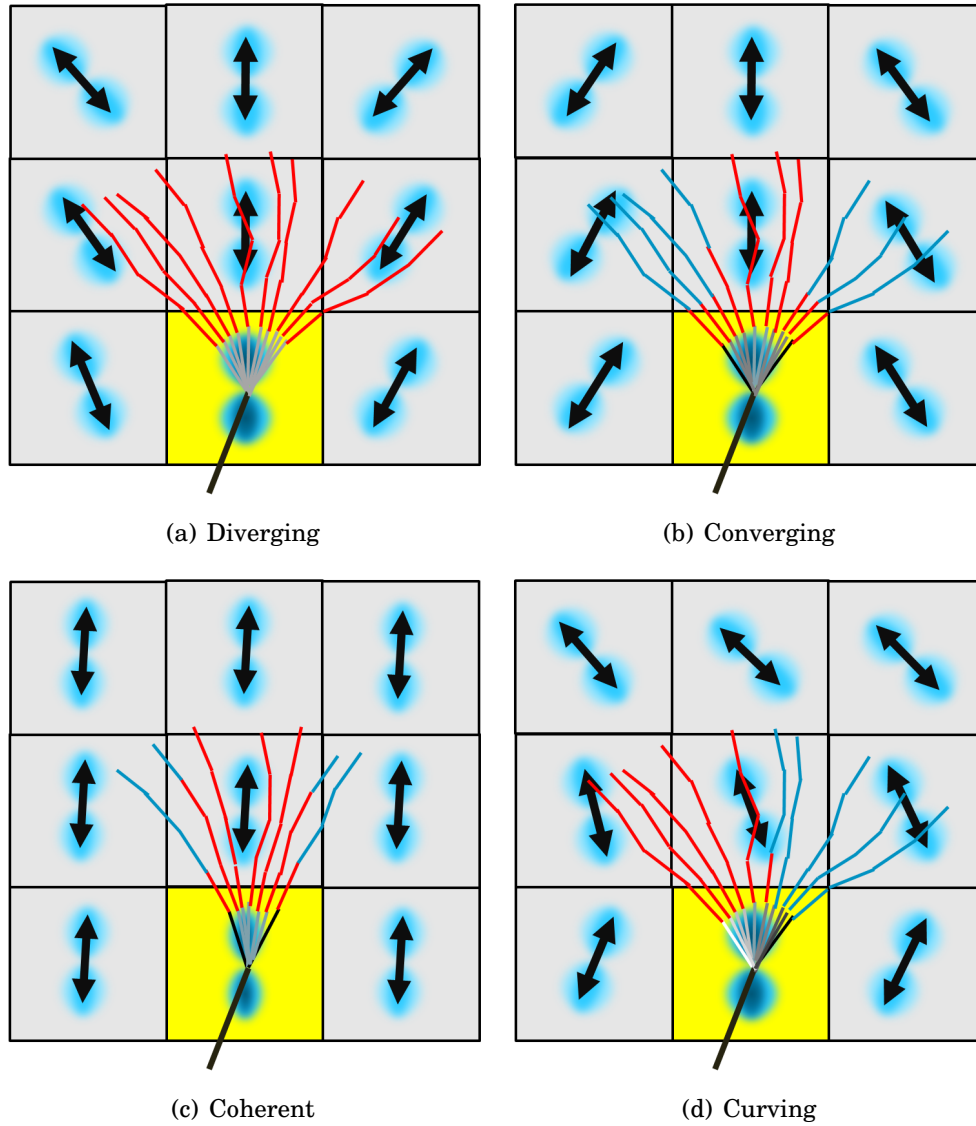


Figure 5.3: Illustration of neighbourhood exploration in the case of of diverging (a), converging (b), coherent (c) and curving (d) neighbourhood structure in the tracking direction. Red streamlines are highly weighted, blue are low weighted.

```

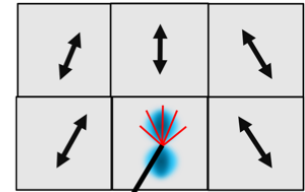
State initialization, sample  $x_0$  from  $p(x_0)$ ;
Initialise importance weights
for  $i = 1, \dots, N$ , do
     $w_0^{*(i)} = \frac{1}{N}$ 
end
for times  $k = 1, 2, \dots, K$  do
    for  $i = 1, \dots, N$ , do
        sample  $x_k^{(i)}$  from  $\pi(x_k | x_{0:k-1}^{(i)}, y_{0:k})$ 
    end
    calculate weight up to normalisation factor:
    for  $i = 1, \dots, N$ , do
         $w_k^{*(i)} = w_{k-1}^{*(i)} p(y_k | x_k^{(i)})$ 
    end
    normalise the importance weights:
    for  $i = 1, \dots, N$ , do
         $\tilde{w}_k^{(i)} = \frac{w_k^{*(i)}}{\sum_{j=1}^N w_k^{*(j)}}$ 
    end
end

```

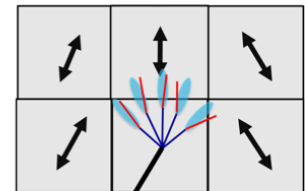
**Algorithm 1:** Sequential importance sampling

In this implementation, the importance density  $\pi(x_k^{(i)} | x_{0:k-1}^{(i)}, y_{0:k})$  is chosen as a Watson distribution and the initial state distribution  $p(x_0)$  is the Bingham distribution (described in Section 2.4.6) from the current voxel. Drawing the initial state distribution  $p(x_0)$  from the local Bingham distribution gives orientations, suggested by the local voxel model of dispersion, which govern the initial trajectories of a pool of candidate paths into the neighbourhood. The Watson importance density then ensures that paths of limited curvature propagate into the neighbourhood as the probability distribution is maximal at the mean direction, which is based on the direction of the particle in the previous step.

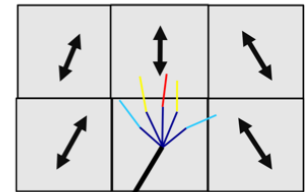
**Step 1:** candidate direction set from local Bingham distribution in the voxel located at the streamline face



**Step 2:** sample from a Watson distribution with a mean equal to the direction of the previous step for each candidate direction to propagate the candidate set into the neighbourhood



**Step 3:** weight the propagated candidate directions according to their alignment with the structure in neighbouring voxels



Repeat steps 2 and 3 K times

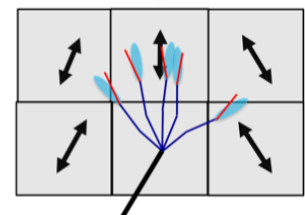


Figure 5.4: Illustration of the algorithm outlined in pseudocode above in algorithm 1.

The concentration of the Watson importance density therefore defines the curvature of the projected candidate streamlines. As it is known that WM tracts in the brain are smooth and present low curvature, this concentration is chosen to be high. A cloud of  $N$  particles defines a set of  $N$  streamlines defined by a string of vectors of fixed length connected end to end. At each timestep  $k$  each streamline is propagated one step from its previous location  $u_{k-1}^{(i)}$  with a direction vector  $v_k^{(i)}$  sampled from the importance density by a step length  $d$  such that  $u_k^{(i)} = u_{k-1}^{(i)} + dv_k^{(i)}$ . The state of a particle at timestep  $k$   $x_k^{(i)}$  is defined by its location  $u_k^{(i)}$  and direction vector  $v_k^{(i)}$ . At each step the particle weights  $w_k^{*(i)} = w_{k-1}^{*(i)} p(y_k | x_k^{(i)})$  are calculated to reflect their alignment with neighbourhood structure and the process is repeated for  $K$  steps. The likelihood  $p(y_k | x_k^{(i)}) = (v_k \cdot D(u_k))^\gamma$  where  $D(u_k)$  is the interpolated direction of the vector field  $D$ , defined by the mean directions of the Bingham distributions in each voxel, at the point location  $u_k$ . The stages of the particle filter scheme from streamline propagation to the selection of tract propagation direction is illustrated in Figure 5.5.

The neighbourhood exploration method can be seen in action in Figure 5.7. Canonical fibre configurations were simulated to exhibit the same structures given in the conceptual illustrations in Figure 5.3. Figure 5.7 shows the particles as they are upon the final iteration  $K$  of the particle filter, with the weights denoted by colour. The simulations in Figure 5.7 reflect the behaviour illustrated conceptually in Figure 5.3, showing that the neighbourhood exploration scheme behaves in practice as expected from the original concept. The most striking result is the differentiation of structures with opposing fanning polarity. From the perspective of a single voxel, these configurations look identical, as they give identical voxelwise fODFs. However as can be seen in Figures 5.7 a) and b), the neighbourhood-informed probability distribution readily distinguishes these configurations. In the divergent case the particles are evenly weighted while in the convergent case, the highly weighted particles are concentrated in the middle of the distribution, meaning that the peripheral directions which clash with the global structure of the simulated structure, will not be selected in the converging case.

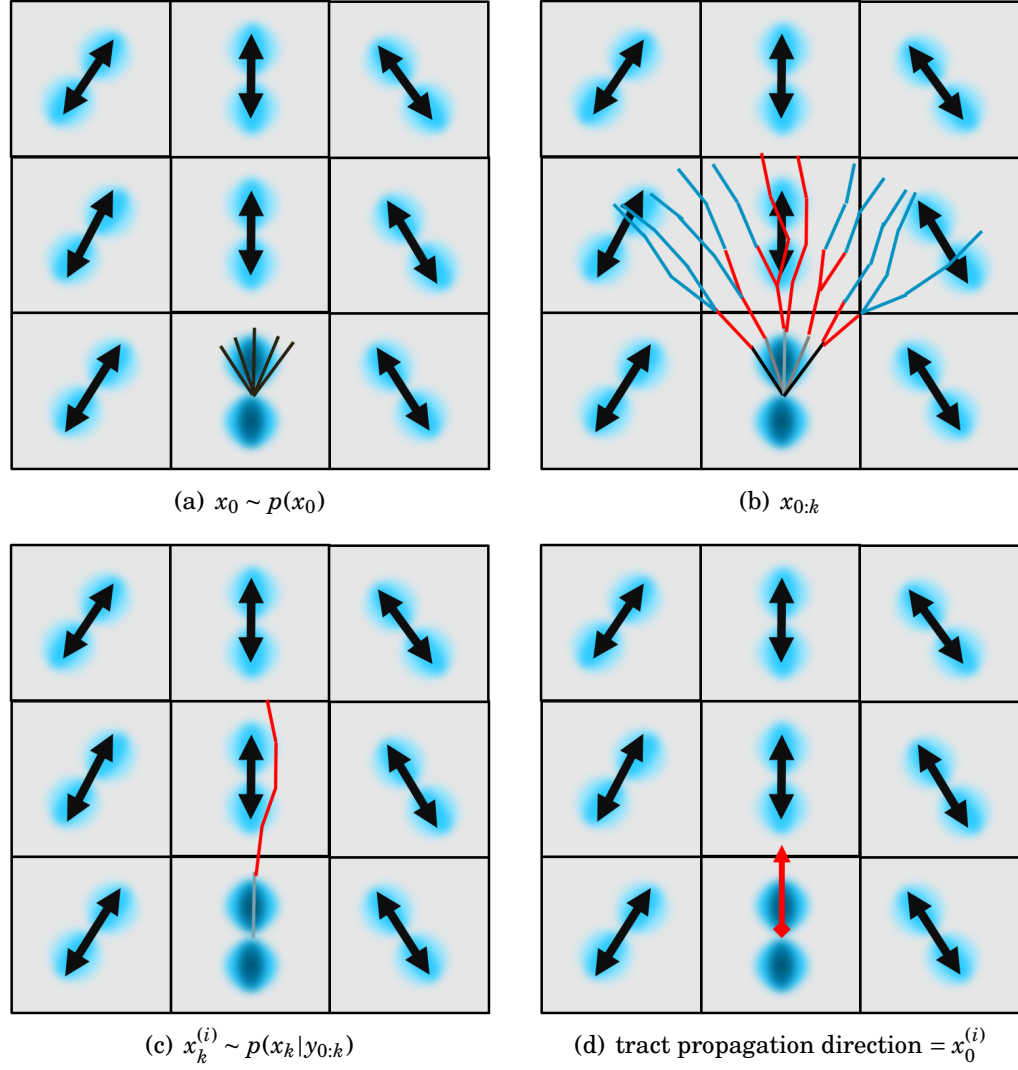


Figure 5.5: Illustration of the stages of neighbourhood exploration: initialisation from the local Bingham distribution (a), particle update and weighting (b), particle selection (c) and tract propagation direction selection (d).

### 5.2.1.1 Parameter choices

The parameters of the algorithm must be chosen carefully to ensure expected operation.  $\gamma$  influences the weight with which the transient streamlines are penalised for misaligning with neighbourhood structure. If this is chosen as zero, there is no penalty and any transient streamline can be randomly selected with equal weight, hence the neighbourhood exploration technique has no influence on the propagation of the overall streamline, it will be entirely governed by the Bingham distributions and will not aid in resolving fanning polarity. If  $\gamma$  is chosen too high, the streamlines will be too heavily penalised for even slight misalignment with neighbourhood structure. Given that the neighbourhood structure is discretised, this would not be sensible, therefore  $\gamma = 2$  is chosen.

The concentration of the Watson distribution used as the importance density governs the regularity of the transient streamlines which are propagated into the neighbourhood to gather information. If this is zero, the streamlines will be propagated in a random walk, taking any direction. This is not representative of the known regular structure of white matter tracts. The Watson concentration should be a high value such as 30 to propagate smooth transient streamlines into the neighbourhood.

$K$  and the transient streamline stepsize  $d$  together determine the distance into the neighbourhood which is probed by the neighbourhood exploration, such that the distance probed is roughly equal to  $K \times d$ . Figure 5.6 demonstrates examples of bad choices for these parameters. In Figure 5.6(a),  $K$  and  $d$  have been badly chosen such that the neighbourhood has not been effectively probed, as the transient streamlines have not penetrated beyond the voxel at the streamline face, so no real information has been gathered about the neighbourhood. In Figure 5.6(b), the algorithm has probed too far into the neighbourhood, and hence the choice of the direction for the next streamline step will be influenced by information gathered in structures clearly distinct from the one at the streamline face. Ideally, the neighbourhood exploration should probe more than one voxel, but less than 3 voxels into the neighbourhood.

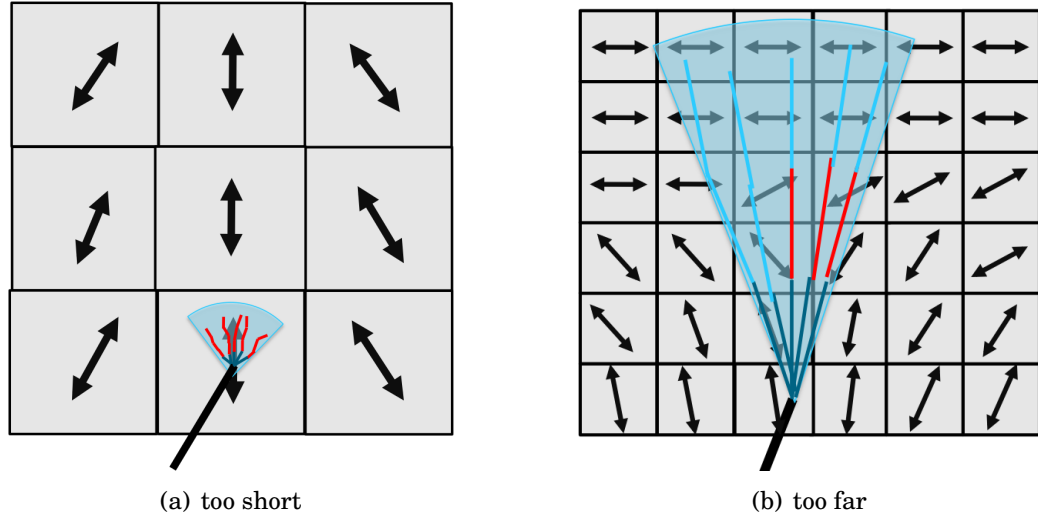


Figure 5.6: Illustration of two extremes of parameter choices which are non-ideal for the neighbourhood exploration framework. In Figure 5.6(a) the neighbourhood exploration doesn't go far enough, it remains within the local voxel and does not gather sufficient information about neighbourhood structure. In Figure 5.6(b) the neighbourhood exploration goes too far and gathers information from structures which are not related to the local voxel structure we are trying to navigate.

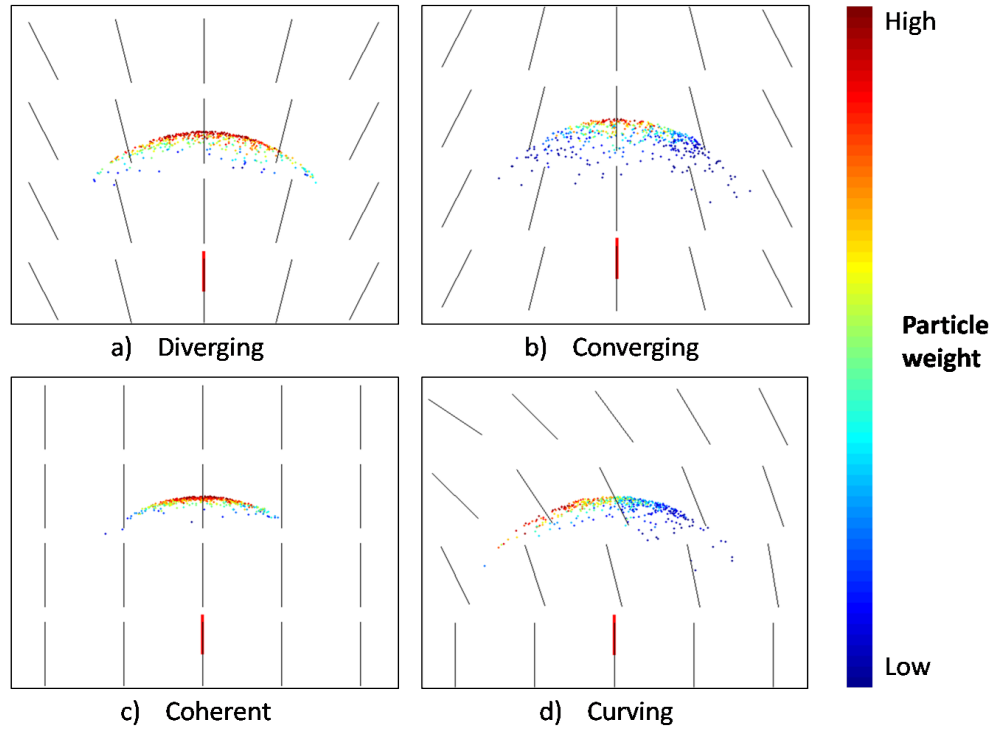


Figure 5.7: Demonstration of particle filter behaviour in regions of diverging (a), converging (b), coherent (c) and curving (d) neighbourhood structure in the tracking direction. Colour denotes particle weight, blue is low through to red, which is high, yellow is intermediate.

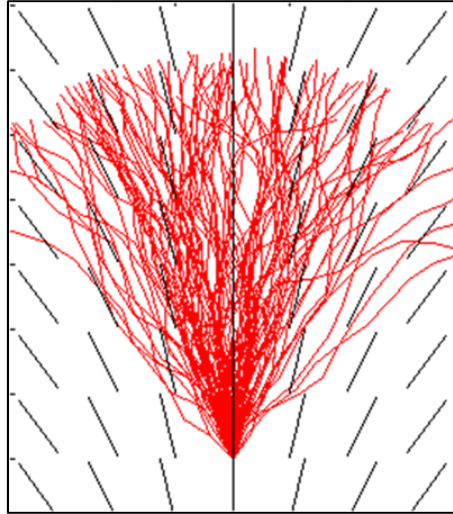
## 5.3 Experiments and results

### 5.3.1 Evaluation on synthetic dataset

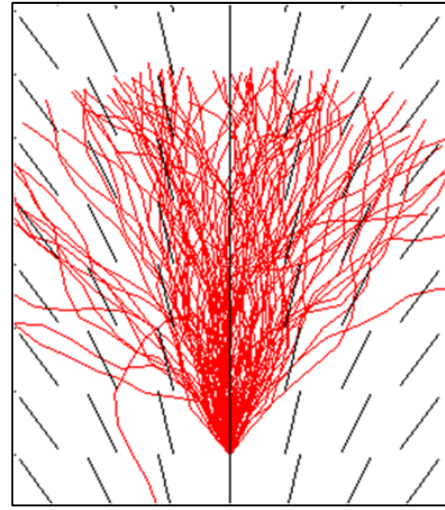
Figure 5.8 shows a demonstration of the NODDI-NIT algorithm over 100 repetitions in diverging and converging local structure. The data was simulated to give gross structural characteristics and sub-voxel dispersion similar to that observed in real data, as can be observed in regions of the corona radiata such as those shown in Figure 5.10. NODDI-NIT tractography was also performed from a single seed point in the synthetic crossing phantom described in the previous chapter in section 4.3.1.

### 5.3.2 *In vivo* data

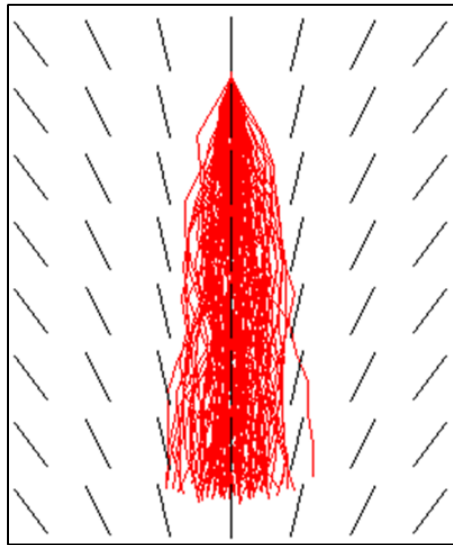
The *in vivo* data was acquired from 5 healthy subjects: 3 males and 2 females, between the ages of 23 and 35 years old scanned with informed consent and the approval of the research ethics committee. The data was acquired on a clinical Philips Achieva system with  $|\mathbf{G}|_{max} = 65mT/m$ . Two HARDI shells were acquired using a PGSE DW-MRI sequence with axial echo-planar imaging (EPI) readout with b-values of 711 and 2855. The echo time  $TE=78$  ms and repetition time  $TR=12.5$  ms, these are the same for all measurements. Voxels were isotropic with size  $2x2x2mm^3$ . The signal to noise ratio (SNR) is approximately 20. Total scanning time for the DW-MRI sequence is roughly 25 minutes. The data was processed with the NODDI-toolbox [1], modified to fit Bingham parameters. The data was also processed with the DT, using the Camino software package [31], which was also used to perform PICO tractography (referred to as DT-PICO). The data was also processed with CSD using the MRtrix software package [118], which was also used to perform tractography. The parameters of the NODDI-NIT algorithm were as follows: stepsize=1mm (or 0.5 voxels), Watson concentration 30, transient streamline stepsize ( $d$ ) =  $0.5mm$ ,  $K = 6$ ,  $\gamma = 2$ ,  $N = 50$ . For DT-PICO and MRtrix tractography all parameters were left as default. In each experiment 1000 tracts were used per seed region voxel for every algorithm.



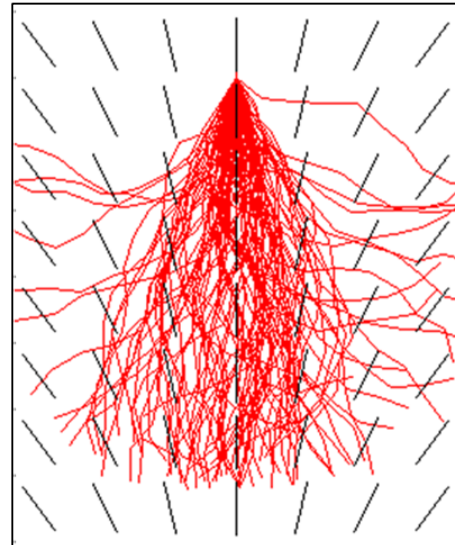
**(a) diverging with particle filter**



**(b) diverging without particle filter**



**(c) converging with particle filter**



**(d) converging without particle filter**

Figure 5.8: 100 repetitions of the tracking algorithm in regions of diverging (a), (b) and converging (c) and (d) neighbourhood structure in the tracking direction. In (a) and (c), particle filter neighbourhood exploration is used, while in (b) and (d) only a curvature prior is used as in chapter 4.

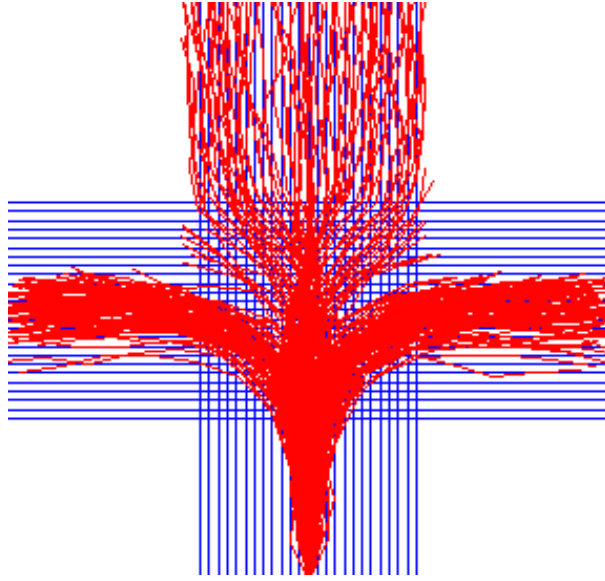


Figure 5.9: Tracking from a single seed on a synthetic crossing fibre structure. The algorithm fails to successfully navigate the crossing region due to the dependence of the neighbourhood exploration framework on the means of the Bingham distributions in each voxel.

### 5.3.3 *In vivo* experiments

To demonstrate the advantages of combining dispersion and neighbourhood exploration, tracking was performed on projection fibres passing through the region of the internal capsule and corona radiata (see Figure 2.7), where significant anterior-posterior fanning is present. Several white matter fascicles, collectively known as the projection fibres, extend from the cerebral peduncle and pass through the internal capsule then spread significantly to form the corona radiata. The fanning structure in this region has a distinct polarity, which can be easily seen in Figure 5.10, which is inferior-superior (i.e. the fibres spread as they travel upwards).

Figure 5.12 shows the results of tractography performed from ROIs manually defined in the cerebral peduncle and the superior portion of the pre-central gyrus, using NODDI-NIT, ND-track, MRtrix and DT-PICo tractography. The ROIs are shown in Figure 5.11. These ROI locations are chosen to demonstrate the behaviour of the tractography algorithm while passing through a region of high dispersion in two opposing directions with streamlines evolving from each region encountering a different polarity of fanning.

The region surrounding the internal capsule and corona radiata illustrated in Figure 2.7 is one of high dispersion in the anterior-posterior orientation. When tracking through this region, ignorance of sub-voxel fanning can cause certain projection-fibres to be missed, especially those travelling through the anterior limb of the internal capsule. Using both a tractography algorithm exploiting Bingham models of dispersion both with and without neighbourhood exploration, the full range of cortical connections are recovered. However, when tracking from a region in the superior regions of the cortex, the fanning polarity is opposed, hence dispersion of tract trajectories in this direction will lead to false positives. When tracking from a seed region in the superior pre-central gyrus, due to the ignorance of fanning polarity, the connectivity estimates given by the ND-track algorithm which does not utilise neighbourhood exploration bleed anteriorly into the frontal lobe, which is in opposition to known anatomy. Using neighbourhood exploration, the NODDI-NIT algorithm tracks directly down to the cerebral peduncle as would be expected.

Further validation of the performance of NODDI-NIT is given in Figure 5.13, which shows similar results obtained in both hemispheres of one subject, and Figures 5.14 and 5.15 which shows the results from NODDI-NIT in 4 further subjects and contrasts with results from MRtrix.

Tractography is also performed with NODDI-NIT on 3 major white matter pathways, which are reliably defined by standard tractography algorithms: the inferior longitudinal fasciculus (ILF), the inferior occipito-frontal fasciculus (IFOF) and the cingulum (Ci) using ROI and waypoint placement guidance derived from [23] and [80], for validation of expected performance in standard tracts. The results are shown in Figure 5.16 with results from MRtrix tractography performed with the same ROIs and waypoints. These results validate expected performance on standard WM structures which are well defined by established algorithms.

All *in vivo* results are displayed as visitation maps with a threshold of 1% of maximum intensity.

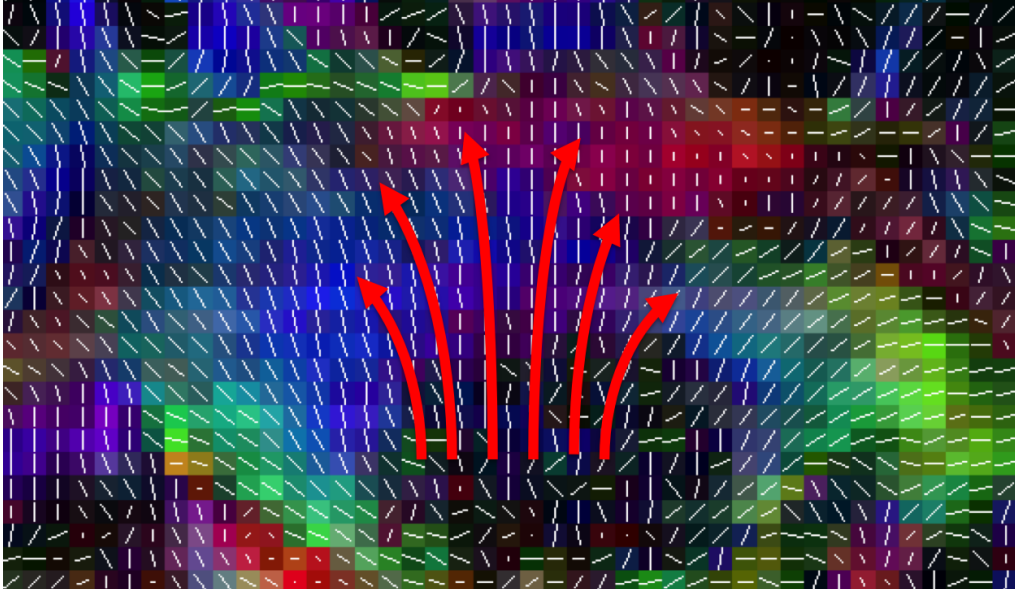


Figure 5.10: Mean directions of Bingham distributions in a sagittal slice in the Corona Radiata, showing the directional dispersion and polarity. The red arrows illustrate the dispersing structure.

## 5.4 Discussion

This section has presented a tractography algorithm which combines structural information drawn from voxels in the immediate neighbourhood of the tracking location with information from a local model capturing sub-voxel fibre orientation dispersion. By capturing fibre dispersion in the model underpinning the tractography algorithm, we can address the underestimation of connectivity caused by underestimation of the true spread of directions available in a voxel exhibiting orientation dispersion in the underlying fibre architecture. Furthermore, the results show that by forming a joint distribution in a neighbourhood exploration scheme which propagates trajectories from the local model into the immediate voxel neighbourhood and examines their coherence with forthcoming structure, we can directly address one of the key ambiguities of antipodally symmetric fODFs: fanning polarity.

Experiments on simulated data show that by addressing the ambiguities of utilising fODFs capturing dispersion, this enables us to exploit the full range of trajectories suggested by a model of dispersion while mitigating the effect of false positives due to

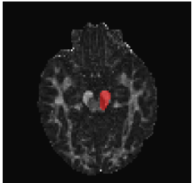
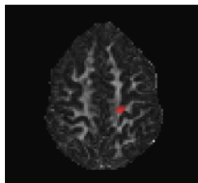
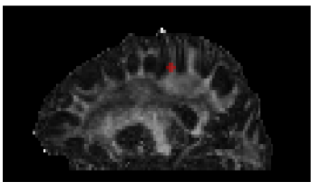
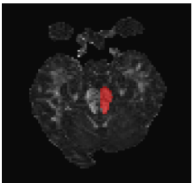
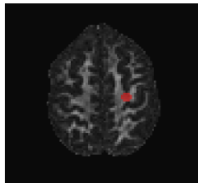
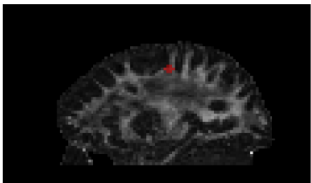
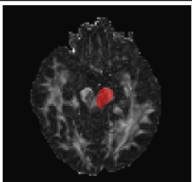
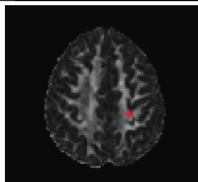
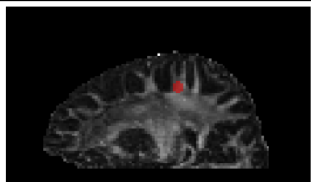
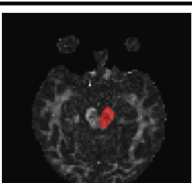
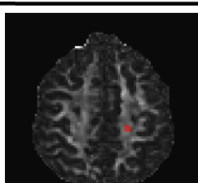
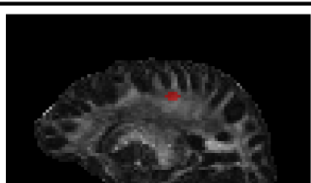
|           | Right peduncle  | Right pre-central gyrus (axial and sagittal)   |   |
|-----------|---|--|---|
| Subject 1 |    |    |    |
| Subject 2 |   |   |   |
| Subject 3 |  |  |  |
| Subject 4 |  |  |  |

Figure 5.11: ROIs used for the *in vivo* experiments. ROIs are manually outlined to cover the whole of the corticospinal tract and the pons in the region of the cerebral peduncle, and a location in the white matter in the superior portion of the pre-central gyrus.

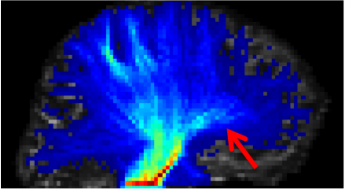
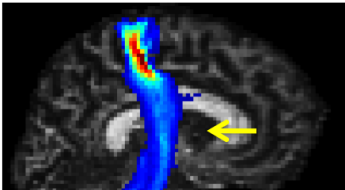
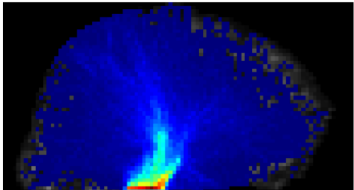
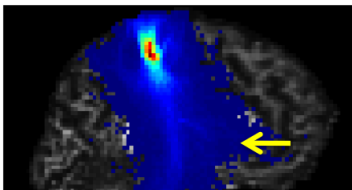
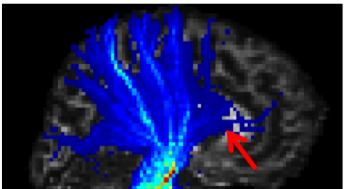
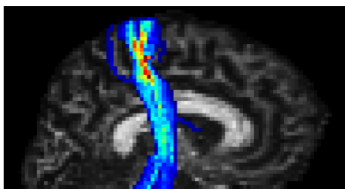
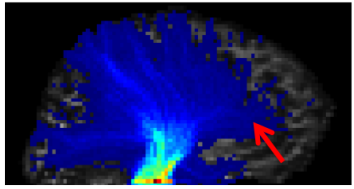
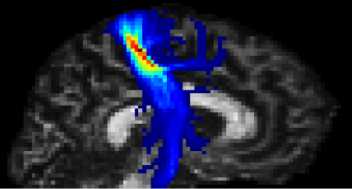
|                  | From cerebral peduncle  | From superior precentral gyrus  |
|------------------|---|---|
| <b>NODDI-NIT</b> |    |    |
| <b>ND-track</b>  |   |   |
| <b>DT-PICo</b>   |  |  |
| <b>MRtrix</b>    |  |  |

Figure 5.12: Tractography from a seed region in the cerebral peduncle and a seed region in the superior portion of the pre-central gyrus with four different algorithms. The red arrows show the anterior connections which are recovered by NODDI-NIT, but are missed or under-represented by alternative algorithms. The yellow arrows point to the region where false positives occur if neighbourhood exploration is not used.

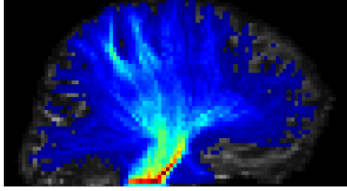
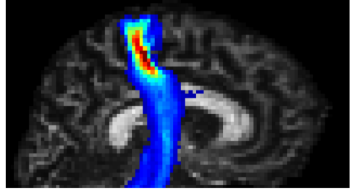
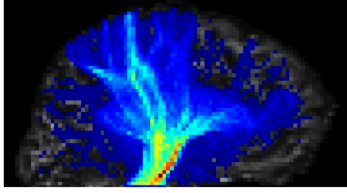
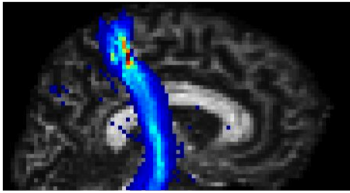
|                  | From cerebral peduncle   | From superior precentral gyrus  |
|------------------|--|---|
| Left hemisphere  |  |  |
| Right hemisphere |  |  |

Figure 5.13: Tracking from a seed region in the cerebral peduncle and a seed region in the superior portion of the pre-central gyrus for each hemisphere of one subject.

ambiguities in the fODF. Due to the NODDI model using a single Bingham distribution to model fibre architecture, this presents problems for the NODDI-NIT algorithm in crossing fibre regions, as demonstrated by the results on the crossing phantom shown in Figure 5.9. NODDI-NIT produces false positives in this synthetic dataset, as the neighbourhood exploration framework follows the Bingham mean directions, which can align with the 2nd fibre population which crosses the one the algorithm is initially following. This represents a failure case for the current formulation of the algorithm. Future work to explicitly model multiple fibre populations in the NODDI model would fix this problem. The neighbourhood exploration framework could be extended to take into account multiple Bingham distributions per voxel.

Experiments on *in vivo* data examined the behaviour of the algorithm in real data when passing through an area known to exhibit significant dispersion with a clear and easily identifiable polarity: the internal capsule and corona radiata, focusing on the connections between the cerebral peduncle and the superior, anterior and posterior regions

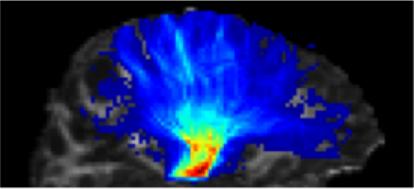
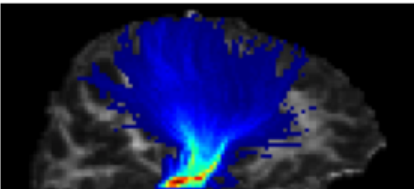
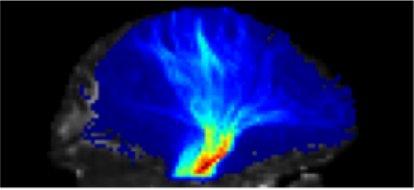
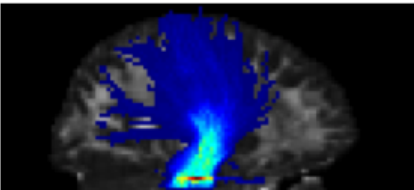
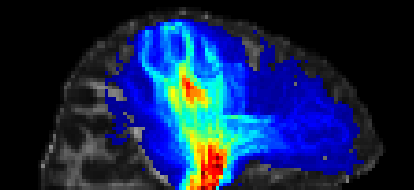
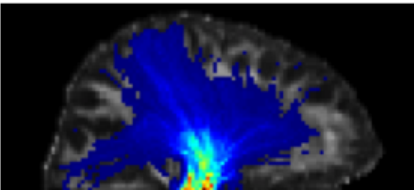
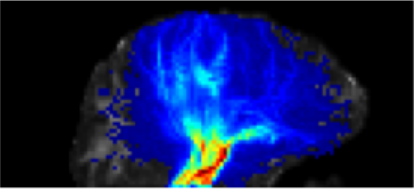
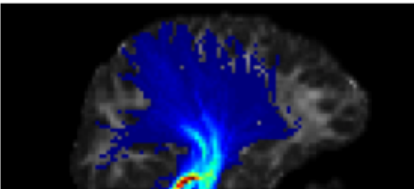
|           | NODDI-NIT   | MRtrix   |
|-----------|---|--|
| Subject 1 |    |    |
| Subject 2 |   |   |
| Subject 3 |  |  |
| Subject 4 |  |  |

Figure 5.14: Tractography from a seed region in the cerebral peduncle in four subjects, using NODDI-NIT and MRtrix.

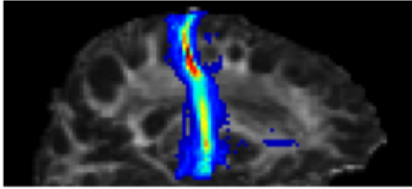
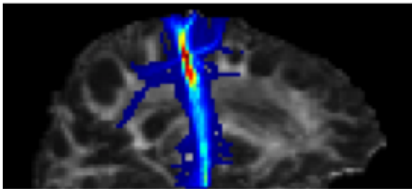
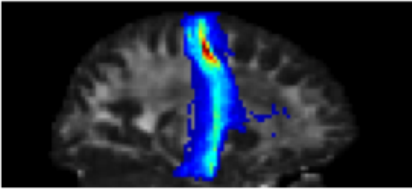
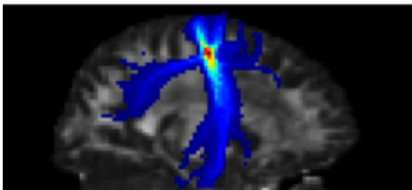
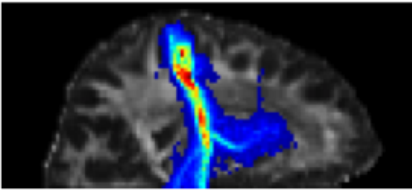
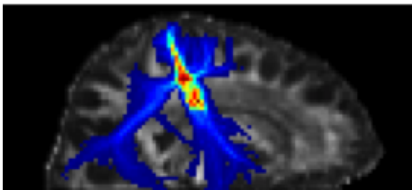
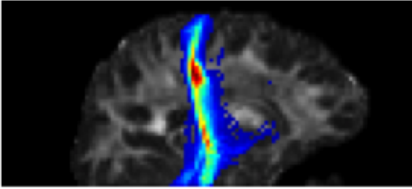
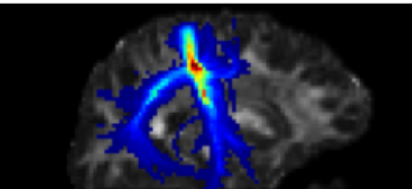
|           | NODDI-NIT  | MRtrix  |
|-----------|--|---|
| Subject 1 |    |    |
| Subject 2 |   |   |
| Subject 3 |  |  |
| Subject 4 |  |  |

Figure 5.15: Tractography from a seed region in the superior portion of the pre-central gyrus in four subjects, using NODDI-NIT and MRtrix.

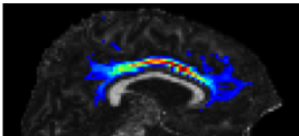
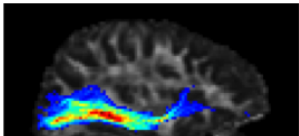
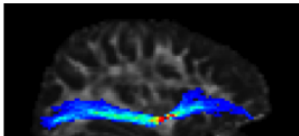
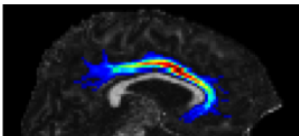
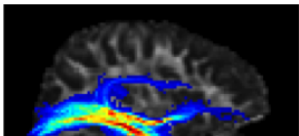
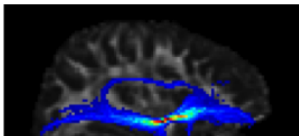
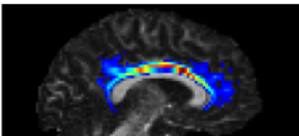
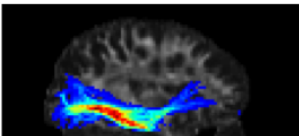
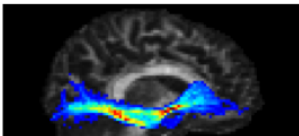
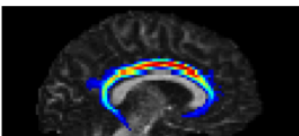
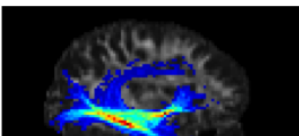
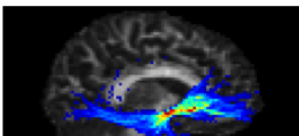
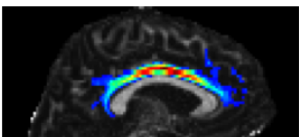
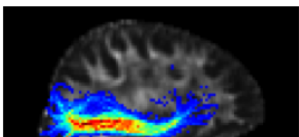
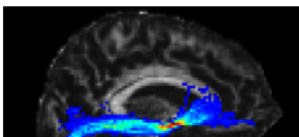
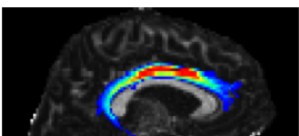
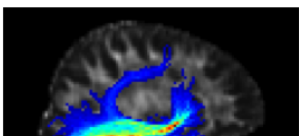
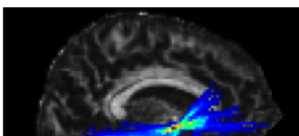
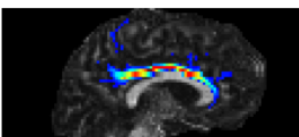
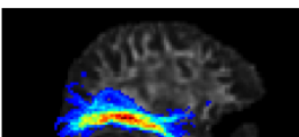
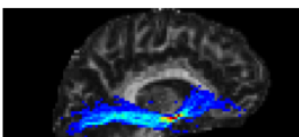
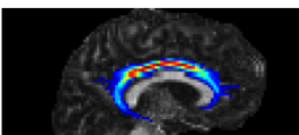
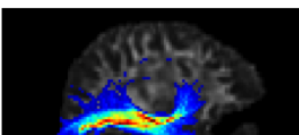
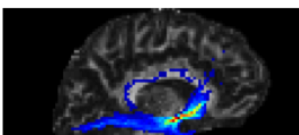
|                  | Cingulum  | ILF  | IFOF  |
|------------------|---|--|---|
| <b>NODDI-NIT</b> |    |    |    |
| <b>MRtrix</b>    |    |    |    |
| <b>Subject 1</b> |   |  |   |
| <b>NODDI-NIT</b> |    |    |    |
| <b>MRtrix</b>    |   |   |   |
| <b>Subject 2</b> |   |  |   |
| <b>NODDI-NIT</b> |  |  |  |
| <b>MRtrix</b>    |  |  |  |
| <b>Subject 3</b> |   |  |   |
| <b>NODDI-NIT</b> |  |  |  |
| <b>MRtrix</b>    |  |  |  |
| <b>Subject 4</b> |   |  |   |

Figure 5.16: Tractography in 3 major WM fascicles for validation: the cingulum, the inferior longitudinal fasciculus (ILF) and the inferior fronto-occipital fasciculus (IFOF).

of the cortex. In this region, there is clear and significant spreading of fibres as they travel superiorly, while in the opposing direction there is clear convergence. This structural arrangement is obvious in both histological specimens and the gross structure clear in visualisations of directional information derived from DW-MRI, exemplified in Figure 5.10.

The results presented in Figure 5.12 demonstrate that by utilising models dispersion in tractography, we recover the full range of connectivity throughout the corona radiata, both with and without neighbourhood exploration, while tracking from a seed region located in the cerebral peduncle. A significantly greater degree of streamlines project towards the anterior portions of the cortex, these connections are far less strongly represented in the MRtrix result and not captured at all by DT-PICo. We hypothesize that these may be fronto-pontine fibres. Figures 5.13, 5.14 and 5.15 further demonstrate that this is a repeatable result across multiple subjects.

The advantage of utilising neighbourhood exploration becomes clear when tracking in the direction opposing dispersion, from a superior region of the cortex. Utilising dispersion models without neighbourhood exploration produces false positive results, with spreading both posterior and anterior which is in conflict with known anatomy. By utilising the neighbourhood exploration scheme, these false positives are eliminated, and the tracks are directed strongly downwards towards the cerebral peduncle, as expected. NODDI-NIT gives a strong connection between the superior pre-central gyrus and peduncle. The connection is weaker for MRtrix tractography, suggesting that MRtrix streamlines spread significantly in this direction.

## 5.5 Conclusions

We have presented in this chapter a new tractography algorithm combining parametric models of sub-voxel fibre dispersion with a neighbourhood exploration framework pooling information from voxels in the neighbourhood of the streamline front to address the

issue of fanning polarity. We have demonstrated in simulations and real data that the algorithm successfully explores dispersion in regions of high fibre dispersion while mitigating false positives arising from ambiguities in the voxel-wise fODFs.

Although tractography is subject to bias from the manual placement of ROIs, importantly in this study we have compared the results of multiple tractography algorithms using identical ROIs in each subject, demonstrating that the incorporation of sub-voxel fibre dispersion in the model allows exploration of more connectivity in dispersing regions while the neighbourhood exploration framework avoids the pitfall caused by the ambiguity of fanning polarity.

Currently the algorithm exploits the Bingham NODDI model, which assumes a single mean direction for a set of dispersing fibres in a voxel. Future work will extend the model to account for multiple mean directions for populations of dispersing fibres.

# Chapter 6

## Connectivity

### 6.1 Introduction

In the previous chapters we presented novel tractography algorithms based on parametric models of sub-voxel fibre dispersion. Examining the effect of the new tractography method proposed in the previous chapter on the derivation of global structural connectivity is instructive in further examining the impact on connectivity estimation. It also provides another opportunity for validation. Results in the previous chapters demonstrated that accounting for dispersion in the model on which the tractography algorithm is based addresses false negatives which arise when using other algorithms based on simpler WM tissue models.

In this chapter we examine the impact of the new tractography algorithm on connectivity between distinct brain regions. We focus on two separate cases of global connectivity: cortico-cortical connectivity in the whole brain network and thalamo-cortical connectivity.

Studying the brain as a network has been a powerful application of tractography [55, 49, 48, 27, 26, 93, 51, 50], giving new insights into the structural organisation of the brain which can be derived from live human subjects, showing that the network organisation of the brain exhibits small-world properties [50, 55].

Methods of analysis of structural brain networks vary from an examination of common graph-theory network metrics such as node degree distribution, efficiency, small world attributes, vulnerability, centrality and motifs [55], to multivariate statistical analysis across a large cohort of subjects [93] and principal network analysis (PNA) [27].

As we only have a small number of subjects, we choose PNA as a simple and robust method of extracting prominent network features and contrasting between the networks derived via NODDI-NIT and an alternative tractography method. PNA allows us to extract the most prominent subnetworks of the whole and look at the organisation of the locations of the most influential nodes and edges.

Secondly we look at thalamo-cortical connections [14, 40, 68]. We contrast the connectivity profiles of the thalamus derived via NODDI-NIT with PICO tractography from the Camino software toolkit [31], based on the DT model, henceforth referred to as 'DT-PICO'. This provides an apt comparison as we contrast a well established single fibre uODF method, which does not explicitly account for sub-voxel fibre dispersion, with tractography based on the dispersing fODF of the NODDI model.

## 6.2 Principal networks

### 6.2.1 Introduction and theory

Principal network analysis (PNA), first proposed in the context of DW-MRI derived network analysis by Clayden *et al* [27], is an elegant way of identifying influential subnetworks which can highlight some key informative features of the network as a whole. The technique is shown to robustly identify influential subnetworks that are stable, meaningful and reproducible. Clayden shows in [27] that principal networks derived from tractography-derived brain connectivity are consistent on rescanning the same patient.

A graph is defined by an association matrix  $\mathbf{A}$ , the elements  $A_{ij}$  defining a measure

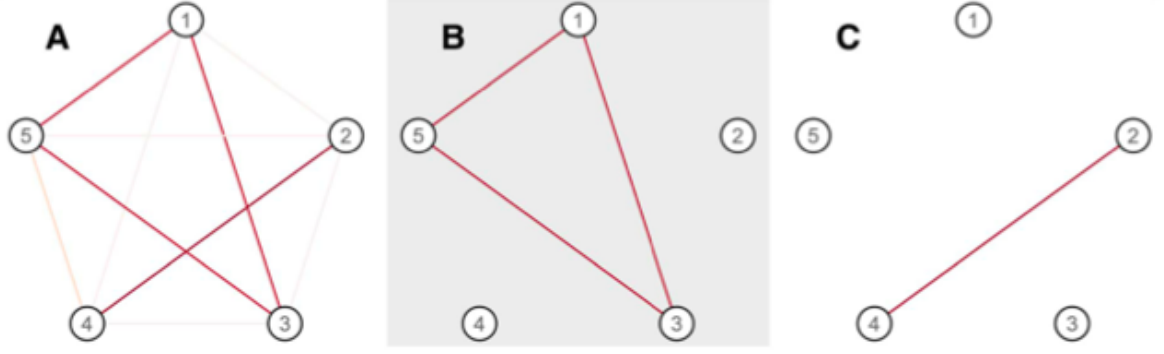


Figure 6.1: Illustration of principal networks approach on a simple example. Network A can be broken down in to its first (B) and second (C) principal network via PNA, capturing the two canonical subnetworks in the whole. Figure from [27]

of the connectivity between regions, or nodes,  $i$  and  $j$ .

PNA starts with the eigendecomposition of the association matrix  $\mathbf{A}$ :

$$\mathbf{A} = \mathbf{Q}\mathbf{\Lambda}\mathbf{Q}^{-1} \quad (6.1)$$

where  $\mathbf{\Lambda}$  is a diagonal matrix of eigenvalues  $\lambda_k$  and  $\mathbf{Q}$  is a matrix for which the columns are the  $\mathbf{M}$  eigenvectors of the association matrix  $\mathbf{A}$ . Principal network analysis is similar in principle to principal component analysis (PCA). If  $\mathbf{A}$  were a correlation matrix, such as in functional connectivity analysis, then  $\mathbf{Q}$  would correspond to the loading matrix of a PCA transformation of the original data [27]. The loading matrix provides the mapping of the values contained in the data matrix,  $\mathbf{A}$ , which in this case is the association matrix, to the principal component axes. The magnitude of each eigenvalue  $\lambda_k$  indicates the degree of influence of the corresponding component in the association matrix.

To identify principal network  $k$ , we calculate a partial association matrix  $\tilde{\mathbf{A}}^k$ :

$$\tilde{\mathbf{A}}_{ij}^k = \lambda_k \mathbf{Q}_{ik} \mathbf{Q}_{jk} \quad (6.2)$$

The full association matrix is the sum of the component matrices  $\tilde{\mathbf{A}}_{ij}^k$ . Each partial association matrix  $\tilde{\mathbf{A}}^k$  defines a subnetwork which has an importance within the network as a whole related to the magnitude of its respective eigenvalue  $\lambda_k$ . Those partial associa-

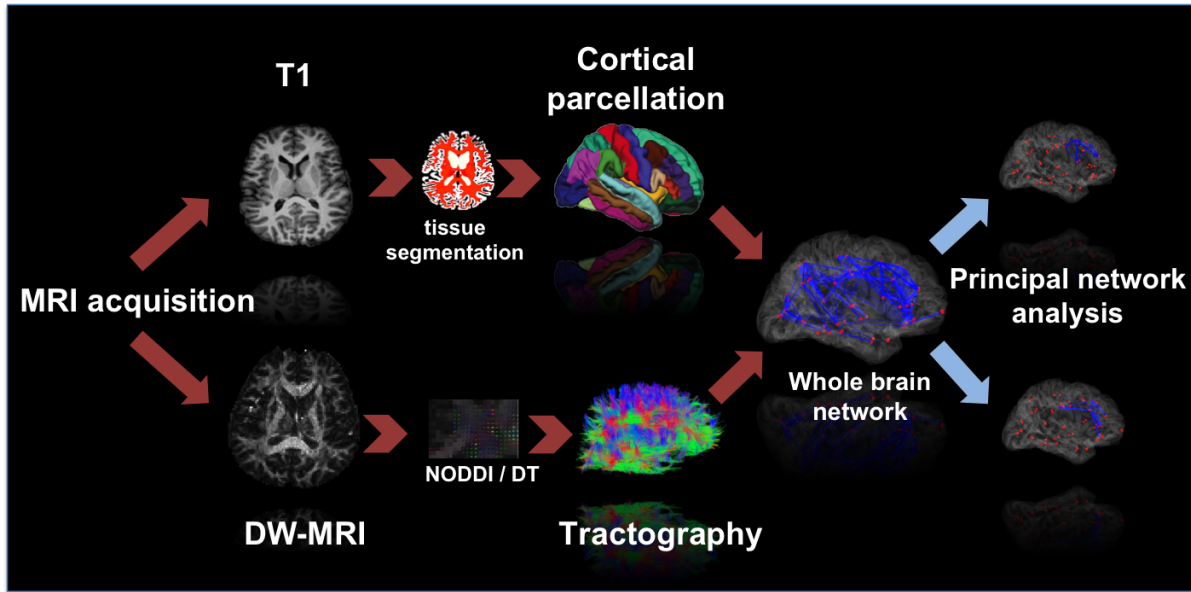


Figure 6.2: Extraction of whole brain structural connectivity network and principal network analysis. A T1 weighted image is used for segmentation and cortical parcellation and a DW-MRI image is used for tractography. The parcellation and tractography are then combined to derive the whole brain structural connectivity network. Influential subnetworks are then extracted from the whole brain network using PNA.

tion matrices which correspond to the largest eigenvalues represent the most prominent and influential subnetworks within the network as a whole.

The principal network method allows us to examine the impact on the derived brain connectivity of the NODDI-NIT method proposed in chapter 5 in an informative and meaningful way. By examining the structure of the most influential subnetworks we can observe changes between subjects and between the networks derived via NODDI-NIT and DT-PICo tractography.

### 6.2.2 Methods

In this section, we derive matrices of inter-connectivity between 64 separate cortical regions defined by the Desikan atlas [36]. The regions are listed in table 6.1 with associated indices for reference and can be seen overlaid on the inflated brain surface shown in Figure 6.3. The datasets for subjects 1-4 were used from section 5.1. The diffusion data was processed using the NODDI toolbox [135, 1] modified to fit Bingham param-

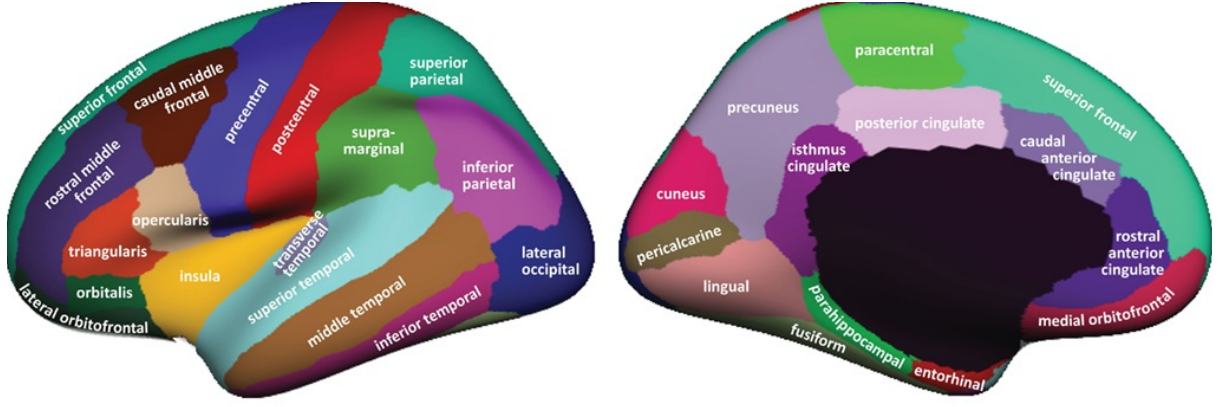


Figure 6.3: Desikan-Killiany atlas used for parcellating the cortex. Image taken from [2]

eters for the NODDI-NIT algorithm. The diffusion weighted data was also processed using the DT model by the Camino software package [31] in preparation for tractography. The T1 weighted images of each subject were parcellated into 64 cortical regions using the FreeSurfer software package [44]. The skull-stripped T1 images in FreeSurfer space were registered with the skull-stripped (FSL BET [107])  $b = 0$  image of the diffusion weighted acquisition using FSL-FLIRT (FSL FLIRT [61, 60]) into diffusion space. The affine transformation derived from this registration procedure was then used to initialise non-linear registration of the skull-stripped T1 images to the  $b = 0$  image using FSL-FNIRT. The warp field from this procedure was then used to reslice the cortical parcellation into diffusion space. 1 probabilistic streamline was seeded per WM voxel using each of the 2 different algorithms: the NODDI-NIT algorithm described in chapter 5 and a DT based PICO algorithm, from the Camino software package [31]. Each seedpoint was subject to random jitter within the voxel to avoid any bias from the voxel grid structure. Connectivity was quantified between ROI pairs as the sum of connecting streamlines divided by the mean number of voxels in each connected ROI to normalise for the size of the respective ROIs. A schematic illustration of the process of whole brain network derivation and PNA is given in Figure 6.2.

| GM region name                            | Index (left) | Index (right) |
|---|--------------|---------------|
| caudal anterior singular cortex           | 1            | 33            |
| caudal middle frontal gyrus               | 2            | 34            |
| cuneus                                    | 3            | 35            |
| enthorinal cortex                         | 4            | 36            |
| fusiform gyrus                            | 5            | 37            |
| inferior parietal gyrus                   | 6            | 38            |
| inferior temporal gyrus                   | 7            | 39            |
| cingulate gyrus, isthmus                  | 8            | 40            |
| lateral occipital cortex                  | 9            | 41            |
| lateral orbitofrontal cortex              | 10           | 42            |
| lingual gyrus                             | 11           | 43            |
| medial orbitofronal gyrus                 | 12           | 44            |
| middle temporal gyrus                     | 13           | 45            |
| parahippocampal gyrus                     | 14           | 46            |
| paracentral gyrus                         | 15           | 47            |
| inferior frontal gyrus, pars opercularis  | 16           | 48            |
| inferior frontal gyrus, pars orbitalis    | 17           | 49            |
| inferior frontal gyrus, pars triangularis | 18           | 50            |
| pericalcarine cortex                      | 19           | 51            |
| postcentral gyrus                         | 20           | 52            |
| posterior cingulate gyrus                 | 21           | 53            |
| precentral gyrus                          | 22           | 54            |
| precuneus                                 | 23           | 55            |
| rostral anterior cingulate cortex         | 24           | 56            |
| rostral middle frongal gyrus              | 25           | 57            |
| superior frontal gyrus                    | 26           | 58            |
| superior parietal gyrus                   | 27           | 59            |
| superior temporal gyrus                   | 28           | 60            |
| supramarginal gyrus                       | 29           | 61            |
| frontal pole                              | 30           | 62            |
| temporal pole                             | 31           | 63            |
| transverse temporal gyrus                 | 32           | 64            |

Table 6.1: Cortical GM regions from FreeSurfer parcellation and associated labels.

### 6.2.2.1 Principal network calculation:

Principal networks were calculated using the theory outlined in section 6.2.1 applied to the association matrices derived from tractography. To extract meaningful and comparable subnetworks, a threshold was lowered on each PN until 10 edges were found. If less than 10 edges were present in any PN, then the maximum number of edges was retained.

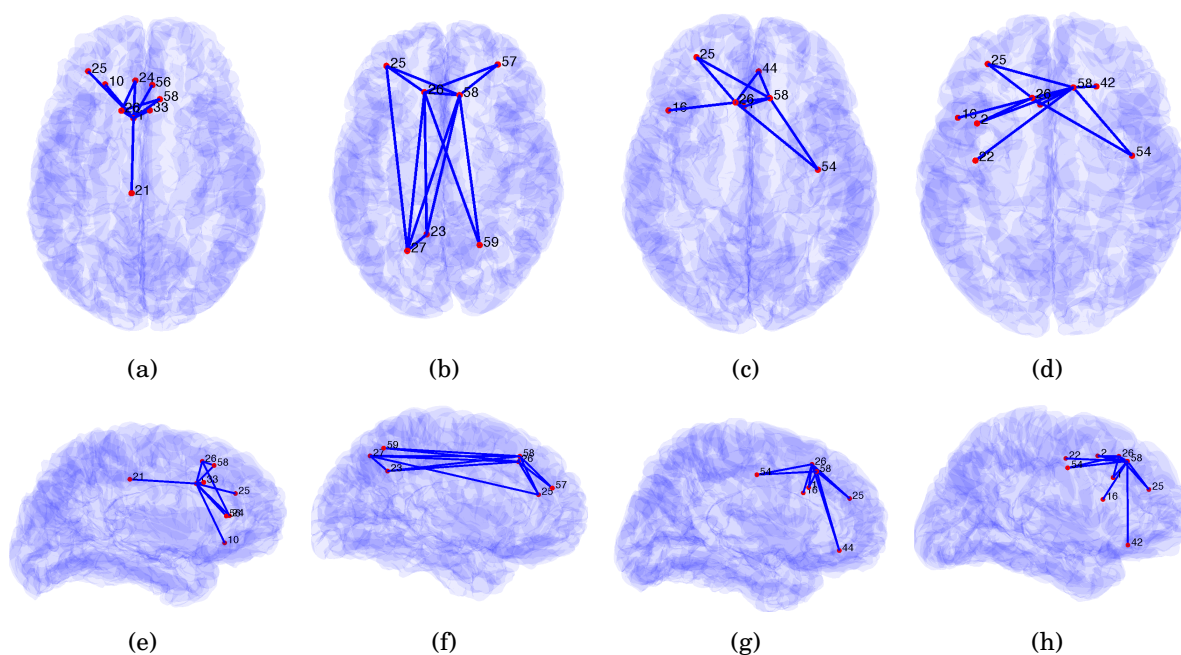


Figure 6.4: First principal network of 4 subjects derived using NODDI-NIT: axial view (top row: a-d) sagittal view (lower row: e-h). See table 6.1 for cortex regions corresponding to numeric indices.

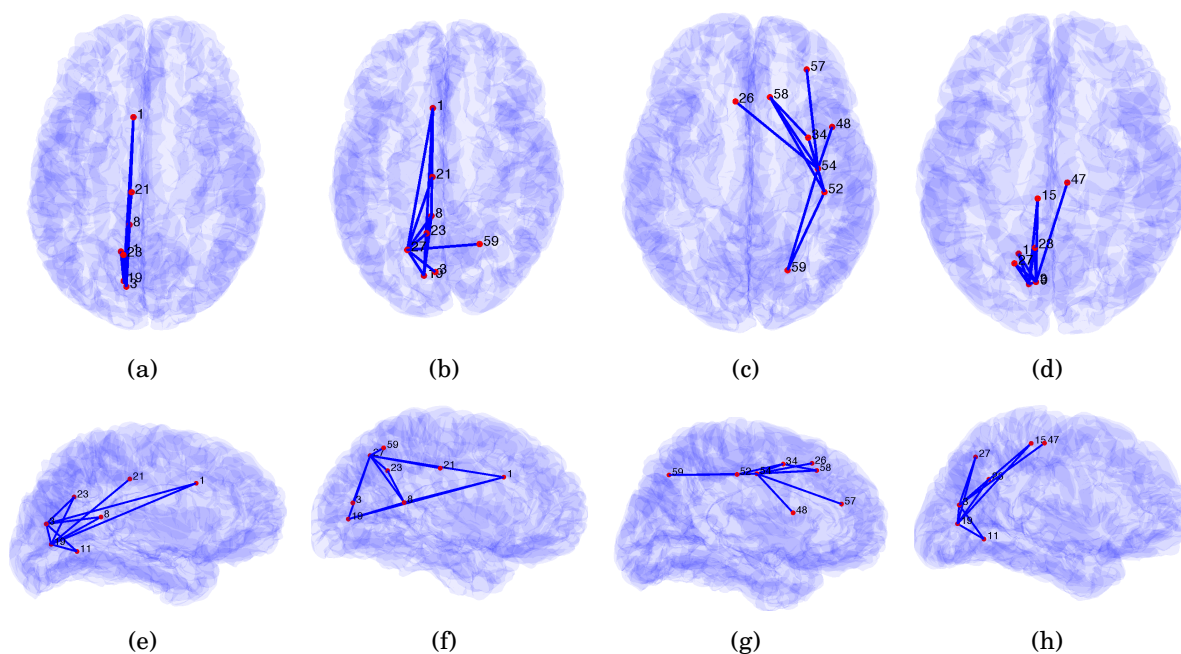


Figure 6.5: First principal network of 4 subjects derived using DT-PICo: axial view (top row: a-d) sagittal view (lower row: e-h). See table 6.1 for cortex regions corresponding to numeric indices.

### 6.2.3 Results

Figures 6.4 and 6.5 show the first PNs for 4 subjects. In Figure 6.4 the principal networks were calculated from networks derived via NODDI-NIT, in Figure 6.5 the network was derived using DT-PICo tractography. The second principal networks can also be seen in appendix C. The principal networks are thresholded until 10 edges are found. The location of each vertex is based on the spatial median of the corresponding region from the voxel-wise whole brain parcellation. Table 6.2 shows the lobe associations of the vertices in the first PN in each subject derived from NODDI-NIT and table 6.3 shows the lobe associations of the vertices in the first PN in each subject derived from Camino tractography.

The PNs shown in Figures 6.4 and 6.5 show clearly that in the networks derived via NODDI-NIT frontal intralobar connectivity is favoured, as frontal regions appear consistently in the first PN of each subject. In the network derived using DT-PICo tractography this is not the case, occipital and parietal regions are more present across subjects. Regions of the frontal cortex were involved in the first PNs derived with NODDI-NIT for all subjects, with the left and right superior frontal gyrus both appearing in every subject, connected by an edge. The left rostral middle frontal gyrus is also present in the first PNs of all subjects and in 3 out of 4 subjects, this is interconnected with both left and right superior frontal gyrus, indicating that this is an important subnetwork of the brain which may be laterally biased.

### 6.2.4 Discussion

The results presented above shown that the choice of tractography algorithm used to derive whole-brain connectivity networks has a significant effect on the features of the derived network. There are distinct differences between the structures of the networks derived using NODDI-NIT and DT-PICo tractography, with the most obvious difference

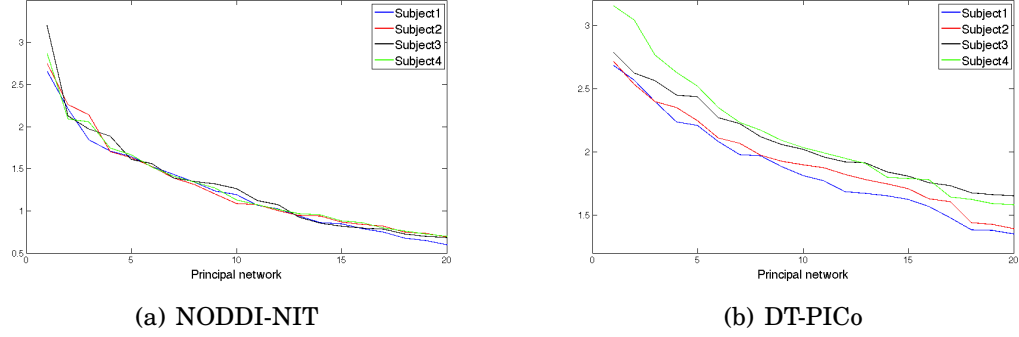


Figure 6.6: Eigenvalues of the first 20 principal networks for each subject. The eigenvalue falloff is very similar, suggesting consistency in subnetwork weighting across networks derived with the same tractography algorithm.

| Subject | Frontal | Parietal | Occipital | Temporal |
|---------|---------|----------|-----------|----------|
| 1       | 8       | 1        | 0         | 0        |
| 2       | 4       | 2        | 0         | 0        |
| 3       | 7       | 0        | 0         | 0        |
| 4       | 7       | 0        | 0         | 0        |

Table 6.2: Lobe association of nodes in principal networks derived using NODDI-NIT.

| Subject | Frontal | Parietal | Occipital | Temporal |
|---------|---------|----------|-----------|----------|
| 1       | 1       | 3        | 3         | 0        |
| 2       | 1       | 5        | 2         | 0        |
| 3       | 6       | 2        | 0         | 0        |
| 4       | 2       | 2        | 3         | 0        |

Table 6.3: Lobe association of nodes in principal networks derived using DT-PICo tractography.

being the extensive presence of frontal lobe regions in the most influential networks as derived using PNA. NODDI-NIT derived PNs feature vertices spatially located in the frontal lobe more prominently, whereas DT-PICo tractography derived PNs feature parietal and occipital regions more prominently. 3 regions, the left and right superior frontal gyri and the left rostral middle frontal gyrus appear consistently in first PNs across all subjects using NODDI-NIT, with an edge existing between the left and right superior frontal gyrus in all subjects. These results echo the results given in the previous chapter, which indicated that NODDI-NIT gives prominent frontal connectivity with regions in the cerebral peduncle.

Frontal regions have been reported elsewhere [49] as featuring prominently in the whole brain network. However, [49] identifies a stronger structural core existing in the parietal cortex. Tractoraphy based on DSI is used in [49], which is i) deterministic and ii) does not use a model accounting for fibre dispersion. DSI is a dODF technique, so the tractography is not underpinned by a model directly related to the fODF, and instead only follows discrete directions derived from the maxima of the dODF, this may account for the differences in the results presented above.. A productive focus of future work would be a direct comparison of numerous competing tractography algorithms and the impact of each on estimated features of whole brain connectivity. These regions of the left pre-frontal cortex have been identified as important in language processing in fMRI studies [90]. Regions of the pre-frontal cortex have also been identified as part of the default mode network (DMN) [3]. The DMN is an interconnected cluster of brain regions which appear to be inter-communicating when the brain is not concentrating on any particular task, but is in a state of 'wakeful rest'.

The results suggest that using a tractography algorithm which accounts for sub-voxel dispersion reveals a different pattern of brain connectivity, with regions of the frontal lobe appearing prominently in the network when compared to networks derived via alternative tractography methods. NODDI-NIT derived networks also show a degree of consistency between subjects in the first PNs, with some common vertices and edges

featuring across all subjects.

## 6.3 Thalamic connectivity

The thalamus is a region of subcortical GM situated between the cortex and the midbrain. It functions as a relay for connections coming from the cortex to other areas of the brain and spine and has a role in sleep regulation. It is divided into several separate nuclei which are cytoarchitecturally distinct and connected to distinct brain regions. Probabilistic tractography has previously been used to examine boundaries between thalamic sub-regions *in vivo* [14, 68] by estimating thalamo-cortical connectivity, segmenting distinct thalamic subregions based on the probability of connection to a certain cortical region. This provides a further opportunity to validate the NODDI-NIT algorithm's ability to recover meaningful brain connectivity and to examine any differences with a well-established tractography method.

### 6.3.1 Methods

The thalamus was identified using a FreeSurfer segmentation of the T1 image of each subject. The cortex was also parcellated using FreeSurfer into the cortical zones outlined in the Desikan-Killiany atlas. The cortical regions defined in the Desikan-Killiany atlas are illustrated on the inflated pial surface shown in Figure 6.7. Several of the regions defined in the Desikan-Killiany atlas were merged to form larger cortical targets based on the major lobes of the brain - frontal, parietal, temporal and occipital. The pre-central and post-central gyrus are separated. The frontal lobe is divided into four separate regions to examine the impact on estimated thalamo-frontal connectivity which is caused by modelling the dispersion in the anterior part of the corona radiata and centrum semiovale. The cortical regions are illustrated in table 6.3.1 and Figure 6.7

For hard segmentation of thalamic sub-regions each thalamic voxel was classified as connected to the ipsilateral cortical zone with which it had the highest probability of

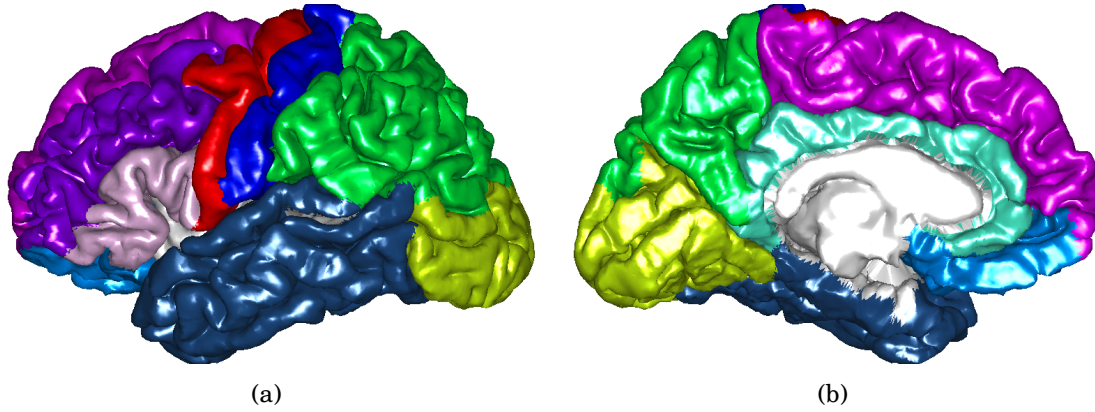


Figure 6.7: Division of the cortex into 10 separate target regions for tractography to facilitate examination of thalamo-cortical connectivity. Rendered on a single subject's brain.

connectivity.

### 6.3.2 Results

Thalamic segmentations of the left thalamus are shown for 3 subjects in Figure 6.9. The segmentations show consistency between subjects and a large amount of agreement between the two separate tractography algorithms. DT-PICo tractography is consistently missing a region most probably connected to the post-central gyrus, while NODDI-NIT has a significant region most probably connected to the post-central gyrus in all subjects. This may be a symptom of fibre dispersion in the centrum semiovale between the thalamus and the post-central gyrus which is not modelled by the DT model on which the tractography is based.

Figure 6.8 shows probabilistic maps of connectivity for each target region in subject 1. NODDI-NIT identifies a small region of the anterior nucleus of the thalamus connected to the occipital and temporal lobes, which DT-PICo does not. These connections are possibly through the cingulum WM bundle. The most obvious differences arise in the connectivity profiles to the medial, inferior and orbito-frontal regions of the frontal lobe. DT-PICo tractography suggests the areas connected to these regions as largely co-located in the medial part of the thalamus, while NODDI-NIT suggests they exist more laterally.

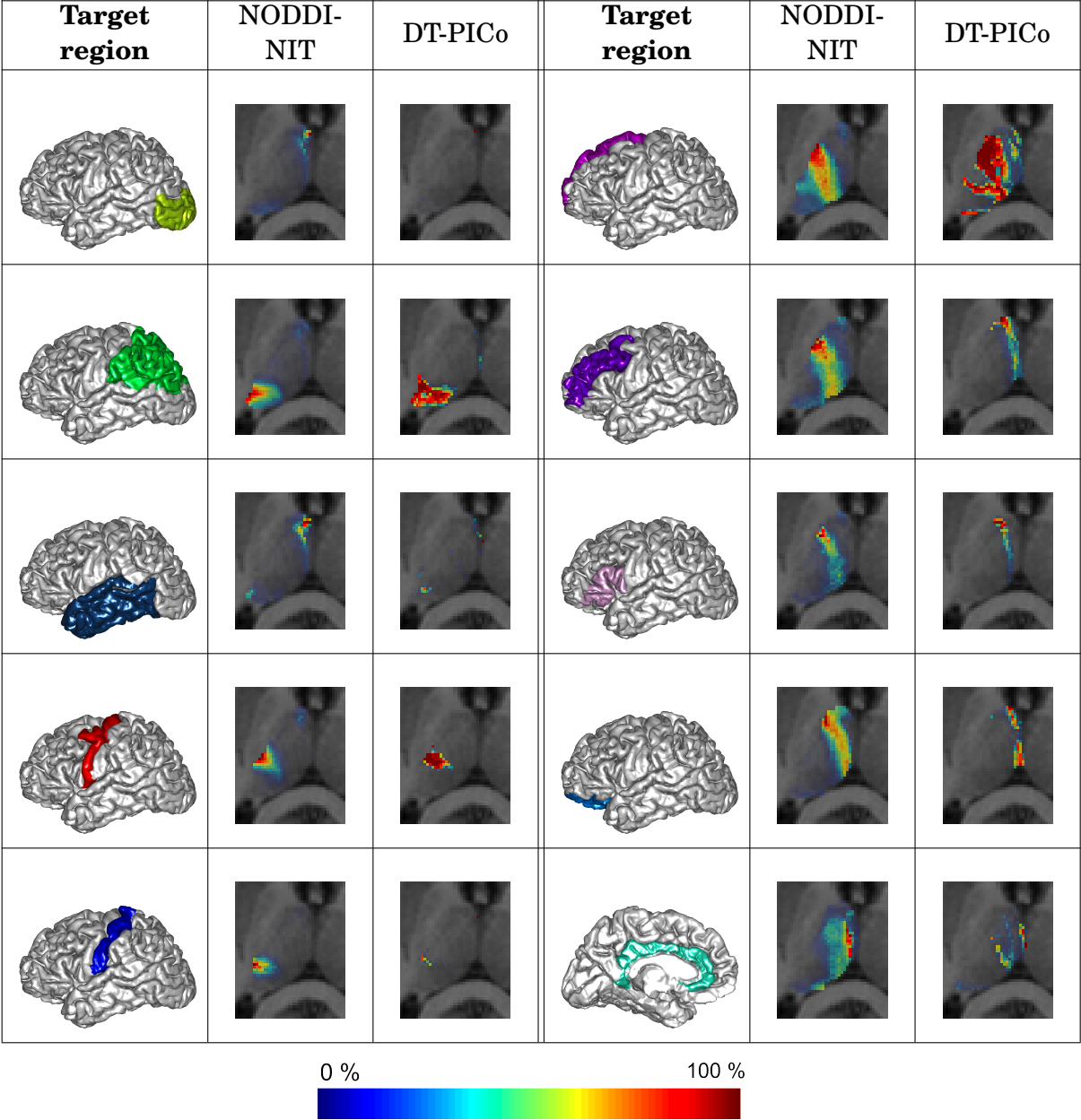


Figure 6.8: Probabilistic mapping of cortical connections to target regions shown in Figure 6.7 for subject 1. Each cortical target region is shown with the probabilistic maps from both NODDI-NIT and DT-PICo.

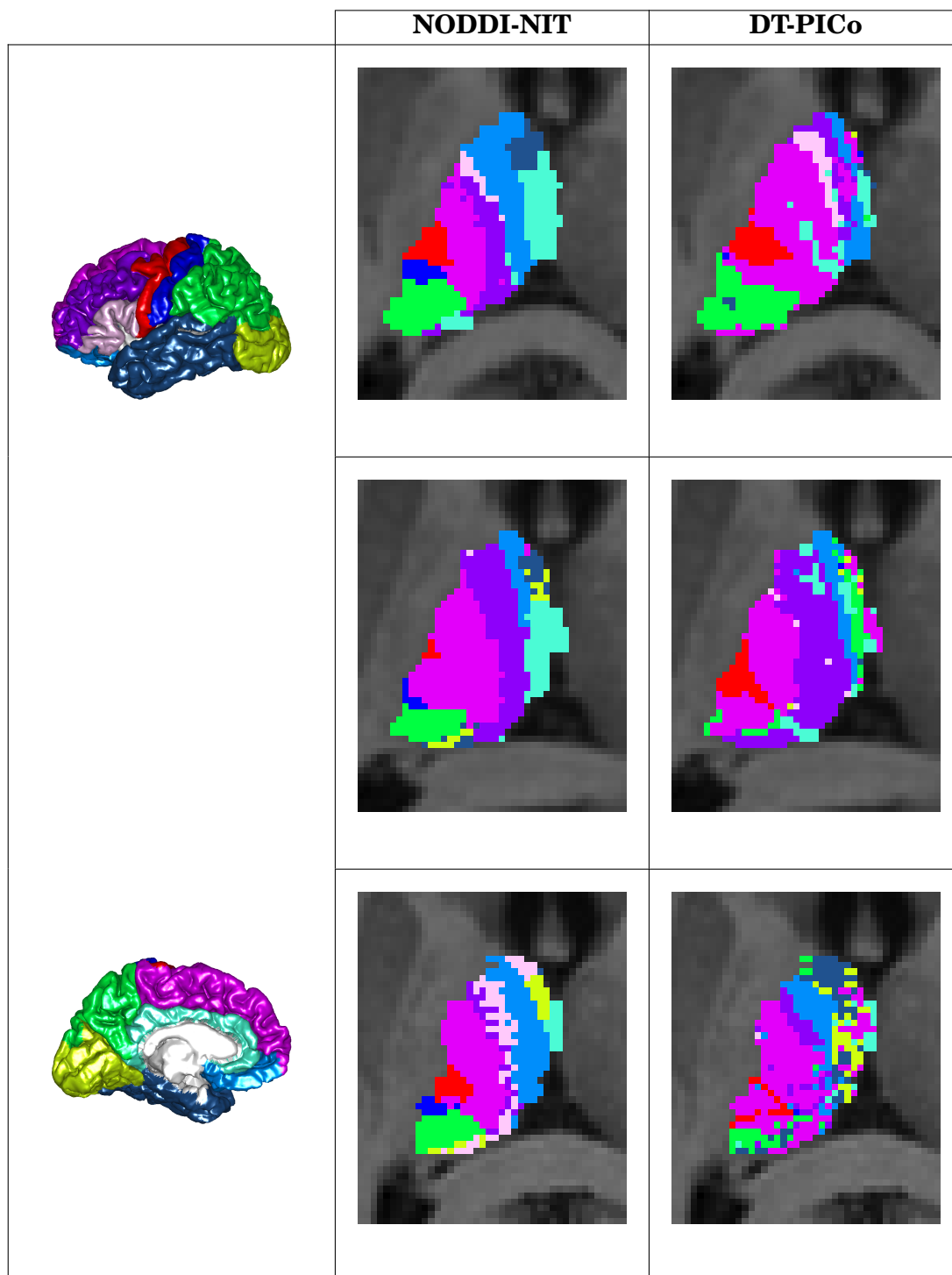


Figure 6.9: Connectivity based segmentation of the thalamus. Colours correspond to the cortical region of the same colour shown in Figure 6.7 and table 6.3.1. The cortical regions and corresponding colours are given in the left column for reference.

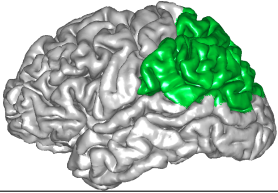
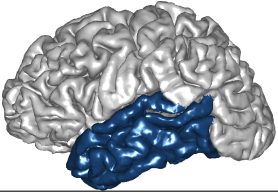
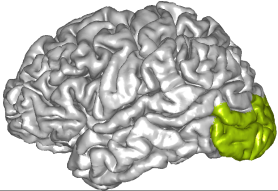
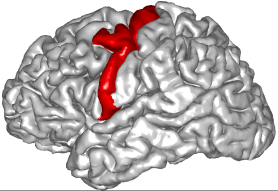
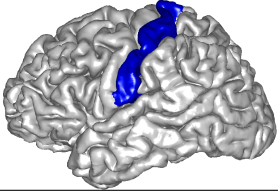
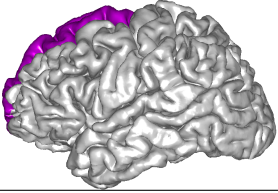
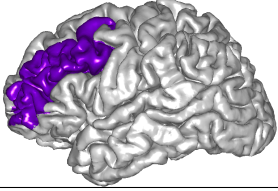
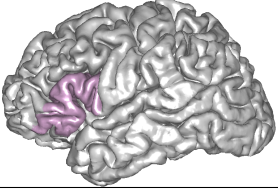
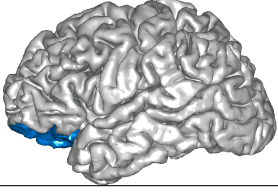
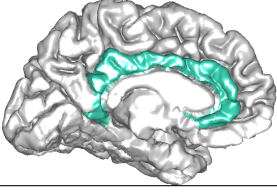
|   |                                       |  |                           |
|---|---------------------------------------|--|---------------------------|
|    | Parietal lobe                         |    | Temporal lobe             |
|    | Occipital lobe                        |    | Pre-central gyrus         |
|    | Post-central gyrus                    |    | Frontal lobe:<br>superior |
|   | Frontal lobe:<br>medial               |   | Frontal lobe:<br>inferior |
|  | Frontal lobe:<br>orbitofrontal cortex |  | Cingulate gyrus           |

Table 6.4: Brain regions and associated colours.

### 6.3.3 Discussion

Connectivity profiling the thalamus using NODDI-NIT shows that the algorithm is capable of producing results that are repeatable across subjects, and also shows reasonable similarity with results from a competing, well-established tractography technique. While the results from NODDI-NIT and DT-PICo tractography are broadly similar, there are subtle differences. NODDI-NIT more consistently recovers connectivity between the tha-

lamus and the post-central gyrus. The difference could possibly be explained by the presence of fibre dispersion in the centrum-semiovale, which is not modelled accurately by the DT. Further differences in connectivity are apparent on inspection of Figure 6.8. The clearest differences are in the connectivity profiles of the different regions of the frontal lobe. NODDI-NIT gives higher probability of connection to each frontal region at a more lateral location in the thalamus than DT-PICo. These connections between the thalamus and the pre-frontal cortex pass also pass through the centrum semiovale, where the NODDI model will be more effective at accurately modelling dispersion, which could explain the differences in thalamic connectivity profiles. Fronto-thalamic connectivity is similarly studied elsewhere in [68] and [40]. Klein *et al* [68] focus on the medio-dorsal nucleus of the thalamus so results are not directly comparable, however they do not contradict the results presented here. Draganski *et al* [40] focus on the thalamus and other regions of the basal ganglia, including the putamen, caudate and palladium. The cortical segmentation pattern chosen in [40] is similar, but not identical to that chosen here. Figure 6.8 also shows that NODDI-NIT identifies a region of the anterior nucleus of the thalamus connected to the temporal and occipital lobes, possibly via the cingulum, which DT-PICo tractography does not identify.

## 6.4 Conclusions

In this chapter we examined the impact of NODDI-NIT on cortico-cortical and thalamo-cortical connectivity. We show that NODDI-NIT derived whole brain networks exhibit different properties to those derived using an alternative algorithm with regions in the frontal lobe featuring prominently in the most influential sub-networks. Certain frontal regions appear consistently in the most influential networks across multiple subjects. We also show that NODDI-NIT estimates thalamo-cortical connectivity with good consistency across subjects and estimates the thalamic connections to regions of the frontal lobe to exist more laterally than DT-PICo.

The results suggest modelling WM fibre dispersion to be an important factor in tractography as it has a strong impact on patterns in estimated cortico-cortical connectivity. As neural computation is inextricably linked to connectivity, deriving brain connectivity networks with an accurate tractography method is highly important. Therefore utilising an accurate model of WM structure on which to base the tractography algorithm is a high priority.

The preliminary whole-brain network results presented here are in contrast to other studies on whole-brain connectivity. Other studies identify regions of the parietal cortex [49] and the cingulate gyrus [27] as central cores. Both these studies use alternative tractography methods, [49] uses DSI based tractography and [27] uses tractography based on the ball and stick model [14, 13].

The differences may be explained by the prominence of fibre dispersion in the centrum semiovale / corona-radiata. These regions are identified by NODDI as areas of significant fibre dispersion (see Figure 6.10) [135]. Accounting for this fibre dispersion in the tractography model may facilitate intra-lobar connections which are not detected by tractography algorithms which do not account for fibre dispersion.

While this preliminary study gives some interesting findings, it is limited by the small number of subjects. To better validate the existence of anterior-biased connectivity in the NODDI-NIT derived brain networks a study with many subjects would be ideal. Scan-rescan data for each subject would also allow repeatability to be thoroughly examined. This is an important goal for future work.

With a large number of subjects we could confirm the existence of nodes which are strongly connected across multiple subjects. A study with more subjects might also reveal further structural connectivity trends existing in the less prominent PNs. No obvious trends seem apparent in the second principal networks shown in appendix C although a many subject study would provide a better opportunity to investigate trends in lower ranking sub-networks.

Alternative cortical segmentation could also be beneficial in future investigation.

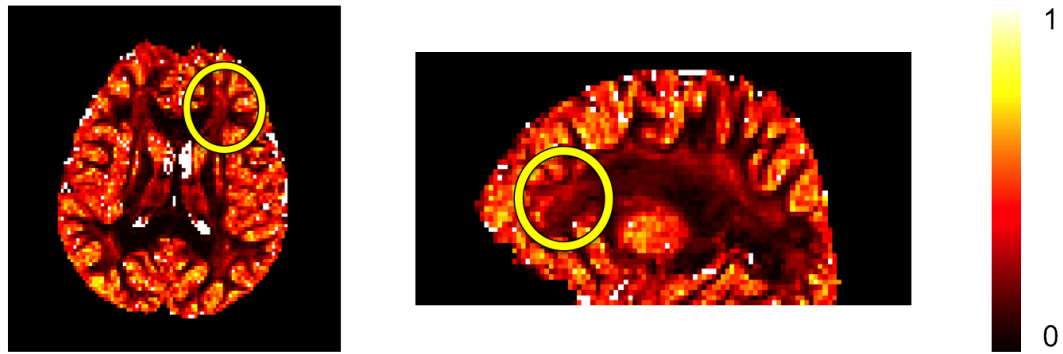


Figure 6.10: NODDI orientation dispersion index (ODI). High values of the ODI indicate regions of high fibre dispersion. The yellow circles highlight the regions of the frontal WM where high fibre dispersion is detected. High fibre dispersion can also be observed throughout the centrum semiovale.

In [50] and [49] a much finer subdivision of the cortex into 500-4000 separate ROIs is used to create targets for tractography. This allows the network to be analysed at higher resolution. Further network analysis techniques such as k-core decomposition, clustering, centrality and efficiency may help reveal further details.

A thorough investigation of frontal intralobar connections would help validate the findings. A framework for investigation of frontal lobe connections via tractography is given by Catani *et al* [77].

# Chapter 7

## Discussion and conclusions

Recent advances in DW-MRI modelling techniques have yielded new parametric models of sub voxel fibre dispersion. These models capture sub-voxel white matter structure more accurately, by specifically modelling expected fibre orientation dispersion, and more robustly, by using a limited number of degrees of freedom in the model. In the search to improve connectivity estimation via tractography, the use of better models is of great importance.

This work has introduced new tractography methods exploiting parametric models of dispersion for improved connectivity estimation and examined the impact of the new methods on connectivity estimation.

During this project a key issue in exploiting advanced DW-MRI models of dispersion in tractography was addressed, that of the ambiguities which arise in fODFs due to the lack of intra-voxel spacial specificity and antipodal symmetry. These ambiguities mean that the difference between fanning structures of opposing polarity, and between fanning and curving structures, cannot be resolved from the information from a single voxel in isolation.

The key contribution of this thesis is the proposal of a tractography method which both exploits parametric models of sub-voxel fibre dispersion and actively addresses the issue of fanning polarity using the concept of the NI-ODF. By using a neighbourhood ex-

ploration scheme, we pool information from multiple voxels to resolve these ambiguities in the information provided by isolated voxels to disambiguate structures of opposing fanning polarity. This is validated in both simulations and real *in vivo* subject data.

In chapter 6 we examined the impact of the newly proposed neighbourhood informed tractography method on connectivity estimation. Whole brain networks derived via NODDI-NIT featured mainly frontal lobe regions among the most prominent networks extracted via PNA with consistency across subjects. This was not reflected in networks derived via a well-established alternative tractography method, suggesting this may be an impact of capturing sub-voxel fibre dispersion in the model underpinning the tractography algorithm. Thorough investigation and validation of this preliminary finding will be a focus of future work.

A summary of the contributions of this thesis is as follows:

- In chapters 4 and 5 we present new tractography algorithms exploiting parametric models of subvoxel fibre dispersion. We show that the use of parametric models of fibre dispersion addresses false negatives of traditional approaches based on simpler models which do not account for dispersion.
- In chapter 5 we present the concept of the NI-ODF: when using parametric models of dispersion in tractography, an ambiguity arises in the interpretation of the local fODFs, that of fanning polarity. We propose a framework to pool information from voxels in the neighbourhood around the streamline front to form the neighbourhood informed ODF (NI-ODF). This allows the full exploitation of dispersion models while mitigating false positives from ambiguities in the local model.
- In chapters 4 and 5 we validate the new tractography algorithms extensively in simulations and real data, showing that utilising models of subvoxel fibre dispersion recovers connectivity in regions of high dispersion, such as the internal capsule and corona radiata, which is missed or under-represented by alternative tractography methods.

- In chapter 6 we show that the new tractography methods presented exhibit differences in estimates of global connectivity to a traditional tractography algorithm, which does not model dispersion, particularly global connections associated with the frontal lobe. We show that frontal lobe regions are more prominent in whole-brain networks derived via the NODDI-NIT algorithm and thalamo-cortical connections to the frontal lobe are also estimated to be from more lateral regions of the thalamus.

A limitation that remains is that the model used in this work does not explicitly model multiple fibre populations per voxel. The model captures crossing fibre structure as dispersion and recruiting extra information provided by curvature priors or neighbourhood exploration, crossing fibre structure can be adequately resolved. However, a more comprehensive model would include the explicit modelling of multiple fibre populations and orientation dispersion in each bundle using multiple Bingham distributions.

This work has presented a methodology for fully exploiting advanced dispersion models in tractography, to address some of the remaining limitations in current tractography methods. This work takes another step towards deriving a more complete picture of the human connectome by using the latest state of the art DW-MRI modelling techniques in tractography.

## 7.1 Future directions

An important modification which would extend the methods presented in this thesis would be the extension of the NODDI model to multiple fibres populations per voxel to more accurately model crossing fibres. Multiple Bingham distributions could be fit per voxel modelling each fibre population and its degree sub-voxel dispersion individually. Although conceptually this is a relatively trivial extension to the model, in practice it is highly challenging. Adding further Bingham fODFs per voxel adds 5 extra parameters per Bingham distribution, and further parameters for any unfixed diffusivities. The

Bingham orientations would have to be carefully initialised using information derived from a multi-fibre model. This can be achieved by initialising the Bingham orientations via spherical deconvolution [92, 65] and calculating peak anisotropy [104].

An extension of the underlying model to include multiple directions also adds technical challenges, but also offers opportunities in any future development of the neighbourhood exploration framework. On traversing voxel with multiple fibre populations a decision must be made about which fibre population to follow. The neighbourhood exploration framework could be modified to help with this decision, looking ahead to find coherence in oncoming structure. This would however be a challenging problem in itself.

Recent work has presented the concept of the track orientation density (TOD) [37]. This work recruits a similar concept, utilising voxel-neighbourhood information to support information gathered from the local fODF. The TOD method functions as a pre-processing step before any tractography is performed. The method works by first integrating many short tracks using CSD-derived voxel-wise fODFs then computing the contributions of each short track to a new ODF, the TOD, in each voxel it intersects, based upon the integral of the tangent to the track at every point within the voxel. The TOD can be thought of as a regularised version of the fODF, based on local support of continuous structure. As it is built from contributions of short streamlines, the TOD favors orientations which lead to similarly oriented structures in neighbouring voxels.

The TOD is, however, antipodally symmetric, hence cannot address the issue of fan-ning polarity which the NI-ODF helps to resolve. Such a technique might provide useful auxiliary information in each voxel. For example, the increased consistency of the TOD may be able to provide peak directions more robustly in a hybrid technique. An extension of the NODDI model to encompass crossing fibres may benefit from accurately derived peak directions from TOD for initialising Bingham distributions for accurate fitting.

One aim of tractography is to build an accurate picture of the human connectome, to better our understanding of how the brain works. By striving to exploit the latest state of the art modelling techniques we take steps forward in this goal. Another

aim of state of the art neuroimaging techniques is also to understand pathology of the brain. The NODDI model has been shown to be a sensitive biomarker in certain pathologies [130, 101] as the NODDI model is capable of detecting subtle changes in neurite structure which competing models do not detect. This could potentially have an impact on tractography based on the NODDI model. Tissue changes in certain neurodegenerative diseases such as Alzheimer's or multiple sclerosis may be detected in connectome estimates derived from tractography based on the NODDI model. This could act as an advanced biomarker and help give insights into how tissue changes might affect brain function. This work has concentrated on a small set of healthy subjects. Future work could be extended to cover larger cohorts with both healthy and diseased subjects.

# **Appendices**

# Appendix A

## Publications

The following details all publications associated with this work, which have appeared in peer-reviewed international conferences. Other related publications are also listed.

### A.0.1 Publications associated with this work.

#### Conference proceedings

- **M. Rowe**, H. Zhang, N. Oxtoby and D. C. Alexander. Beyond Crossing Fibers: Tractography Exploiting Sub-voxel Fibre Dispersion and Neighbourhood Structure. In *Proceedings of the 23rd biennial International Conference on Information Processing in Medical Imaging*, California, USA, 2013. (Features a preliminary version of the work covered in Chapter 5). Selected for podium presentation, ~top 10% of submissions.
- **M. Rowe**, H. Zhang, and D. C. Alexander. Utilising measures of fibre dispersion in white matter tractography. In *Proceedings of the MICCAI'12 Workshop on Computational Diffusion MRI*, Nice, France, 2012. (Features a preliminary version of the work covered in Chapter 4). Selected for podium presentation.

## Conference abstracts

- **M. Rowe**, H. Zhang and D. C. Alexander. ND-Track: Tractography Utilising Parametric Models of White Matter Fibre Orientation Dispersion. In *Proceedings of the 21st annual meeting of the International Society for Magnetic Resonance in Medicine (ISMRM)* Utah, USA, 2013. (Features extracts of the work covered in Chapter 4). Selected for podium presentation, ~top 10% of accepted abstracts. Received the ISMRM *magna cum laude* merit award.
- **M. Rowe**, H. Zhang and D. C. Alexander. ND-Track: Tractography Utilising Parametric Models of White Matter Fibre Dispersion. In *Proceedings British Chapter of ISMRM Postgraduate symposium*, held at University College London, London, UK. (Features extracts of the work covered in Chapter 4). Selected for podium presentation.
- **M. Rowe**, H. Zhang and D. C. Alexander. Combining neighbourhood exploration with models of sub-voxel fibre dispersion to improve tractography. In *Proceedings of the ISMRM Workshop on Diffusion as a Probe of Neural Tissue Microstructure*, Podstrana, Croatia, 2013. (Features a preliminary version of the work covered in Chapter 5)

## Papers in preparation

## Journal articles

- **M. Rowe**, H. Zhang, N. Oxtoby, M. Tariq and D. C. Alexander. Exploiting neighbourhood exploration combined with sub-voxel models of fibre dispersion in tractography. *Manuscript in preparation*

## Other publications

### Conference proceedings

- A. J. Sherbondy and **M. Rowe** and D. C. Alexander. MicroTrack: an algorithm for concurrent projectome and microstructure estimation. In *Proc. Medical Image Computing and Computer Assisted Intervention*. 13(Pt 1):183-90. 2010

### Conference abstracts

- A. J. Sherbondy, T. B. Dyrby, **M. Rowe**, M. Ptito, B. A. Wandell, D. C. Alexander. Microstructure Tracking (MicroTrack): An Algorithm for Estimating a Multiscale Hierarchical White Matter Model from Diffusion-Weighted MRI. In *Proc. International Society for Magnetic Resonance in Medicine*. Montreal, Canada, 2011.

# Appendix B

## Sampling from a Bingham distribution

The following is derived from [29].

### B.1 Rejection sampling

To sample from a Bingham distribution, we can make use of the rejection sampling technique, recruiting the simpler Watson distribution, which is simpler to sample from [15, 89], as an *instrumental* distribution. This allows us to draw samples from the instrumental distribution  $g(x)$ , from which we have a known method of drawing samples, and use this to draw samples from an arbitrary distribution  $f(x)$  where  $f(x) < Mg(x)$  and  $M > 1$  gives us an appropriate bound on  $f(x)/g(x)$ .

Samples can be then be drawn from  $f(x)$  via simple algorithm:

- Sample  $x$  from  $g(x)$  and  $u$  from  $U(0, 1)$ .
- Check if  $u < \frac{f(x)}{Mg(x)}$ .
  - If true, accept  $x$  as a realisation of  $f(x)$ .
  - If false, reject  $x$  and repeat.

### B.1.1 Sampling from a Watson distribution

The Watson distribution is given by [78]:

$$f(\mathbf{n}) = W(\mathbf{n}; \mu, \kappa) = F_1\left(\frac{1}{2}, \frac{3}{2}, \kappa\right)^{-1} \exp[\kappa(\boldsymbol{\mu} \cdot \mathbf{n})^2], \quad (\text{B.1})$$

where  $F_1$  is the hypergeometric function (note:  $F_1(1/2, 3/2, \kappa)$  is a number, not a function).  $\mu$  is the mean orientation and  $\kappa$  controls the concentration of the distribution.

If we assume the mean axis to be the Cartesian z-axis, where  $\theta = \phi = 0$ . Then we can generate a sample using the following method (The values  $R_x$  refer to pseudo-random variables from a uniform distribution ( $R \in [0, 1]$ )):

1. Set  $C = \frac{1}{\exp \kappa - 1}$
2.  $U = R_1, V = R_2$
3. Set  $S = \frac{1}{\kappa} \log \frac{U}{C} + 1$
4. If  $V > \exp(\kappa S^2 - \kappa S)$ , go to 2
5. Sample direction is given by  $\theta = \arccos S, \phi = 2\pi R_3$ .

### B.1.2 Sampling from a Bingham distribution using the Watson as the instrumental distribution

As we can sample from a Watson distribution using the method described in section B.1.1, we can now sample from the Bingham distribution using the Watson as the instrumental distribution. We require that the Watson distribution we use wraps the Bingham distribution as closely as possible but must always be greater than or equal to the underlying Bingham. Recalling that the Bingham distribution is given by:

$$f(\mathbf{n}) = F_1\left(\frac{1}{2}, \frac{3}{2}, \kappa_1, \kappa_2\right)^{-1} \exp[\kappa_1(\boldsymbol{\mu}_1 \cdot \mathbf{n})^2 + \kappa_2(\boldsymbol{\mu}_2 \cdot \mathbf{n})^2] \quad (\text{B.2})$$

Therefore:

$$\frac{1}{C_{bw}} \exp[\kappa(\boldsymbol{\mu}_3 \cdot \mathbf{n})^2] \geq \frac{1}{C_B} \exp[\kappa_1(\boldsymbol{\mu}_1 \cdot \mathbf{n})^2 + \kappa_2(\boldsymbol{\mu}_2 \cdot \mathbf{n})^2] \quad (\text{B.3})$$

The normalisation constant  $C_{bw}$  can be found by considering the case where  $n$  is orthogonal to  $\mu_3$ :

$$\frac{1}{C_{bw}} \geq \frac{1}{C_B} \exp[\kappa_1(\boldsymbol{\mu}_1 \cdot \mathbf{n})^2 + \kappa_2(\boldsymbol{\mu}_2 \cdot \mathbf{n})^2] \quad (\text{B.4})$$

As  $\kappa_1 \leq \kappa_2$  the right hand side of equation B.4 is maximal when  $n$  is equal to  $\pm\mu_1$ .

Giving:

$$\frac{1}{C_{bw}} \geq \frac{1}{C_B} \exp \kappa_2 \Rightarrow C_{bw} \leq C_B \exp -\kappa_2 \quad (\text{B.5})$$

Substituting the maximal value of  $C_{bw}$  into equation B.3 and taking the logarithm of both sides gives:

$$\kappa_3(\boldsymbol{\mu}_3 \cdot \mathbf{n})^2 + \kappa_2 \geq \kappa_1(\boldsymbol{\mu}_1 \cdot \mathbf{n})^2 + \kappa_2(\boldsymbol{\mu}_2 \cdot \mathbf{n})^2 \quad (\text{B.6})$$

The right hand side is maximal when  $\mathbf{n} = \mu_3$ , therefore:

$$\kappa_3 \geq -\kappa_2 \quad (\text{B.7})$$

Substituting into equation B.6 gives:

$$\kappa_1(\boldsymbol{\mu}_1 \cdot \mathbf{n})^2 + \kappa_2[(\boldsymbol{\mu}_2 \cdot \mathbf{n})^2 + (\boldsymbol{\mu}_3 \cdot \mathbf{n})^2] - \kappa_2 \leq 0 \quad (\text{B.8})$$

As  $\kappa_1 < \kappa_2$  and  $(\boldsymbol{\mu}_1 \cdot \mathbf{n})^2 + (\boldsymbol{\mu}_2 \cdot \mathbf{n})^2 + (\boldsymbol{\mu}_3 \cdot \mathbf{n})^2 = 1$  for all  $\mathbf{n}$  then equation B.8 is satisfied for all  $\mathbf{n}$ .

## **Appendix C**

### **Second principal networks**

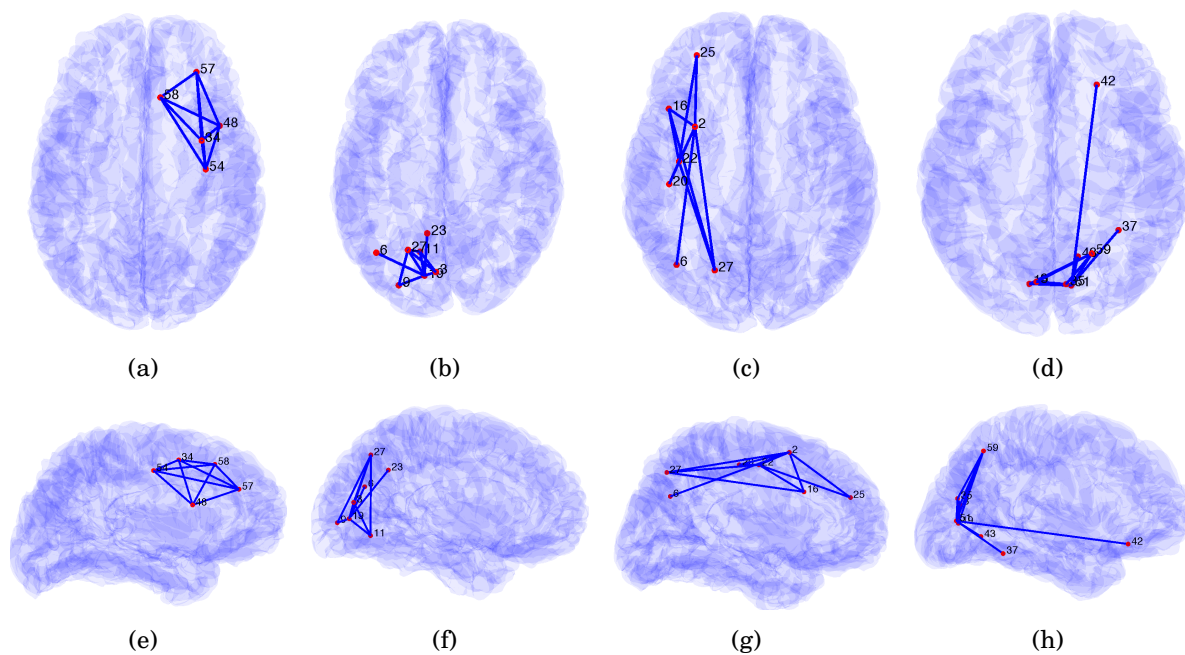


Figure C.1: Second principal networks of 4 subjects derived using NODDI-NIT: axial view (top row: a-d) sagittal view (lower row: e-h). See table 6.1 for cortex regions corresponding to numeric indices.

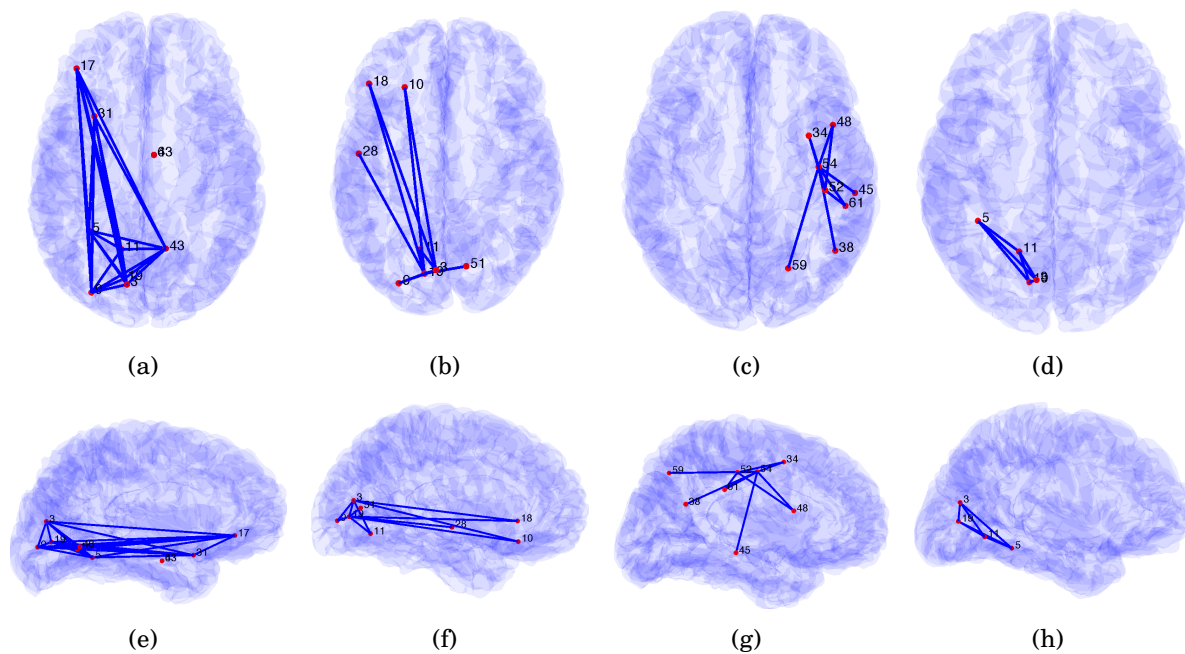


Figure C.2: Second principal networks of 4 subjects derived using DT-PICo: axial view (top row: a-d) sagittal view (lower row: e-h). See table 6.1 for cortex regions corresponding to numeric indices.

# Bibliography

- [1] <http://cmic.cs.ucl.ac.uk/mig/index.php?n=Tutorial.NODDI.matlab>.
- [2] <http://mindboggle.info/data.html>.
- [3] Horn A., Ostwald D., Reisert M., and Blankenburg F. The structural–functional connectome and the default mode network of the human brain . *NeuroImage*, 102, Part 1(0):142 – 151, 2014. Multimodal Data Fusion.
- [4] D. C. Alexander. Maximum Entropy Spherical Deconvolution for Diffusion MRI. In *Proc. Information Processing in Medical Imaging*, pages 76–87, 2005.
- [5] D. C. Alexander. A general framework for experiment design in diffusion mri and its application in measuring direct tissue-microstructure features. *Magnetic Resonance in Medicine*, 60(2):439–448, 2008.
- [6] D. C. Alexander and G. J. Barker. Optimal imaging parameters for fiber-orientation estimation in diffusion MRI. *NeuroImage*, 27(2):357–367, 2005.
- [7] D. C. Alexander, P. I. Hubbard, M. G. Hall, E. A. Moore, M. Ptito, G. J. M. Parker, and T. B. Dyrby. Orientationally invariant indices of axon diameter and density from diffusion MRI. *NeuroImage*, 52(4):1374–1389, 2010.
- [8] A. W. Anderson. Measurement of fiber orientation distributions using high angular resolution diffusion imaging. *Magnetic Resonance in Medicine*, 54(5):1194–1206, 2005.

- [9] P. J. Basser and D. LeBihan. Fiber orientation mapping in anisotropic medium with NMR diffusion spectroscopy. In *Proc. 11th annual meeting of the International Society for Magnetic Resonance in Medicine*, Berlin, Germany, page 1221, 1992.
- [10] P. J. Basser, J. Mattiello, and D. LeBihan. Estimation of the effective self diffusion tensor from the NMR spin echo. *Journal of Magnetic Resonance*, 103:247–254, 1994.
- [11] P. J. Basser, J. Mattiello, and D. LeBihan. MR diffusion tensor spectroscopy and imaging. *Biophys J.*, 66(1):259–267, 1994.
- [12] P. J. Basser, S. Pajevic, C. Pierpaoli, J. Duda, and A. Aldroubi. In vivo fiber tractography using DT-MRI data. *Magnetic Resonance in Medicine*, 44(4):625–632, 2000.
- [13] T. E. J. Behrens, H. Johansen-Berg, S. Jbabdi, M. F. S. Rushworth, and M. W. Woolrich. Probabilistic diffusion tractography with multiple fibre orientations: What can we gain? *NeuroImage*, 34(1):144–155, 2007.
- [14] T. E. J. Behrens, M. W. Woolrich, M. Jenkinson, H. Johansen-Berg, R. G. Nunes, S. Clare, P. M. Matthews, J.M. Brady, and S. M. Smith. Characterization and propagation of uncertainty in diffusion-weighted MR imaging. *Magnetic Resonance in Medicine*, 50(5):1077–1088, 2003.
- [15] D. J. Best and N. I. Fisher. Efficient Simulation of the von Mises Distribution. *Journal of Applied Statistics*, 28(2):152–157, 1979.
- [16] C. Bingham. An antipodally symmetric distribution on the sphere. *The Annals of Statistics*, 2(6):1201–1225, 1974.
- [17] F. Bloch, W. W Hansen, and M. Packard. Nuclear induction. *Physical Review*, 70:460–474, 1946.

- [18] K. Brodmann and L. J. Garey. *Brodmann's: Localisation in the Cerebral Cortex*. Springer, 2006.
- [19] A. Brun, M. Bjornemo, R. Kikinis, and C. F. Westin. White matter tractography using sequential importance sampling. In *Proc. 10th annual meeting of the International Society for Magnetic Resonance in Medicine*, Honolulu, Hawaii, 10, 2002.
- [20] P. T. Callaghan, A. Coy, T. P. J Halpin, D. MacGowan, K. J. Packer, and F. O. Zelaya. Diffusion in porous systems and the influence of pore morphology in pulsed gradient spin-echo nuclear magnetic resonance studies. *The Journal of Chemical Physics*, 97(1):651–662, 1992.
- [21] J. S.W. Campbell, K. Siddiqi, V. V. Rymer, A. F. Sadikot, and G. B. Pike. Flow-based fiber tracking with diffusion tensor and q-ball data: validation and comparison to principal diffusion direction techniques. *NeuroImage*, 27(4):725 – 736, 2005.
- [22] H. Y. Carr and E. M. Purcell. Effects of diffusion on free precession in nuclear magnetic resonance experiments. *Physical review*, 94(3):630, 1954.
- [23] M. Catani, R. J. Howard, S. Pajevic, and D. K. Jones. Virtual in vivo interactive dissection of white matter fasciculi in the human brain. *NeuroImage*, 17(1):77–94, 2002.
- [24] L. C. Chang, D. K. Jones, and C. Pierpaoli. Restore: Robust estimation of tensors by outlier rejection. *Magnetic Resonance in Medicine*, 53(5):1088–1095, 2005.
- [25] C. A. Clark, T. R. Barrick, M. M. Murphy, and B. A. Bell. White matter fiber tracking in patients with space-occupying lesions of the brain: a new technique for neurosurgical planning? *NeuroImage*, 20(3):1601–1608, 2003.
- [26] J. D. Clayden. Imaging connectivity: MRI and the structural networks of the brain. *Funct Neurol*, 28(3):197–203, 2013.

- [27] J. D. Clayden, M. Dayan, and C. A. Clark. Principal networks. *PLoS One*, 8(4), 2013.
- [28] T. E. Conturo, N. F. Lori, T. S. Cull, E. Akbudak, A. Z. Snyder, J. S. Shimony, R. C. McKinstry, H. Burton, and M. E. Raichle. Tracking neuronal fiber pathways in the living human brain. *Proc. Natl. Acad. Sci. U.S.A.*, 96(18):10422–10427, 1999.
- [29] P. A. Cook. Modelling uncertainty in brain fibre orientation from diffusion weighted MRI. *PhD Thesis, University College London*, 2006.
- [30] P. A Cook, D. C Alexander, and G. J M Parker. Modelling noise-induced fibre-orientation error in diffusion tensor MRI. In *Proc. IEEE International Symposium on Biomedical Imaging*, pages 332–336, 2004.
- [31] P. A. Cook, Y. Bai, S. Nedjati-Gilani, K. K. Seunarine, M. G. Hall, G. J. M. Parker, and D. C. Alexander. Camino: Open-Source Diffusion-MRI Reconstruction and Processing. In *Proc. 14th annual meeting of the International Society for Magnetic Resonance in Medicine*, Seattle, Washington., page 2759, 2006.
- [32] F. Dell’Acqua, G. Rizzo, P. Scifo, R. A. Clarke, G. Scotti, and F. Fazio. A model-based deconvolution approach to solve fiber crossing in diffusion-weighted MR imaging. *IEEE Transactions on Medical Imaging*, 54(3):462–472, 2007.
- [33] F. Dell’Acqua, A. Simmons, S. C.R. Williams, and M. Catani. Can spherical deconvolution provide more information than fiber orientations? Hindrance modulated orientational anisotropy, a true-tract specific index to characterize white matter diffusion. *Human Brain Mapping*, 34(10):2464–2483, 2013.
- [34] M. Descoteaux, E. Angelino, S. Fitzgibbons, and R. Deriche. Regularized, fast, and robust analytical Q-ball imaging. *Magnetic Resonance in Medicine*, 58(3):497–510, 2007.

- [35] M. Descoteaux, R. Deriche, T. R. Knösche, and A. Anwander. Deterministic and probabilistic tractography based on complex fibre orientation distributions. *IEEE Transactions on Medical Imaging*, 28(2):269–286, Feb 2009.
- [36] R. S. Desikan, F. Segonne, B. Fischl, B. T. Quinn, B. C. Dickerson, D. Blacker, R. L. Buckner, A. M. Dale, R. P. Maguire, B. T. Hyman, M. S. Albert, and R. J. Killiany. An automated labeling system for subdividing the human cerebral cortex on MRI scans into gyral based regions of interest. *NeuroImage*, 31(3):968–980, 2006.
- [37] T. Dhollander, L. Emsell, W. Van Hecke, F. Maes, S. Sunaert, and P. Suetens. Track Orientation Density Imaging (TODI) and Track Orientation Distribution (TOD) based tractography. *NeuroImage*, 94(0):312 – 336, 2014.
- [38] G. Douaud, T. E. J. Behrens, C. Poupon, Y. Cointepas, S. Jbabdi, V. Gaura, N. Golestani, P. Krystkowiak, C. Verny, P. Damier, A-C Bachoud-L  vi, P. Hantraye, and P. Remy. In vivo evidence for the selective subcortical degeneration in Huntington’s disease. *NeuroImage*, 46(4):958 – 966, 2009.
- [39] A. Doucet, S. Godsill, and C. Andrieu. On sequential Monte Carlo sampling methods for Bayesian filtering. *Stat. and Comput.*, 10:197–208, 2000.
- [40] B. Draganski, F. Kherif, S. Kl  ppel, P. A. Cook, D. C. Alexander, G. J. M. Parker, R. Deichmann, J. Ashburner, and R. S. J. Frackowiak. Evidence for segregated and integrative connectivity patterns in the human basal ganglia. *The Journal of Neuroscience*, 28(28):7143–7152, 2008.
- [41] A. Einstein. Uber die von der molekularkinetischen Theorie der warme gefordete Bewegung von in ruhenden Flussigkeiten suspendierten Teilchen. *Ann. Phys*, 4:549–560, 1905.
- [42] A. Fick. Concerns diffusion and concentration gradient. *Ann. Phys Lpz*, 59:170, 1855.

- [43] P. Fillard, C. Poupon, and J. F. Mangin. A Novel Global Tractography Algorithm Based on an Adaptive Spin Glass Model. In *Proc. international conference on Medical Image Computing and Computer Assisted Intervention.*, pages 927–934, 2009.
- [44] Freesurfer. <http://surfer.nmr.mgh.harvard.edu/>.
- [45] O. Friman, G. Farneback, and C. F. Westin. A Bayesian Approach for Stochastic White Matter Tractography. *Transactions on Medical Imaging*, 25(8):965–978, 2006.
- [46] O. Friman, G. Farneback, and C. F. Westin. A Bayesian Approach for Stochastic White Matter Tractography. *IEEE Transactions on Medical Imaging*, 25(8):965–978, 2006.
- [47] H Gray. *Grays anatomy of the Human Body*. Lea and Febiger, 1918.
- [48] P. Hagmann, L. Cammoun, X. Gigandet, S. Gerhard, P. E. Grant, V. Wedeen, Reto Meuli, Jean-Philippe Thiran, Christopher J. Honey, and Olaf Sporns. MR connectomics: Principles and challenges. *Journal of Neuroscience Methods*, 194(1):34–45, 2010.
- [49] P. Hagmann, L. Cammoun, X. Gigandet, R. Meuli, C. J. Honey, and V. J. Wedeen. Mapping the structural core of human cerebral cortex. *PLoS Biol*, pages 154–161, 2008.
- [50] P. Hagmann, M. Kuran, X. Gigandet, P. Thiran, V. J. Wedeen, R. Meuli, and J. P. Thiran. Mapping human whole-brain structural networks with diffusion MRI. *PLoS ONE*, pages 154–161, 2008.
- [51] P. Hagmann, J. P. Thiran, L. Jonasson, P. Vandergheynst, S. Clarke, P. Maeder, and R. Meuli. DTI mapping of human brain connectivity: statistical fibre tracking and virtual dissection. *NeuroImage*, 19:545–554, 2003.

- [52] A. Hammers, R. Allom, M. J. Koepp, S. L. Free, R. Myers, L. Lemieux, D. J. Brooks, and J. S. Brooks. Three-dimensional maximum probability atlas of the human brain, with particular reference to the temporal lobe. *Human Brain Mapping*, 19(4):224–247, 2003.
- [53] C. P. Hess, P. Mukherjee, E. T. Han, D. Xu, and D. B. Vigneron. Q-ball reconstruction of multimodal fiber orientations using the spherical harmonic basis. *Magnetic Resonance in Medicine*, 56(1):104–117, 2006.
- [54] T. Hosey, G. Williams, and R. Ansorge. Inference of multiple fiber orientations in high angular resolution diffusion imaging. *Magnetic Resonance in Medicine*, 54(6):1480–1489, 2005.
- [55] Y. Iturria-Medina, R. C. Sotero, E. J. Canales-Rodríguez, Y. Alemán-Gómez, and L. Melie-García. Studying the human brain anatomical network via diffusion-weighted MRI and Graph Theory. *NeuroImage*, 40(3):1064 – 1076, 2008.
- [56] title = Direct estimation of the fiber orientation density function from diffusion-weighted MRI data using spherical deconvolution. J. D. Tournier and F. Calamante and D. G. Gadian and A. Connelly. *NeuroImage*, 23:1176–1185, 2004.
- [57] K. M. Jansons and D. C. Alexander. Persistent angular structure: new insights from diffusion MRI data. *Inverse Problems*, 19(5):1031–1046, 2003.
- [58] S. Jbabdi and H. Johansen-Berg. Tractography: Where Do We Go From Here? *Brain Connectivity*, 1(3):169–183, 2011.
- [59] S. Jbabdi, M. W. Woolrich, J. L. R. Andersson, and T. E. J. Behrens. A bayesian framework for global tractography. *NeuroImage*, 37(1):116 – 129, 2007.
- [60] M. Jenkinson, P. R. Bannister, J. M. Brady, and S. M. Smith. Improved optimisation for the robust and accurate linear registration and motion correction of brain images. *NeuroImage*, 17(2):825–841, 2002.

- [61] M. Jenkinson and S. M. Smith. A global optimisation method for robust affine registration of brain images. *Medical Image Analysis*, 5(2):143–156, 2001.
- [62] B. Jeurissen, A. Leemans, J. D. Tournier, and J. Sijbers. Estimation of uncertainty in constrained spherical deconvolution fiber orientations. In *Proc. IEEE International Symposium on Biomedical Imaging: Macro to Nano*, pages 907–910, 2008.
- [63] D. K. Jones. Tractography gone wild: Probabilistic tracking using the wild bootstrap. In *In Proc. 14th annual of the International Society for Magnetic Resonance in Medicine* Seattle, Washington, USA, page 435, 2006.
- [64] D. K. Jones and C. Pierpaoli. Confidence mapping in diffusion tensor magnetic resonance imaging tractography using a bootstrap approach. *Magnetic Resonance in Medicine*, 53(5):1143–1149, 2005.
- [65] E. Kaden, T. R. Knösche, and A. Anwander. Parametric spherical deconvolution: Inferring anatomical connectivity using diffusion MR imaging. *NeuroImage*, 37(2):474–488, 2007.
- [66] E. Kaden, T. R. Knösche, and A. Anwander. Variational inference of the fiber orientation density using diffusion MR imaging. *NeuroImage*, 42(4):1366–80, 2008.
- [67] J. Karger and W. Heink. The propagator representation of molecular transport in microporous crystallites. *Journal of Magnetic Resonance*, 51(1):1–7, 1983.
- [68] J. C. Klein, M. F.S. Rushworth, T. E.J. Behrens, C. E. Mackay, A. J. de Crespigny, H. D’Arceuil, and H. Johansen-Berg. Topography of connections between human prefrontal cortex and mediodorsal thalamus studied with diffusion tractography. *NeuroImage*, 51(2):555 – 564, 2010.
- [69] T. Klingberg, M. Hedehus, E. Temple, T. Salz, D. E. Gabriele, M. E. Moseley, and R. A. Poldrack. Microstructure of temporo-parietal white matter as a basis for reading ability. *Neuron*, 25(2):493–500, 2000.

- [70] B. W. Kreher, I. Mader, and V. G. Kiselev. Gibbs Tracking: A Novel Approach for the Reconstruction of Neuronal Pathways. *Magnetic Resonance in Medicine*, 60(4):953–963, 2008.
- [71] M. Lazar and A. L. Alexander. White matter tractography using random vector (RAVE) perturbation. In *Proc. 10th annual meeting of the International Society for Magnetic Resonance in Medicine*, Hawaii, USA, 10:0523, 2002.
- [72] M. Lazar, P. J. Thottakara, A. S. Field, B. Laundre, B. Badie, B. Jellison, and A. L. Alexander. A white matter tractography study of white matter reorganization after surgical resection of brain neoplasms. In *Proc. 12th annual meeting of the International Society for Magnetic Resonance in Medicine*, Kyoto, Japan., page 1259, 2004.
- [73] M. Lazar, D. M. Weinstein, J. S. Tsurada, K. M. Hasan, K. Arfanakis, M. E. Meyerand, B. Badie, H. A. Rowley, V. Haughton, A. Field, and A. L. Alexander. White Matter Tractography Using Diffusion Tensor Deflection. *Human Brain Mapping*, 18(4):306–321, 2003.
- [74] D. LeBihan, E. Breton, D. Lallemand, P. Grenier, E. Cabanis, and M. Laval-Jeantet. MR imaging of intravoxel incoherent motions: application to diffusion and perfusion in neurologic disorders. *Radiology*, 161(2):401–407, 1986.
- [75] I. B. Levitan and L. K. Kaczmarek. *The neuron: cell and molecular biology*. Oxford University Press, 3rd edition, 2002.
- [76] L. Li, J. K. Rilling, T. M. Preuss, M. F. Glasser, F. W. Damen, and X. Hu. Quantitative assessment of a framework for creating anatomical brain networks via global tractography. *NeuroImage*, 61(4):1017–1030, 2012.
- [77] Catani M., Dell’Acqua F., Vergani F., Malik F., Hodge H. and Roy P., Valabregue R., and Thiebaut de Schotten M. Short frontal lobe connections of the human brain. *Cortex*, 48(2):271–261, 2012.

- [78] K. V. Mardia and P. E. Jupp. *Directional Statistics*. Wiley, 2000.
- [79] S. Mori, B. J. Crain, V. P. Chacko, and P. C. M. van Zijl. Three dimensional tracking of axonal projections in the brain by magnetic resonance imaging. *Ann Neurol*, 45(2):265–269, 1999.
- [80] S. Mori, W. E. Kaufmann, C. Davatzikos, B. Stieltjes, L. Amodei, K. Fredericksen, G. D. Pearlson, E. R. Melhem, M. Solaiyappan, G. V. Raymond, H. W. Moser, and P. C. M. van Zijl. Imaging cortical association tracts in the human brain using diffusion-tensor-based axonal tracking. *Magnetic Resonance in Medicine*, 47(2):215–223, 2002.
- [81] J. Nolte. *The human brain: An introduction to its functional anatomy*. Mosby Elsevier, 2008.
- [82] E. Panagiotaki, T. Schneider, B. Siow, M. G. Hall, M. F. Lythgoe, and D. C. Alexander. Compartment models of the diffusion mr signal in brain white matter: A taxonomy and comparison. *NeuroImage*, 59(3):2241–54, 2012.
- [83] G. D. Parker, D. Marshall, P. L. Rosin, N. Drage, S. Richmond, and D.K. Jones. A pitfall in the reconstruction of fibre ODFs using spherical deconvolution of diffusion MRI data. *NeuroImage*, 65(0):433 – 448, 2013.
- [84] G. J. Parker and D. C. Alexander. Probabilistic Monte Carlo based mapping of cerebral connections utilising whole-brain crossing fibre information. *Lecture Notes in Computer Science*, 2732:684–695, 2003.
- [85] G. J. Parker and D. C. Alexander. Probabilistic anatomical connectivity derived from the microscopic persistent angular structure of cerebral tissue. *Philosophical Transactions of the Royal Society B: Biological Sciences*, 360(1457):893–902, 2005.
- [86] G. J. M. Parker, H. A. Haroon, and C. A. M. Wheeler-Kingshott. A Framework for a Streamline-Based Probabilistic Index of Connectivity (PICO) Using a Structural

- Interpretation of MRI Diffusion Measurements. *Journal of Magnetic Resonance Imaging*, 18(2):242–254, 2003.
- [87] M. Perrin, C. Poupon, Y. Cointepas, B. Rieul, N. Golestani, C. Pallier, D. Riviere, A. Constantinesco, D. LeBihan, and J. F Mangin. Fiber tracking in q-ball fields using regularized particle trajectories. In *Proc. Information Processing in Medical Imaging*, 19:52–63, 2005.
- [88] J. Pontabry and F. Rousseau. Probabilistic tractography using Q-ball modeling and particle filtering. In *Proc. Medical Image Computing and Computer-Assisted Intervention*, 14:209–16, 2011.
- [89] W. H. Press, S. A. Teukolsky, W. T. Vetterling, and B. P. Flannery. *Numerical Recipes in C (2nd Ed.): The Art of Scientific Computing*. Cambridge University Press, New York, NY, USA, 1992.
- [90] Binder J. R., Frost J. A., Hammeke T. A., Cox R. W., Rao S. M., and Prieto T. Human Brain Language Areas Identified by Functional Magnetic Resonance Imaging. *Journal of Neuroscience*, 17(1):353–362, 1997.
- [91] M. Reisert, I. Mader, C. Anastasopoulos, M. Weigel, S. Schnell, and V. Kiselev. Global fiber reconstruction becomes practical. *NeuroImage*, 54(2):955 – 962, 2011.
- [92] T. W. Riffert, J. Schreiber, A. Anwander, and T. R. Knäusche. Beyond fractional anisotropy: Extraction of bundle-specific structural metrics from crossing fiber models. *NeuroImage*, 100(0):176 – 191, 2014.
- [93] E. C. Robinson, M. Valstar, A. Hammers, A. Ericsson, A. D. Edwards, and D. Rueckert. Multivariate statistical analysis of whole brain structural networks obtained using probabilistic tractography. In *Proc. Medical Image Computing and Computer-Assisted Intervention*, 11(Pt 1):486–93, 2008.

- [94] M. Rowe, H. Zhang, and D. C Alexander. Utilising measures of fiber dispersion in white matter tractography. In *Proc. CD-MRI, MICCAI*, 2012.
- [95] M. Rowe, H. Zhang, N. Oxtoby, and D. C. Alexander. Beyond crossing fibers: Tractography exploiting sub-voxel fibre dispersion and neighbourhood structure. In JamesC. Gee, Sarang Joshi, KilianM. Pohl, WilliamM. Wells, and Lilla ZÁülle, editors, *Information Processing in Medical Imaging*, volume 7917 of *Lecture Notes in Computer Science*, pages 402–413. Springer Berlin Heidelberg, 2013.
- [96] K. E. Sakaie and M. J. Lowe. An objective method for regularization of fiber orientation distributions derived from diffusion-weighted MRI. *NeuroImage*, 34(1):169–176, 2007.
- [97] P. Savadjiev, J. S. W. Campbell, M. Descoteaux, R. Deriche, G. B. Pike, and K. Siddiqi. Labeling of ambiguous subvoxel fibre bundle configurations in high angular resolution diffusion MRI. *NeuroImage*, 41(1):58–68, 2008.
- [98] P. Savadjiev, G. L. Kindlmann, S. Bouix, M. E. Shenton, and C. F. Westin. Local white matter geometry from diffusion tensor gradients. *NeuroImage*, 49(4):3175–3186, 2010.
- [99] P. Savadjiev, Y. Rathi, J. G. Malcolm, M. E. Shenton, and C. F. Westin. A geometry-based particle filtering approach to white matter tractography. volume 13, page 233–240, 2010.
- [100] B. Scherrer, M. Taquet, and S. K. Warfield. Reliable selection of the number of fascicles in diffusion images by estimation of the generalization error. *Proceedings of the 23rd international conference on Information Processing in Medical Imaging*, 7917:742–753, 2013.
- [101] T. Schneider, W. Brownlee, H. Zhang, O. Ciccarelli, D. H. Miller, and C. Wheeler-Kingshott. Application of multi-shell NODDI in Multiple Sclerosis. In *Proc. 22nd*

*annual meeting of the International Society for Magnetic Resonance in Medicine*, Milan, Italy,, 22:0019, 2014.

- [102] K. K. Seunarine and D. C. Alexander. Linear persistent angular structure MRI and non-linear spherical deconvolution for diffusion MRI. In *Proc. 14th annual meeting of the International Society for Magnetic Resonance in Medicine*, Seattle, Washington., page 2726, 2006.
- [103] K. K. Seunarine and D. C. Alexander. *Multiple fibres: beyond the diffusion tensor. In Johansen-Berg H., Behrens T. E. J. (Eds.), Diffusion MRI: From Quantitative Measurement to In Vivo Neuroanatomy. Chapter 4.* Elsevier, 2009.
- [104] K. K. Seunarine, P. A. Cook, M. G. Hall, K. V. Embleton, G. J. M. Parker, and D. C. Alexander. Exploiting peak anisotropy for tracking through complex structures. *Proc. IEEE International Conference on Computer Vision Workshop on MMBIA*, 2007.
- [105] A. J. Sherbondy, R. F. Dougherty, R. Ananthanarayanan, D. S. Modha, and B. A. Wandell. Think Global, Act Local; Projectome Estimation with Bluematter. pages 861–868. Springer-Verlag Berlin Heidelberg, 2009.
- [106] A. J. Sherbondy, M. Rowe, and D. C. Alexander. MicroTrack: an algorithm for concurrent projectome and microstructure estimation. In *Proc. Medical Image Computing and Computer-Assisted Intervention*, 13:183–90, 2010.
- [107] S. M. Smith. Fast robust automated brain extraction. *Human Brain Mapping*, 17(3):143–155, 2002.
- [108] S. N. Sotiropoulos, T. E. J. Behrens, and S. Jbabdi. Ball and rackets: Inferring fiber fanning from diffusion-weighted MRI. *NeuroImage*, 60(2):1412–1425, 2012.
- [109] S. N Sotiropoulos, C Chen, K Dikranian, S. Jbabdi, T. E J Behrens, D. C VanEssen, and M. F Glasser. Comparison of Diffusion MRI Predictions and Histology in the

- Macaque Brain. In *In Proc. 21st annual of the International Society for Magnetic Resonance in Medicine*, page 0835, 2013.
- [110] S. N. Sotiropoulos, S. Jbabdi, J. Xi, J. L. Andersson, S. Moeller, D. J. Auerbach, M. F. Glasser, M. Hernandez, G. Sapiro, M. Jenkinson, D. A. Feinberg, E. Yacoub, C. Lenglet, D. C. VanEssen, K. Ugurbil, and T. E. J. Behrens. Advances in diffusion MRI acquisition and processing in the Human Connectome Project. *NeuroImage*, 80:125–143, 2013.
  - [111] A. Stamm, O. Commowick, C. Barillot, and P. Perez. Adaptive Multi-modal Particle Filtering for Probabilistic White Matter Tractography. *Proceedings of the 23rd international conference on Information Processing in Medical Imaging*, 7917:594–606, 2013.
  - [112] G. J. Stanisz, A. Szafer, G. A. Wright, and M. Henkelman. An analytical model of restricted diffusion in bovine optic nerve. *Magnetic Resonance in Medicine*, 37(1):103–111, 1997.
  - [113] E. O Stejskal and J. E Tanner. Spin diffusion measurements: spin echoes in the presence of a time-dependent field gradient. *Journal of Chemical Physics*, 42:288–292, 1965.
  - [114] A. Szafer, J. H. Zhong, and J. C. Gore. Theoretical model for water diffusion in tissues. *Magnetic Resonance in Medicine*, 33(5):697–712, 1995.
  - [115] M. Tariq, T. Schneider, D. C. Alexander, C. A. M Wheeler-Kingshott, and H. Zhang. In vivo estimation of dispersion anisotropy of neurites using diffusion MRI. In *Proc. Medical Image Computing and Computer-Assisted Intervention*, 8675:241–248, 2014.
  - [116] M. Tariq, T. Schneider, D. C. Alexander, C. A. M. Wheeler-Kingshott, and H. Zhang. NODDI with dispersion anisotropy. In *Proc. 22nd annual meeting of the International Society for Magnetic Resonance in Medicine*, Milan, Italy,, 22:0104, 2014.

- [117] J. D. Tournier, F. Calamante, and A. Connelly. Robust determination of the fibre orientation distribution in diffusion MRI: non-negativity constrained super-resolved spherical deconvolution. *NeuroImage*, 35(4):1459–1472, 2007.
- [118] J. D. Tournier, F. Calamante, and A. Connelly. Mrtrix: Diffusion tractography in crossing fiber regions. *International Journal of Imaging Systems and Technology*, 22(1):53–66, 2012.
- [119] J. D. Tournier, F. Calamante, D. G. Gadian, and A. Connelly. Probabilistic fibre tracking through regions containing crossing fibres. In *Proc. 13th annual meeting of the International Society for Magnetic Resonance in Medicine*, Miami, Florida, USA, page 1343, 2005.
- [120] D. S. Tuch. Q-ball imaging. *Magnetic Resonance in Medicine*, 52(6):1358–1372, 2004.
- [121] D. S. Tuch, T. G. Reese, M. R. Wiegell, N. Makris, J. W. Belliveau, and V. J. Wedeen. High Angular Resolution Diffusion Imaging Reveals Intravoxel White Matter Fiber Heterogeneity. *Magnetic Resonance in Medicine*, 48(4):577–582, 2002.
- [122] D. S. Tuch, T. G. Reese, M. R. Wiegell, and V. J. Wedeen. Diffusion MRI of complex neural architecture. *Neuron*, 40(5):885–895, 2003.
- [123] S. G. Waxman-editor. *Gray’s anatomy of the Human Body*. Oxford university press, 1918.
- [124] V. J. Wedeen, P. Hagmann, W. Tseng, T. G. Reese, and R. M. Weiskoff. Mapping complex tissue architecture with diffusion spectrum magnetic resonance imaging. *Magnetic Resonance in Medicine*, 54(6):1377–1386, 2005.
- [125] V. J. Wedeen, T. G. Reese, D. S. Tuch, J. G. Dou, R. M. Weiskoff, and D. Chessler. Mapping fiber orientation spectra in cerebral white matter with fourier-transform

- diffusion mri. In *Proc. 7th annual meeting of the International Society for Magnetic Resonance in Medicine*, Philadelphia, Pennsylvania, USA.
- [126] D. Weinstein, G. Kindlmann, and E. Lundberg. Tensorlines: advection-diffusion based propagation through diffusion tensor fields. In *Proc. Conference on Visualization*, 3:249–530, 1999.
- [127] C. F. Westin, S. E. Maler, H. Mamata, A. Nabavi, F. A. Jolesz, and R. Kikinis. Processing and visualization for diffusion tensor mri. *Medical Image Analysis*, 6(2):93–108, 2002.
- [128] B. Whitcher, D. S. Tuch, and L. Wang. The wild bootstrap to quantify variability in Diffusion Tensor MRI. In *Proc. 13th annual meeting of the International Society for Magnetic Resonance in Medicine*, Miami, Florida, USA.
- [129] T. H. Williams, N Gluhbegovic, and J. Y. Jew. *Virtual Hospital: The Human Brain: Dissections of the Real Brain (1997)* .
- [130] G. P. Winston, M. R. Symms, D. C. Alexander, J. S. Duncan, and H. Zhang. Clinical Utility of NODDI in Assessing Patients with Epilepsy Due to Focal Cortical Dysplasia. In *Proc. 21st annual meeting of the International Society for Magnetic Resonance in Medicine*, Salt Lake City, Utah, USA, 21:0784, 2013.
- [131] G. P. Winston, M. Yogarajah, M. R. Symms, A. W. McEvoy, C. Micallef, and J. S. Duncan. Diffusion tensor imaging tractography to visualize the relationship of the optic radiation to epileptogenic lesions prior to neurosurgery. *Epilepsia*, 52(8):1430–1438, 2011.
- [132] X. Wu, Q. Xu, L. Xu, J. Zhou, A. W. Anderson, and Z. Ding. Genetic white matter fiber tractography with global optimization. *Journal of Neuroscience Methods*, 184(2):375 – 379, 2009.

- [133] F. Zhang, E. R. Hancock, C. Goodlett, and G. Gerig. Probabilistic white matter fiber tracking using particle filtering and von Mises-Fisher sampling. *Medical Image Analysis*, 13(1):5–18, 2009.
- [134] H. Zhang, P. L. Hubbard, G. J. M. Parker, and D. C. Alexander. Axon diameter mapping in the presence of orientation dispersion with diffusion MRI. *NeuroImage*, 56:1301–1315, 2011.
- [135] H. Zhang, T. Schneider, C. A. M. Wheeler-Kingshott, and D. C. Alexander. NODDI: Practical in vivo neurite orientation dispersion and density imaging of the human brain. *NeuroImage*, 61(4):1000–1016, 2012.